Introduction

Infrasonic waves may be thought of as the equivalent of seismic compressional waves that propagate in the atmosphere. Because volcanic explosion earthquakes occur at or near the free surface, some eruptions radiate more elastic energy into the atmosphere than into the ground. Neglecting the information contained in radiated infrasonic pressure traces can lead to the misinterpretation of the associated seismic signals and source mechanisms for volcanic degassing.

This dissertation provides numerous examples of the benefits of recording the infrasound generated by volcanic degassing. The first chapter is an introduction to volcanic infrasound, providing an overview of the simplicity of atmospheric propagation filters. Raw infrasonic waveforms are thus much more representative of the gas flux history from a volcanic vent than the corresponding seismic waveforms. The second chapter focuses on infrasonic and seismic signals produced at two volcanoes (Erebus and Karymsky) that demonstrate relatively simple Strombolian-type behavior. At these two volcanoes, arrays of microphones and seismometers recorded the elastic energy from hundreds of explosive events, allowing a critical analysis of the relative energy partitioning into the ground and atmosphere. Synchronous video footage and COSPEC gas flux data at Karymsky provide additional constraints for the analysis of the degassing mechanisms. Finally, the third chapter introduces and analyzes seismo-acoustic waveforms generated at a series of different volcanoes, with activities ranging from Strombolian to Vulcanian to phreato-magmatic. Comparisons are made between the infrasound produced at the various volcanic centers by taking into account magma chemistry and firsthand observations of eruptive behavior.

Chapter 1 - Generation and Propagation of Infrasonic Airwaves from Volcanic Explosions

1.1 Chapter Overview

In recent years, co-installation of low-frequency acoustic pressure sensors at seismic stations has furthered the understanding of volcanic explosion dynamics. Infrasonic acoustic airwaves produced during volcanic degassing offer a relatively unfiltered version of source motions at the vent because shear waves do not exist in the atmosphere and velocity gradients in the atmosphere tend to be slight compared to infrasonic wavelengths. Small scale gradients that cause reflections or scattering of infrasonic energy are not significant. Volcanoes generate substantial energy in the infrasonic bandwidth (below 20 Hz), a portion of the acoustic spectrum that suffers very little attenuation due to transmission losses and receiver site response. Unfortunately propagation of infrasound in the atmosphere can be significantly affected by variable atmospheric conditions which can cause acoustic rays to refract and focus or defocus. To accurately recover explosion source overpressures at the vent, care must be taken to understand the propagation effects caused by time-varying atmospheric winds and temperatures. Excess pressure time histories at the vent are proportional to the time derivative of the mass flux. For many explosions, infrasound strength is a good measure of the impulsivity of degassing source. For larger explosions, the acoustic approximation may not be an appropriate assumption because excess pressures may be large enough that an explosion begins as or becomes a shockwave. In these instances, pressure waves propagate supersonically and non-linearly.

1.2 Introduction

Even when an active volcano is obscured by clouds, detonations, booming, cracking, and whooshing noises can indicate the eruption of gas and solid material from the vent. Richards (1963) recorded audible acoustic noises from a suite of volcanoes with activities

ranging from Hawaiian and Strombolian to Vulcanian and acknowledged that volcanic sources generate substantial low-frequency acoustic energy. More recently, other investigators have deployed low-frequency sensitive microphones in the vicinity of actively degassing volcanoes including: Tolbachik and Klyuchevskoi [Firstov & Kravchenko, 1996], Stromboli [Vergniolle et al., 1996], Unzen [Yamasato, 1998, Sakurajima [Garces et al., 1999], Arenal [Hagerty et al., 2000], Erebus [Rowe et al., 2000], Karymsky and Sangay [Johnson & Lees, 2000]. Infrasonic pressure traces recorded from these volcanoes (see figure 1.1) reveal varied degassing behaviors. In many instances (most notably at Tolbachik, Klyuchevskoi, Stromboli, Erebus, and in certain explosions from Arenal and Karymsky - figure 1.1a,b,c,d,g,i,j), infrasonic signals consist primarily of a single compression followed by a more gradual rarefaction. In other cases, pressure traces have a complex coda lasting several minutes indicative of continued degassing (see figure 1.1f,h,k,l). However, many of the extended degassing events (with the exception of Tolbachik - figure 1.1e) begin with the same characteristic impulsive compressional onset. The examples in figure 1.1 are shown to provide an overview of degassing signals from different volcanoes and may not be representative of typical degassing behavior at each of the volcanoes (refer to chapter 3 for a more detailed comparison of infrasonic signals).

Infrasonic pressure traces are time histories of atmospheric pressure pertubations relative to a fixed atmospheric pressure. The excess pressure is usually very small compared to ambient atmospheric pressure ($\sim 10^5$ Pa). At distances of several kilometers from the vent, many of the infrasonic traces from figure 1 show peak excess pressures greater than 10 Pascals. A 10 Pascal excess pressure corresponds to 115 dB sound pressure level (SPL) relative to a fixed excess pressure amplitude of 2 x 10^{-5} Pa:

$$SPL \; = \; 20\log\left(\frac{excess\ pressure}{2 \times 10^{-5}}\right) \qquad\qquad (1.1)$$

An SPL of 115 dB in the audible bandwidth corresponds to the noise produced by a pneumatic riveter [Truax, 1978].
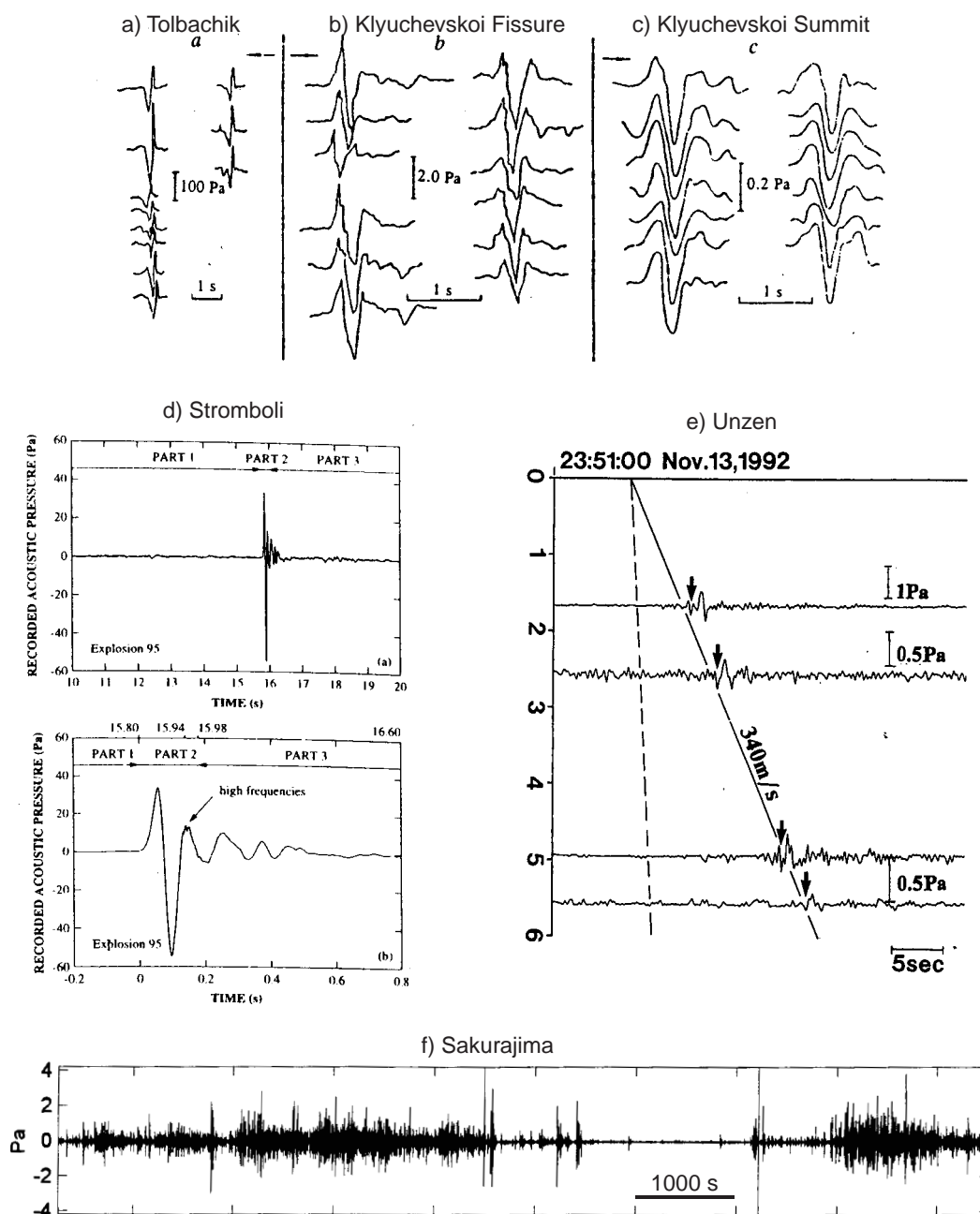
Figure 1.1 Infrasound Signals - Low-frequency acoustic waveforms recorded in the vicinity of degassing volcanoes with VEI I or VEI II activity. Examples are from a) Tolbachik (note that the time axis is reversed) and b-c) Klyuchevskoi [Firstov & Kravchenko, 1996], d) Stromboli [Vergniolle et al., 1996], e) Unzen [Yamasato, 1998], and f) Sakurajima [Garces et al., 1999].

g,h) Arenal

i) Erebus
Jan 10, 1998 05:36 UTC

Acoustic

± 50 Pa

E1LI

TIME (SECONDS)

j,k) Karymsky

Karymsky Simple Impulse Event (1997:234:07:01)

Karymsky Chugging Event (1997:233:15:23)

l) Sangay
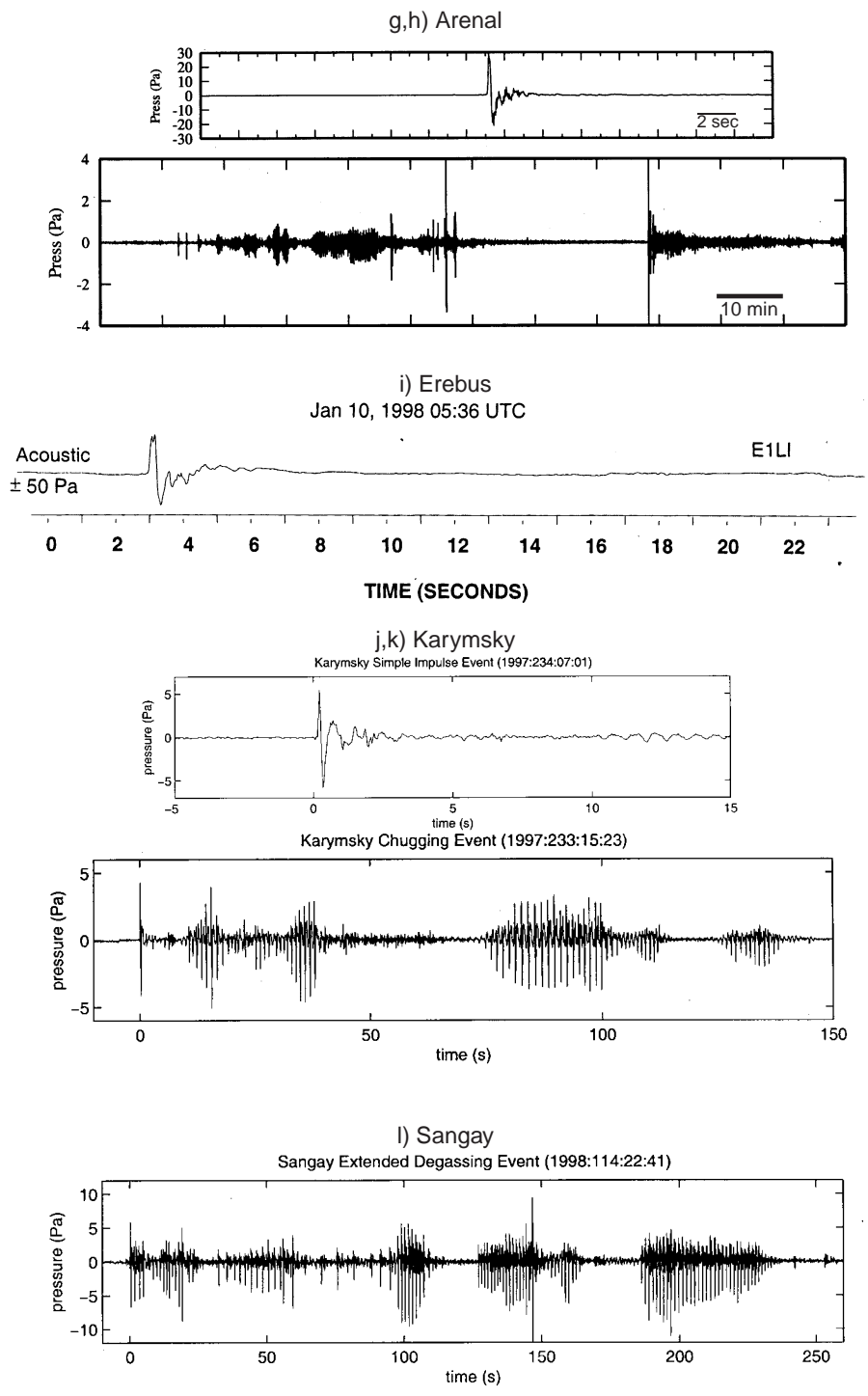
Sangay Extended Degassing Event (1998:114:22:41)

Figure 1.1 (continued) Infrasound Signals - Infrasonic pressure traces from: g-h) Arenal [Hagerty et al., 2000], i) Erebus [Rowe et al., 2000], j-k) Karymsky [Johnson & Lees, 2000], and l) Sangay [Johnson & Lees, 2000]. Example waveforms may not be representative of the typical degassing activity at the above volcanoes.

At Karymsky and Sangay, audible sounds from the volcanic explosions rarely exceed volumes comparable to street traffic (80 dB [Truax, 1978]) at distances of several kilometers from the vent [author's observation]. Vergniolle et al. (1996) also estimate that explosions at Stromboli are about 30 dB 'softer' in the audible band than in the infrasonic band. Because acoustic energy scales with the square of acoustic pressure [Truax, 1978], the 30 dB difference in SPL indicates about a factor ~1000 difference in acoustic energy. In general, volcanic sounds should be recorded in the infrasonic bandwidth because acoustic intensity is greatest.

For a source which radiates acoustic waves radially, the total acoustic energy is proportional to the time-integrated squared pressure trace. For hemispherically radiating infrasound (see appendix A):

$$E_{acoustic} = \frac{2\pi r^2}{\rho_a c} \int \Delta P^2 dt \qquad (1.2)$$

r = distance between source and receiver (m)

ρ_a = air density (1.189 kg/m^3 at standard temperature and pressure)

c = sound speed (343 m/s at standard tememperature and pressure)

ΔP = excess pressure (Pa)

Table 1 shows approximate acoustic energies for the waveforms displayed in figure 1.1 according to equation 1.2. Because these energy values are estimations made directly from paper records of infrasonic pressure traces, they should only be considered accurate to within an order-of-magnitude. Sound pressure levels for these infrasonic records are calculated at 100 meters using the maximum excess pressure and assuming an inverse relationship between pressure amplitude and distance [Truax, 1978]. Event durations are also approximate values which correspond to the time interval when infrasonic pressure traces are above background noise levels (noise levels in these records have variable amplitude). Finally, the equivalent magma volume release is calculated assuming 100% transferal of compressed gas expansion energy (refer to figure 1.2) to acoustic energy.

Table 1 Infrasonic Signal Summary - Volcano name and information (from references), distance between microphone and explosion source, peak excess pressure at recording site, sound pressure level at 100 meters assuming inverse pressure amplitude decay with distance, explosion duration determined from coda lengths, estimated acoustic energy at standard temperature and pressure according to equation 1.2, and equivalent volume of degassed magma (from figure 1.2).

volcano name, magma chemistry, and type of explosion	distance of microphone from source	peak excess pressure	SPL at 100 meters	estimated explosion duration	acoustic energy estimated from trace data	equivalent volume of degassed magma
a) Tolbachik, basalt, single pulses	1.9-2.6	100 Pa	160 dB	2 s	1×10^8 J	10 m^3
b) Klyuchevskoi fissure, basalt, single pulses	12.2 km	2 Pa	142 dB	3 s	2×10^6 J	0.2 m^3
c) Klyuchevskoi summit, basalt, single pulses	14.6 km	0.2 Pa	123 dB	3 s	2×10^4 J	0.002 m^3
d) Stromboli, basalt, single pulse	0.3 km	50 Pa	136 dB	0.5 s	1×10^5 J	0.01 m^3
e) Unzen, dacitic dome, emergent, low amplitude	1.7 km	1 Pa	119 dB	~5 s	1×10^4 J	0.0001 m^3
f) Sakurajima, andesite, extended degassing	~3.0 km	4 Pa	136 dB	~10^4 s	4×10^8 J	4 m^3
g) Arenal1, andesite, single pulse	~2 km	30 Pa	150 dB	3 s	1×10^7	0.1 m^3
h) Arenal2, andesite, extended duration explosion	~2 km	4 Pa	132 dB	~10^3 s	3×10^7	0.3 m^3
i) Erebus, phonolite, single pulse	0.7 km	50 Pa	145 dB	4 s	4×10^6	0.4 m^3
j) Karymsky1, andesite, single pulse	1.6 km	5 Pa	132 dB	4 s	2×10^5	0.002 m^3
k) Karymsky2, andesite, series of pulses	1.6 km	5 Pa	132 dB	~10^2 s	3×10^6	0.03 m^3
l) Sangay, basaltic andesite, series of pulses	2.2 km	10 Pa	141 dB	~10^2 s	2×10^7	0.2 m^3

It is important to record acoustic airwaves with low-frequency pressure sensors because volcanic sources generate exceedingly 'loud' signals at frequencies between 2 s and 10 Hz that remain above background noise levels even at great distances from the source. A further advantage to infrasound recording is that acquisition sample rates are compatible with typical seismic data acquisition sample rates. Co-located acoustic and seismic sensors may conveniently share a single datalogger or telemetry site.

1.3 Explosion Source and Acoustic Energy

During eruptions, gas flux (mass per unit time) can range from ~10 kg/s for Strombolian 'pops' to ~10^8 kg/s for Plinian columns [Newhall & Self, 1982]. However, there is a much

greater wealth of quality infrasonic data recorded at VEI I and VEI II volcanoes because these sites offer frequent, repetitive explosions and relatively safe access. Also, infrasound generation at the Strombolian end of the degassing spectrum is relatively easy to model for the following reasons: (1) a point source approximation is appropriate, (2) infrasound sources are generated at the ground/atmosphere interface and not within a convecting column, (3) the bulk of the elastic wave energy is generated prior to the mixing of magmatic and atmospheric gases, (4) ejection velocities are subsonic. In contrast, a point source is not appropriate for larger eruption plumes, where infrasound can be generated from a diffuse volume with a dimension greater than the infrasonic wavelengths.

The current consensus among most researchers at VEI I and VEI II volcanoes is that the fundamental source of infrasonic signals is the rapid release of pressurized gas from a vent. Yamasato (1997) calculated radiated acoustic pressures for two types of sources at Unzen Volcano (ground dislocations and volumetric gas expansions) and concluded that ground dislocations were not large enough to produce the observed infrasonic signals. Other investigators [Firstov & Kravchenko, 1996; Vergniolle et al., 1996; Rowe et al., 2000; Johnson & Lees, 2000] use visual observations to substantiate that the primary infrasonic pulse is coincident with rapid gas expansion from the vent.

Ideal gases under adiabatic conditions (no heat exchange to surroundings) and isentropic conditions (reversible process), release significant energy during explosive gas expansion [Kinney & Graham, 1985]:

$$E_e \ = \ \frac{(M/m)RT_i}{\gamma - 1}\left[1 - \left(\frac{P_o}{P_i}\right)^{\frac{\gamma - 1}{\gamma}}\right] \qquad (1.3)$$

$E_e \ = \ $ potential energy of explosion (in Joules)

$M \ = \ $ mass of gas (kg)

$m \ = \ $ molecular weight of gas (0.018 kg/mole for water vapor)

R = gas constant (8.314 N·m/mol·kelvin)

T_i = initial temperature (1000 to 1500 K for magmatic gases)

P_o = atmospheric pressure (~10^5 Pa)

P_i = initial gas pressure

γ = heat capacity ratio (1.1 for hot gases [Garces et al., 1998a])

If the initial pressure of magmatic volatiles is taken to be the overburden pressure at depth (before decompression), gas expansion energies can be estimated for several different types of eruptions (see figure 1.2) using equation 1.3 and typical properties of magmatic eruptions (fragmentation depths and weight percent of volatiles [Sparks, 1997]). Gas expansion energies from figure 1.2 are extremely large (~1-10 MJ/kg^3 for basaltic magma, ~100 MJ/kg^3 for andesite, and ~250 MJ/kg^3 for rhyolite) compared to the radiated acoustic energy values listed in table 1 (0.01 MJ to 100 MJ). The equivalent volume of degassed magma (last column of table 1) is vastly underestimated because only a fraction of the energy released during volatile expansion is converted to infrasonic energy (refer to chapter 2 for more on the efficiency of elastic energy radiation).

Several different dissipation phenomena can explain the discrepancy between the potential energy released during volcanic eruptions and the total acoustic energy recovered from infrasonic pressure traces. Work done by expanding volcanic gases may be absorbed by a host of energy transport mechanisms including: seismic waves, permanent ground deformation, kinetic energy tied to ballistic and ash emissions, frictional heat losses in the conduit, and non-adiabatic, and non-isentropic processes. McGetchin & Chouet (1979) have dealt with some of these energy transport modes while studying the energy budget for Stromboli Volcano. They concluded that during the frequent explosions, heat carried by ejected gas and particles was most dominant energy mode (97%), followed by seismic energy radiation (1 to 3%), kinetic energy of ejected gas and ballistics (0.07%), and finally acoustic power (0.01%). Though McGetchin &
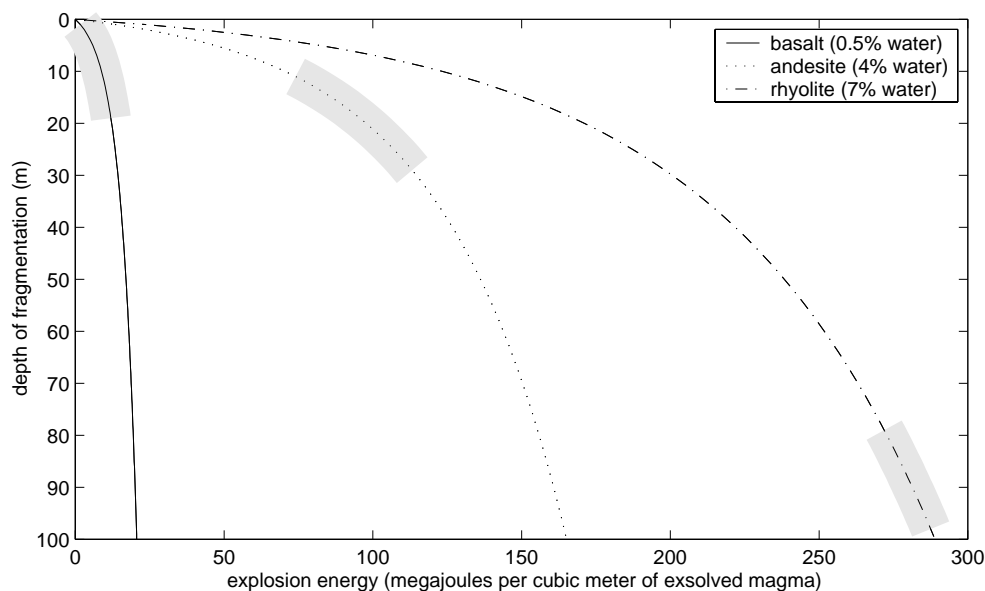
Figure 1.2 Potential Gas Expansion Energy - Potential energy released due to the expansion of compressed volatiles. Energies are calculated for bubbles filled with water vapor suspended hydostatically in a magma with density 2700 kg/m^3. Possible fragmentation depths for the different magma types are indicated by shading. Volatile weight percent is from Sparks (1997).

Chouet (1979) calculated acoustic power based on analysis of audible sound waves (infrasonic energy is two to three orders of magnitude higher), the total acoustic power radiated from Stromboli is still only a small fraction of the total energy release. Roughly acoustic power is the same order-of-magnitude as the radiated seismic energy (1 to 3%).

Aside from the aforementioned energy transport sinks, some volcanic explosions also generate acoustic gravity waves, which are atmospheric pressure pertubations with periods longer than 270 seconds that are propagated by buoyancy forces [Beer, 1974]. Acoustic gravity waves are observed in the far-field in association with extremely large movements of air parcels such as the 1980 Mount St. Helens eruption [Mikumo & Bolt, 1985] or the 1992 Pinatubo eruption [Tahira et al., 1996], but are not observed in association with small explosions. For VEI I and II eruptions, plume heights and gravity waves are much smaller because the heat injected into the atmosphere is comparatively small [Wilson et al., 1978].

The heat energy transported by erupted material is the largest portion of the energy budget released during volcanic eruptions. The heat capacity of water vapor is about 1860 Joules/kg/Kelvin [Sparks, 1997] so for the three types of magma displayed in figure 1.2, cooling energies for the volatile phase ranges from 10^1 to 10^2 MJ per cubic meter of degassed magma. Cooling energy for ejected solid phase (heat capacity of 1100 Joules/ kg/Kelvin [Sparks, 1997]) is about 10^3 MJ per cubic meter of degassed magma. Though this energy value exceeds the energy released through gas expansion, heat transport is not likely to be a source of infrasound unless thermal shocking of the atmosphere is invoked as a source mechanism (such as the thunder generated during rapid atmospheric heating caused by lightning).

1.4 Infrasonic Waveforms

Expansion of gas at the vent is the most likely source of infrasound because the atmosphere is significantly perturbed by a rapid gas volume outflux. If frictional heat generation caused by air resistance is neglected, momentum and energy flux from the vent should be conserved. Firstov & Kravchenko (1996) employ these arguments to approximate gas release volumes at Klyuchevskoi and Tolbachik Volcanoes using low-frequency microphones deployed tens of kilometers from the vent.

Recorded acoustic pressure traces are a convolution of a source pressure time series, propagation filters, and instrument responses. Source pressure time series are valued because they offer information about the physical motions at the vent. Fortunately, atmospheric propagation does not filter acoustic waveforms significantly because the atmosphere does not support shear waves and it is largely devoid of structures which scatter and reflect acoustic waves. Atmospheric structure can affect acoustic arrival times and signal strength (see acoustic propagation filters section), but compared with seismic propagation filters, atmospheric propagation effects are minimal. Deconvolution of the instrument response from acoustic waveforms is not complicated as many modern

pressure transducers and electret condenser microphones have nearly flat responses in the frequencies of interest (see appendix B).

The acoustic approximation is suitable for infrasonic pressure pertubations which are infinitessimal with respect to the ambient atmospheric pressure. Assuming a homogeneous medium and point source, the restoring force in the atmosphere is proportional to particle displacement. Acoustic compressional waves propagate elastically according to the wave equation for spherical waves [Jensen et al., 1994]:

$$\nabla^2(\Delta P) - \frac{1}{c^2}\frac{\partial^2}{\partial t^2}(\Delta P) = -F(t)\delta(r) \tag{1.4}$$

$$c = \text{sound speed}$$

$$F(t) = \text{effective force function}$$

The solution to the inhomogeneous wave equation can be written in the form [Lay & Wallace, 1995]:

$$4\pi r \Delta P = -F\left(t - \frac{r}{c}\right) \tag{1.5}$$

Where the sound speed is [Ford, 1970]:

$$c = \sqrt{\frac{E}{\rho_a}} = \sqrt{\gamma R T} \approx \sqrt{402.8T} \tag{1.6}$$

$$E = \text{bulk modulus (1.4 x 10^5 Pa)}$$

$$\rho_a = \text{air density (1.189 kg/m^3 at standard temperature and pressu)}$$

$$\gamma = \text{heat capacity ratio (1.4)}$$

$$R = \text{gas constant (287 Joules/kg/Kelvin)}$$

$$T = \text{temperature (degrees K)}$$

Compressional waves propagate at a velocity equal to the square root of the bulk modulus divided by the density. For the atmosphere, sound speed is proportional to the square root of temperature [Ford, 1970]. In the lower atmosphere (troposphere), acoustic waves

may propagate as slowly as 306 m/s (at -40 degrees C) and as fast as 355 m/s (at +40 degrees C).

For a simple acoustic source, the effective force function ($F(t)$) is equal to the rate of change of mass outflow from the source [Lighthill, 1978]. Therefore the excess pressure according to the linear theory of sound is [Lighthill, 1978]:

$$\Delta P = \left(\frac{1}{4\pi r} \right) \left[\frac{dq(t - r/c)}{dt} \right] \tag{1.7}$$

$$q(t) = \text{mass flux from a point source}$$

For hemispherically radiating acoustic waves, the excess pressure is proportional to $1/(2\pi r)$. Figure 1.3 shows the acoustic pressure trace generated from a simple acoustic source radiating into a half space. The asymmetric mass flux function is described by $10000/(t^2 + 0.01)$ for $t < 0$ and $10000/(t^2 + 0.1)$ for $t > 0$, where t is time in seconds.
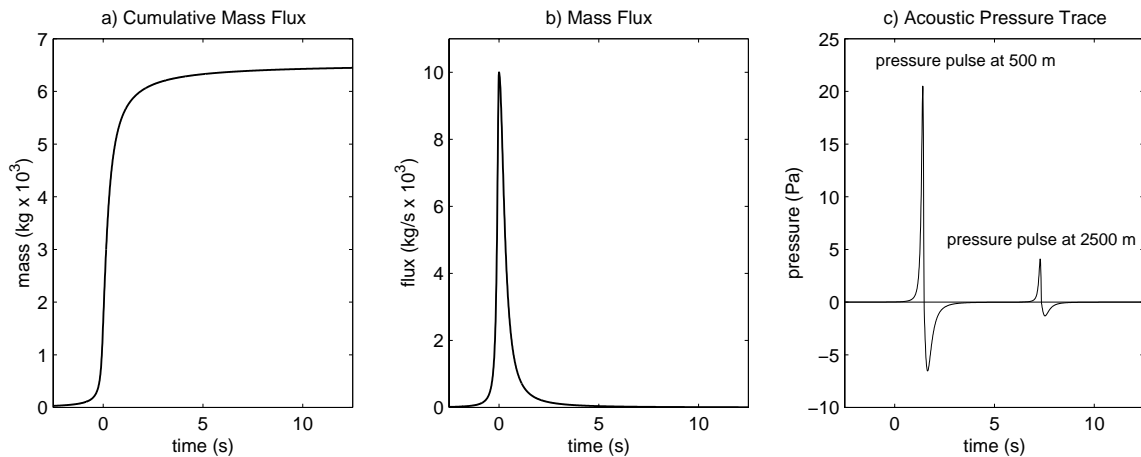
Figure 1.3 Arbitrary Mass Flux and Synthetic Infrasonic Pulse - The generation of a transient acoustic pressure pulse from a point source gas release at a volcanic vent. a) Potential cumulative gas flux history for an impulsive explosion. b) Time history of the mass flux representing a rapid degassing onset followed by more gradual tapering. c) Pressure pulses calculated at 500 meters and 2500 meters from the vent assuming standard atmospheric temperature and pressure.

The associated source mass flux derived from an acoustic pressure trace is one of the most important parameter that can be recovered from infrasonic data because it is closely

related to the gas emission rate from the vent. To determine an accurate mass flux, several assumptions must be made including: (1) instrument response and propagation effects are removed, (2) wind noise and barometric changes are negligible, (3) source is a point fixed at the vent, (4) pressure pertubations are small enough that a linear relationship exists between excess pressure, particle velocity, and particle displacement. For pressure traces recorded in the far field from a source at the edge of a halfspace:

$$q(\tau) = 2\pi r \int_0^\tau \Delta P\left(t + \frac{r}{c}\right) dt \tag{1.8}$$

$$\tau = \text{source duration}$$

The cumulative gas outflux is the time integral of the mass flux rate:

$$M(t) = \int_0^\tau 2\pi r \left[\int_0^\tau \Delta P\left(t + \frac{r}{c}\right) dt \right] d\tau \tag{1.9}$$

$$M(t) = \text{cumulative mass flux from source}$$

Equation 1.8 reveals that low-frequency mass flux signals are not featured prominently in the acoustic pressure traces because excess pressure is the time derivative of mass flux. Infrasonic microphones should theoretically not even be able to record steady-state laminar gas flow. Therefore cumulative gas flux values recovered from infrasonic pressure traces should be considered a lower limit. Fortunately, the onset of most Strombolian explosions are impulsive by nature. Because the rate of degassing accelerates dramatically at the onset of an explosion, high-amplitude infrasound signals are recorded and may be used to recover cumulative mass outflux for the onset of an explosion.

For larger and more explosive sources with rapid ejection velocities, a point source mass flux is too simplistic because the atmospheric pertubation front is translated away from the vent as material is ejected into the atmosphere. For mass ejection velocities approaching the speed of sound, Doppler shifts should be incorporated to account for frequency variations in the recorded pressure traces.
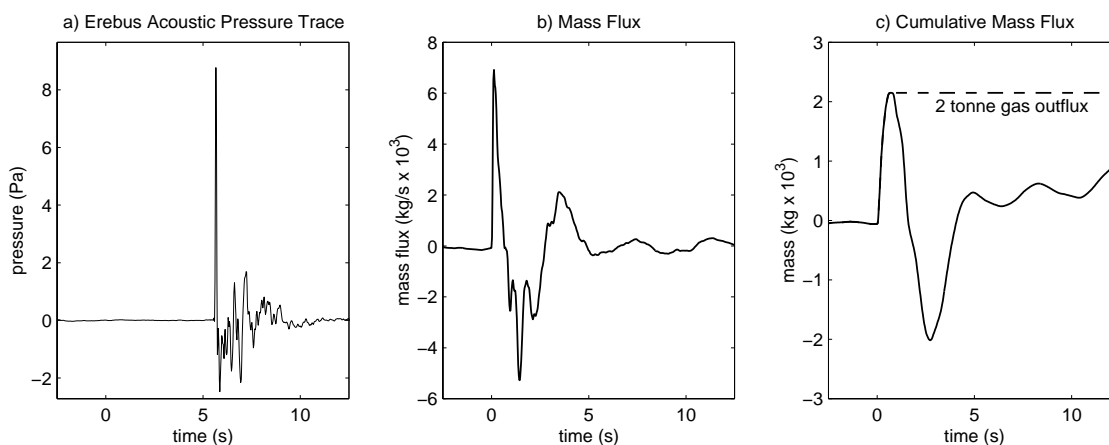
Figure 1.4 Infrasonic Pulse and Associated Mass Flux - a) Recorded acoustic pressure trace associated with an explosion at Erebus (1999:359:06:52), recorded 660 meters from the vent at station EHUT. The example is selected because it is a low-noise, simple explosion. b) Corresponding mass flux time history according to 1.8 and c) cumulative gas flux according to equation 1.9. Dashed line represents maximum mass outflux. Negative mass fluxes are artificial, low-frequency artifacts, or alternatively, inertial effects [Kinney & Graham, 1985].

1.5 Acoustic Propagation Filters

Though the structure of the atmosphere is much less complicated than the structure of the earth, acoustic energy is bent and refracted by velocity and wind gradients causing possible shadow zones at distances greater than a few kilometers. However, when conditions are agreeable, acoustic signals from large eruptions such as Krakatoa in 1883 may be ducted in low-velocity channels and remain audible at distances of many thousands of kilometers [Bedard & Georges, 2000]. Eyewitness reports of sounds heard from large eruptions can be mapped regionally [Fairfield, 1980; Power, 1993] to reveal zones of inaudibility (often close to the volcano or upwind of the volcano) and zones of high sound intensity (sometimes several hundred kilometers from the vent). Johnson & Malone (1997) explained the audibility patterns from the 1980 Mount St. Helens airblast by tracing acoustic rays in a U.S. standard atmosphere (see figure 1.5). They utilized Garces et al. (1998b) formulation for computing traveltimes of infrasonic waves propagating in a stratified atmosphere where the ray parameter is conserved.

$$p = \frac{\sin(i_o)}{c(z)}\left(1 + \frac{u(z)\sin(i_o)}{c(z)}\right)^{-1} \qquad (1.10)$$

p = ray parameter (horizontal slowness)

i_o = angle of incidence (from vertical)

$c(z)$ = intrinsic sound speed (function of height)

$u(z))$ = horizontal wind speed (parallel to propagation direction)

Even at the intermediate distances of 100 meters to 5 km commonly used during the deployment of microphones at Strombolian-type volcanoes, atmospheric structure can significantly impact the amplitude of a recorded pressure trace. Figure 1.6 presents several potential weather scenarios, corresponding acoustic raypaths for those weather conditions, and the effective atmospheric pressure magnification factors (MF). The magnification factor is calculated from traveltime curves and is defined here as the ratio of the recorded pressure amplitude to the expected pressure amplitude for an isotropic source in a homogenous atmosphere:

$$MF(X) = \sqrt{\frac{Ed_s}{Ed_h}} \qquad (1.11)$$

Where the energy density is determined by [Lay & Wallace, 1995]:

$$Ed = \frac{\tan(i_o)}{X\cos(i_1)}\frac{dp}{dX} \qquad (1.12)$$

Ed = relative energy density (for structured (s) and homogeneous (h) atmospheres)

i_1 = incidence raypath angle (from vertical)

X = horizontal distance from source

Under still wind conditions with typical temperature gradients, magnification factors less than a factor of 2 can be expected out to distances of about 5 km. Beyond this distance, however, magnification factors often change dramatically and upward refraction can create silent zones relatively close to the source (see figures 1.6c,d). In general, wind has a more substantial influence on magnification factors than temperature gradients. Under
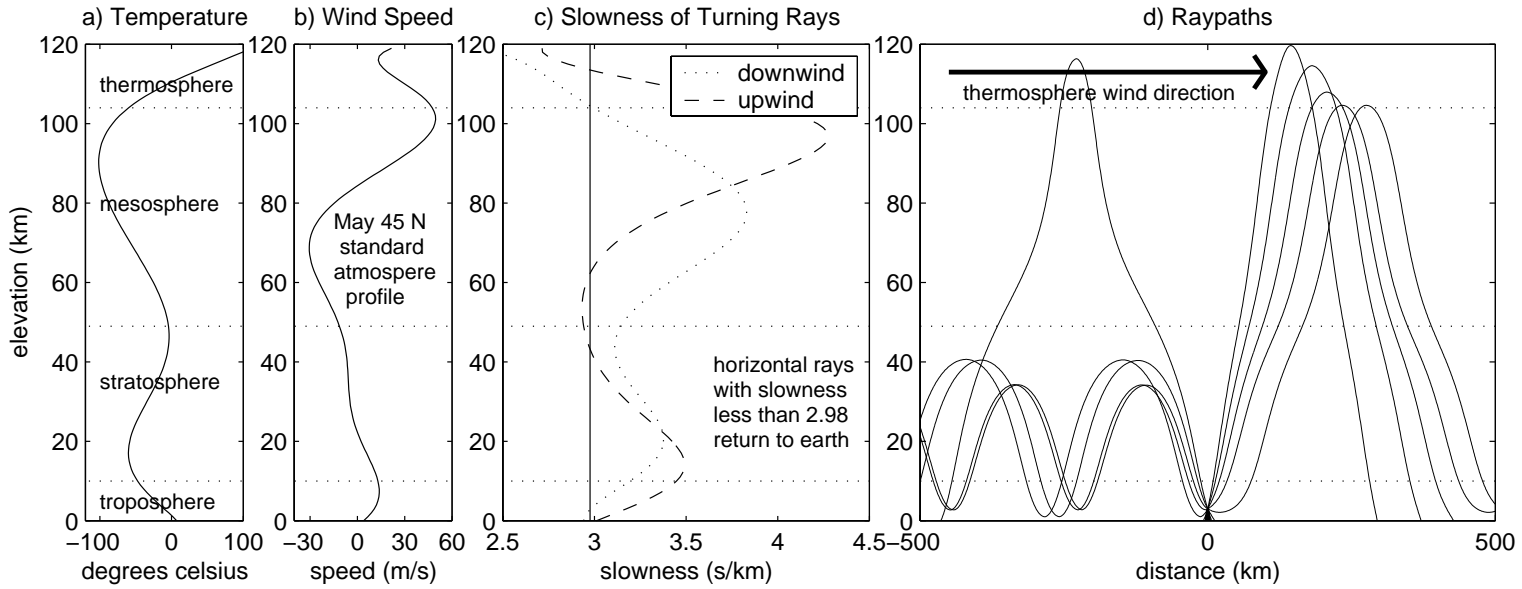
a) Temperature

b) Wind Speed

c) Slowness of Turning Rays

d) Raypaths

thermosphere

mesosphere

stratosphere

troposphere

elevation (km)

degrees celsius

May 45 N standard atmospere profile

speed (m/s)

downwind

upwind

horizontal rays with slowness less than 2.98 return to earth

slowness (s/km)

thermosphere wind direction

distance (km)

Figure 1.5 Regional Infrasound Propagation - a) Temperature profile, b) zonal wind profile, and c) horizontal ray parameter profile for the month of May at 45 degrees north. d) Acoustic raypaths from an explosion source such as the one generated by Mount St. Helens are refracted in the stratosphere and thermosphere [from Johnson & Malone, 1997]. Rays are displayed at 10 degree increments.

windy conditions, or under drastic temperature gradients, shadow zones may be found as close as 2 km from the source.

Apart from geometric spreading, acoustic attenuation can result from propagation inefficiencies through the atmosphere due to molecular absorption and viscous friction losses as well as scattering, reflection, and absorption effects at boundaries. In classical acoustic attenuation, amplitude decay due to transmission losses through the atmosphere depends exponentially upon the square of the frequency [Reed, 1972].

$$\Delta P = \Delta P_i e^{-(\alpha f^2 / \rho_a) r} \tag{1.13}$$

ΔP_i = initial overpressure

α = attenuation constant

f = frequency (Hz)

According to Reed (1972), empirical values for α / ρ_a range from 1.3×10^{-11} s^2/m to 3.0×10^{-11} s^2/m, corresponding to about 2×10^{-5} dB/km for 10 Hz infrasound. These small values indicate that attenuation of infrasound is extremely small for acoustic propagation in the lower atmosphere even at global distances. However, molecular absorption is moisture and frequency dependent and other researchers have shown that absorption coefficients may be considerably higher. Bass & Bauer (1972) list absorption coefficients for 10 Hz infrasound as high 0.2 dB/km for sound in dry air and 0.002 dB/km for air with 100 percent humidity.

Scattering or reflections caused by wind turbulence or localized density contrasts (such as an ash cloud) is another mechanism that may be responsible for acoustic dissipation and should receive more attention. Such atmospheric heterogeneities can have pronounced effects upon higher frequency acoustic waves, but may not affect infrasonic energy with quarter wavelengths ranging from 4 meters at 20 Hz to 85 meters at 1 Hz. The same principle applies to small barriers or topography in the vicinity of infrasonic receivers. Low-frequency microphones may be deployed in depressions or behind small barriers
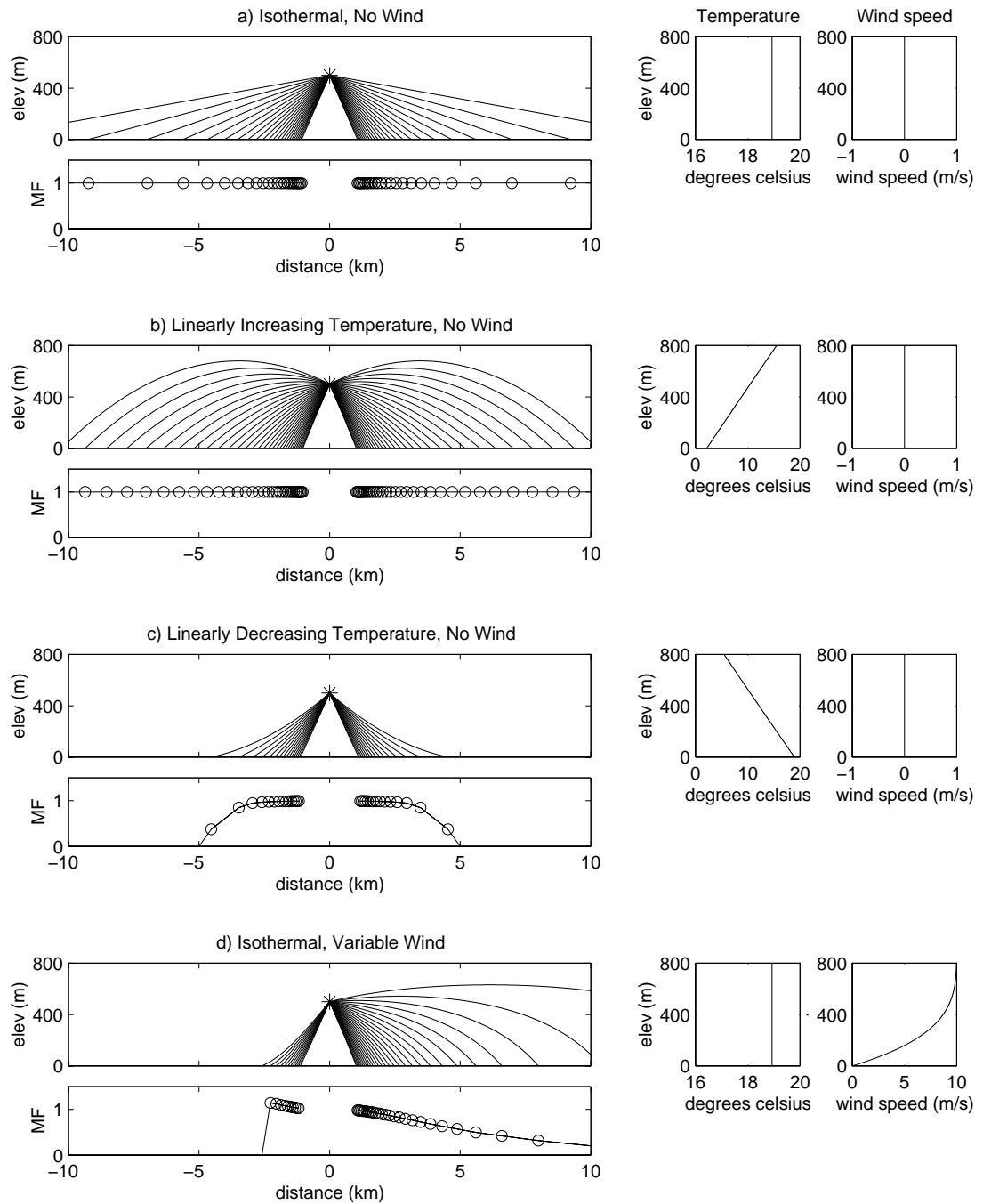
Figure 1.6 Infrasonic Focusing at Close Offsets - Dependence of raypaths on variable atmospheric conditions: a) homogeneous atmosphere, b) temperature inversion with no wind, c) normal temperature gradient with no wind, and d) isothermal atmosphere and wind increasing with altitude. Acoustic rays are radiated at 1 degree increments. Magnification factors (MF) for each raypath are shown for the three scenarios. An absence of raypaths impacting the ground indicates shadow zones.

without inducing significant site responses. Amplitude loss is roughly proportional to the ratio of barrier height over acoustic wavelength [Maekawa, 1968].

Ground absorption is yet another dissipative mechanism for sound waves. Hard surfaces induce little attenuation, but surfaces covered with vegetation can attenuate 125 Hz sound by as much as 6 dB per kilometer [Maekawa, 1968]. Infrasound attenuation due to ground absorption will be less severe but not insignificant. Destructive interference from sound waves reflecting at shallow angles tends to plague high acoustic frequencies, but is not a major concern for infrasound [Truax, 1978].

1.6 Non-linear Propagation and Explosive Shocks

For larger volcanic explosion sources and/or in the near-field, acoustic airwave propagation may be non-linear because initial mass flux is either supersonic or pressure transients are high enough that the acoustic approximation is invalid. Chemical explosions generate non-linear shock waves (discontinuous pressure traces) by expanding at supersonic velocities. Although Strombolian ejection velocities range up to only a few hundred meters per second [Sparks, 1997], there is evidence for Plinian eruptions with emissions exceeding 500 m/s [Wilson, 1980]. Shock wave velocities exceed sound speed and are a function of the shock excess pressure [Kinney & Graham, 1985]:

$$\overline{M} = \sqrt{1 + \left(\frac{\gamma + 1}{2\gamma}\right)\left(\frac{\Delta P}{P_o}\right)} \tag{1.14}$$

$\overline{M}$ = Mach number = (shock speed)/(sound speed)

As a shockwave expands radially, excess pressure drops and Mach number decreases until shock waves deteriorate into acoustic waves that travel at ambient sound speed. Arrival times for shock waves propagating to far offsets can be predicted by integrating along slowness/distance curves. A spherical shock with 0.01 bars excess pressure at 1 km will precede a low amplitude acoustic wave by approximately 0.13 seconds at far offsets. And a shockwave with 0.1 bars excess pressure at 1 km will arrive 1.3 seconds

faster than a low amplitude acoustic wave. Though excess pressure from large eruptions may exceed ~10^3 Pa at distances of 1 km [Reed, 1987], upper bounds for excess pressures from Strombolian explosions are approximately 100 Pa at 1 km. Acoustic radiation from Strombolian explosions thus propagates at the speed of sound.

Even when explosion expansion velocities are initially subsonic, pressure pertubations may be large enough that acoustic signals steepen or 'shock up' with time [Kinney & Graham, 1985]. As acoustic pressure pertubations propagate, the atmosphere heats or cools adiabatically according to the ideal gas law. Because sound speed increases with the square root of temperature, trailing portions of an acoustic pressure wave with large excess pressures can catch up toward the front of the wave. This mechanism is used by Reed (1987) to explain how low-frequency air waves that were inaudible within 50 km of the Mount St. Helens eruption acquired higher frequencies and were audible at farther offsets.

As a first order approximation for ideal gases under adiabatic conditions, sound speed can be related to excess pressure by (see appendix A):

$$\Delta c = c \left[\left(\frac{P_o + \Delta P}{P_o} \right)^{\frac{\gamma - 1}{2\gamma}} - 1 \right] \qquad (1.15)$$

Δc = change in sound speed

Figure 1.7 shows the potential transformation of pressure waves with different amplitudes according to equation 1.15. Although the waveform modeling is simplistic, it gives an indication of excess pressure amplitudes where non-linear effects may become important and pressure waves can steepen. Strombolian airwaves will not 'shock up' because excess pressures are too low. However, larger eruptions are certainly capable of generating pressure-time traces which evolve as they propagate away from the source.
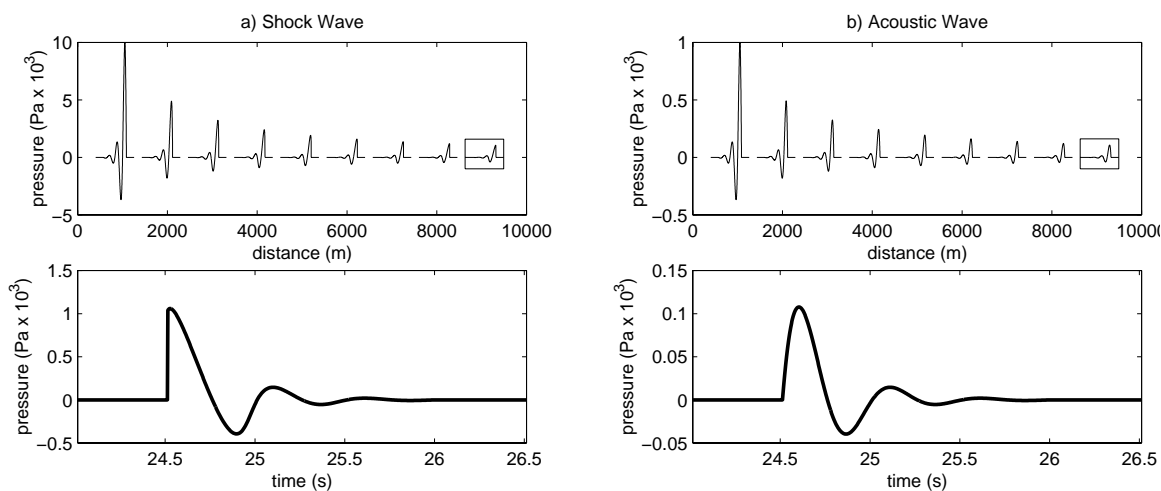
Figure 1.7 Non-linear Infrasound Propagation - a) Pressure-distance waveform evolution for a 2 Hz damped sinusoid with 0.1 bar maximum excess pressure at 1000 m (Plinian explosion). b) Pressure-distance waveform evolution for a 2 Hz damped sinusoid with 0.01 bar maximum excess pressure at 1000 m (large Strombolian explosion). Waveforms are modeled according to equation 1.14 at STP for spherical spreading with no attenuation. Lower panels shows pressure-time waveforms at ~9 km. Non-linear 'shocking-up' is evident only in the larger explosion.

1.7 Summary

Infrasonic signals provide an extremely useful tool for the study of actively degassing volcanoes. Not only do erupting volcanoes generate the majority of their acoustic energy in the infrasonic bandwidth, but infrasonic energy is little affected by propagation filters, transmission losses, dispersion, or site responses. Though changing atmospheric properties can influence infrasonic amplitudes and arrival times, they do not significantly distort the original waveform. Non-linear propagation effects are only important for very large eruptions (excess pressures greater than $\sim 10^3$ Pa at 1 km). These excess pressures are not likely exceeded during Strombolian eruptions.

Chapter 2 - Variable Source Energy Partitioning for Strombolian Explosions

2.1 Chapter Overview

Once instrument responses and weather-dependent propagation influences have been deconvolved from recorded infrasonic waves, source overpressures may be recovered and compared to radiated seismic energy. Together, infrasonic and seismic signals can help quantify the energy that is released by a volcanic explosion and constrain the elastic energy partitioning into the atmosphere and ground. This chapter focuses on the seismo-acoustic energy partitioning for discrete Strombolian-type explosions at Erebus and Karymsky volcanoes. Though the Strombolian-type explosions at Erebus consistently radiate proportional amounts of energy into the acoustic and seismic wavefields, the explosions at Karymsky demonstrate widely variable partitioning of energy into the ground and into the atmosphere, indicating that either acoustic or seismic energy by itself is a poor indicator of relative explosion size. To understand how degassing signals relate to the size of an explosion, comparisons are made between inferred vent overpressures, reduced seismic displacements, video records of the explosions, and gas flux measurements. The total energy budget for small Strombolian-type explosions is discussed in terms of potential energy of pressurized volatiles and dissipation due to radiated elastic and kinetic energies, and viscous losses. This chapter shows that although elastic energy is only a small component of the total energy budget, it is an appropriate diagnostic of conditions at the vent. High acoustic radiation efficiency (relative to seismic) at Erebus is attributed to explosion sources occurring at the very surface of a lava lake. Generally lower acoustic efficiencies at Karymsky are attributed to sources that may occur at slight depth within the conduit. Variable source-energy partitioning, which is apparent at Karymsky but not Erebus, is dependent upon changing conduit geometries and fragmentation depths.

2.2 Introduction

Remotely assessing explosion strength is important in both volcano hazard monitoring and scientific research. Traditionally, the size of a volcanic explosion is defined by the volume of explosive products, eruptive cloud height, and distribution of tephra. In an effort to make a uniform scale for volcanic eruptions, Newhall & Self (1982) coined the Volcanic Explosivity Index (VEI), a logarithmic scale from 1 to 8 which encompasses eruptions ranging from effusive Hawaiian (VEI I) through ultra-Plinian (VEI V and greater). McNutt (1994) investigated the reduced seismic tremor displacement (D_R) associated with eruptions of different VEI and determined an empirical relationship between VEI and reduced displacement (see equations 2.5 and 2.6 for definitions of reduced displacement):

$$\log_{10}(D_R) = 0.46(VEI) + 0.08 \tag{2.1}$$

Different eruptions may show substantial deviation from equation 2.1 because reduced seismic displacement is not always representative of the total energy budget. Variable conduit geometries, magma properties, and/or fragmentation depths can influence the amount of energy leeched into the seismic wavefield. Radiated acoustic energy may have to be incorporated into equation 2.1 to produce a more accurate relationship between remote observations and the VEI associated with an eruption.

Radiated acoustic energy may be recovered for situations where microphones are well-calibrated and are deployed in close proximity to the vent. Multiple microphones with azimuthal distribution about an explosion source can be used to understand and filter out the effects of atmospheric propagation on recorded acoustic pressure traces (refer to chapter 1). This chapter focuses on seismo-acoustic energy partitioning from three experiments with arrays of acoustic and seismic sensors: Karymsky in 1998 and 1999, and Erebus in 1999-2000. In each of these experiments, four to six microphones and seismometers were deployed within 3 km of the vent (see figure 2.1a-c) to quantify the energy propagating into the acoustic and seismic wavefields. In each experiment, more than 200 discrete Strombolian-type explosions were captured on acoustic and seismic

channels. Though individual explosions during the periods of study consist wholly of VEI I or VEI II events, material flux and radiated seismic and acoustic energies for the different explosions span several orders of magnitude. For more information on the volcanic history and field experiments conducted at Karymsky and Erebus, refer to chapter 3.

Examples of acoustic and seismic traces displayed in figure 2.2a-c illustrate the different eruptive styles at Erebus and Karymsky. In general, Erebus explosions are highly repeatable, short-duration, impulsive events, whereas Karymsky explosions frequently begin with an impulse and have codas of variable length. Karymsky explosions in 1998 possessed shorter codas than Karymsky explosions from 1999 and occurred about twice as frequently. The frequency of Karymsky explosions ranged from 8 to 20 per hour while Erebus produced an average of 5 explosions each day during the periods of observation.

2.3 Acoustic Reduced Pressure and Energy

The 'loudest' infrasound recorded during Strombolian-type eruptions generally does not exceed 100 Pa at distances of about 1 km (refer to chapter 1). For spherical spreading (an inverse relationship between excess pressure and radiation distance) these infrasonic pressure pertubations are small enough that the acoustic approximation is valid a few tens of meters from the explosion source. The acoustic approximation implies that linear propagation and acoustic pressure traces retain their shape as they radiate away from the source. For infrasound propagating in the atmosphere, spherical spreading can be perturbed by focusing or defocusing caused by atmospheric temperature and wind structure (refer to chapter 1). At distances of 2 km excess pressure magnification factors (MF's) are unlikely to exceed a factor of 2. But at offsets further than about 5 km, magnification factors can be infinitessimal and shadow zones may exist.
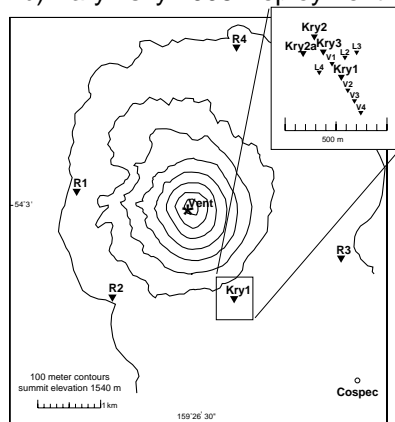
a) Erebus 1999-2000 Deployment
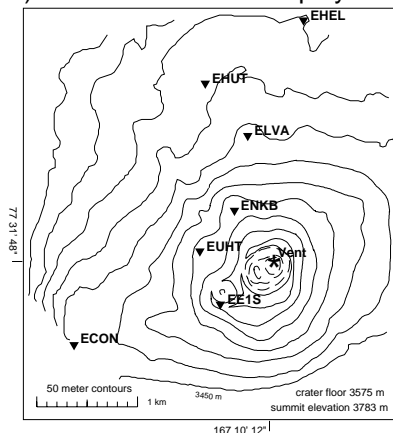
Erebus 1999-2000 Stations:

station	distance	hor. dist.	ver. dist.	comment
EE1S	670	660	100	
ENKB	690	670	150	
EUHT	1270	1260	150	seismic only
ELVA	1270	1230	300	seismic only
ECON	2080	2060	300	
EHUT	1900	1860	400	
EHEL	2430	2400	400	

b) Karymsky 1998 Deployment

Karymsky 1998 Stations:

station	distance	hor. dist.	ver. dist.	comment
Kry1	1620 m	1470 m	680 m	
Kry2	1360 m	1220 m	600 m	
Kry2a	1400 m	1260 m	610 m	
Kry3	1450 m	1300 m	640 m	
R1-4	1800-2800			temporary
L1-4	1520-1550			temporary
V1-4	1530-1890			temporary
COSPEC	3900 m	3800 m	900 m	

c) Karymsky 1999 Deployment
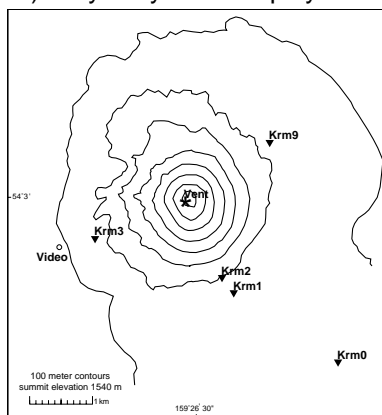
Karymsky 1999 Stations:

station	distance	hor. dist	ver. dist.	comment
Krm0	3630 m	3510 m	920 m	
Krm1	1620 m	1470 m	680 m	
Krm2	1360 m	1220 m	600 m	
Krm3	1760 m	1620 m	690 m	
Krm9	1820 m	1680 m	710 m	
Video	2200 m	2100 m	600 m	

Figure 2.1 Erebus and Karymsky Station Location Maps - Station deployment and information for the three experiments. Tables show distances to inferred explosion source location.

a) Erebus 1999–00 Explosion Examples

b) Karymsky 1998 Explosion Examples
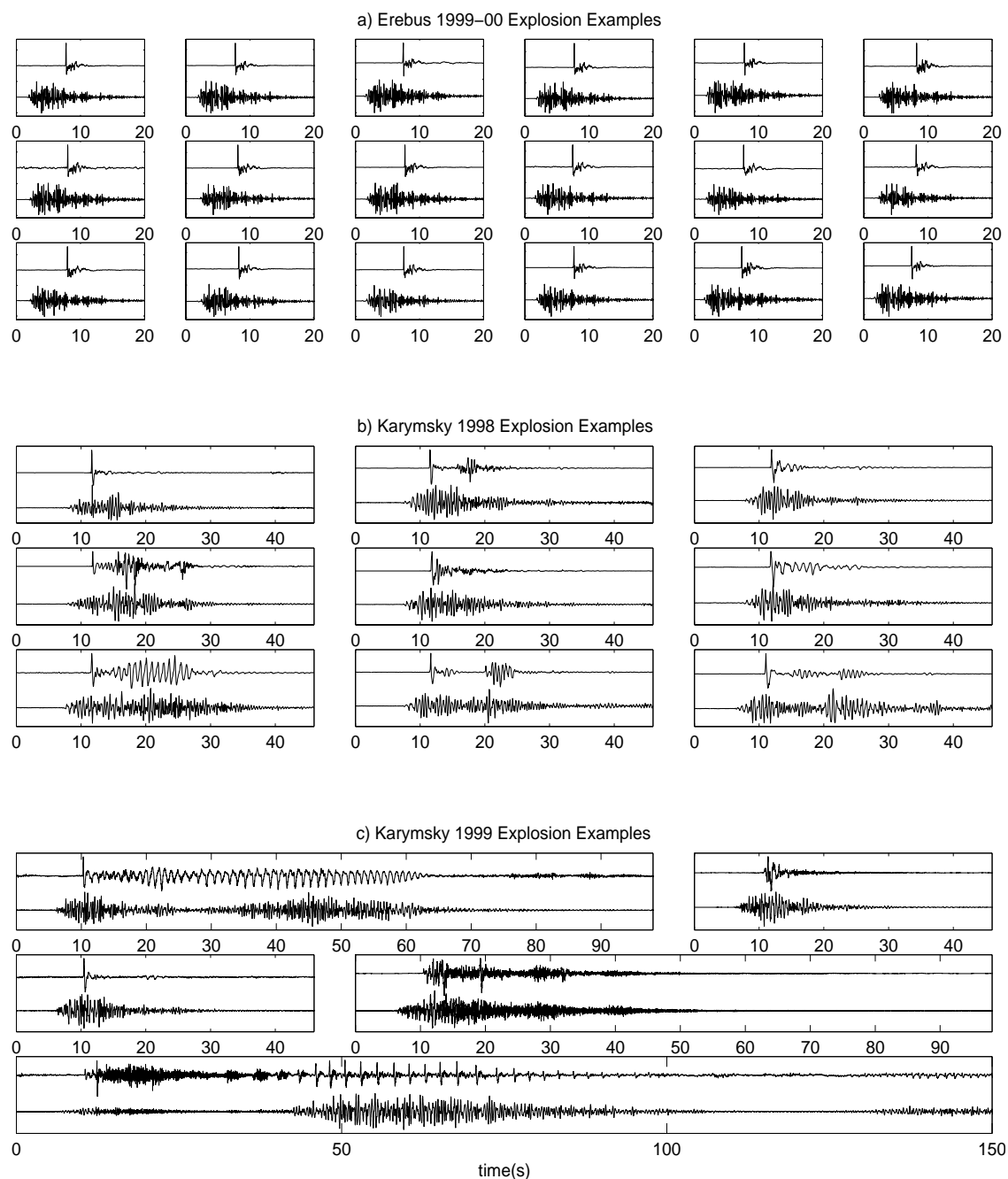

c) Karymsky 1999 Explosion Examples

time(s)

Figure 2.2 Erebus and Karymsky Explosion Examples - Example acoustograms and seismograms from degassing explosions at: a) Erebus 1999-2000 b) Karymsky in 1998, and c) Karymsky in 1999. Acoustic pressure waveforms (top traces) from stations a) EHUT, b) Kry1, and c) Krm3. Seismic velocity waveforms (bottom trace) from a) EE1S, b) Kry1, and c) Krm3. Events are selected based upon their high signal-to-noise ratio. All signals are recorded at stations located between 500 m and 2000 m from the vent.

At intermediate distances (1 km to 3 km), reduced pressures can be easily recovered from recorded acoustic pressure traces. Reduced pressure is analogous to reduced displacement [Aki & Koyanagi, 1981] and serves as an indicator of excess pressure close to the explosion source. For infrasonic pressure traces with an identifiable positive compression and negative rarefaction, the reduced pressure is defined according to the following formula (see appendix A).

$$P_R = \left(\frac{\Delta P_{max}}{MF}\right) \cdot \left(\frac{r}{r_o}\right) \tag{2.2}$$

ΔP_{max} = peak excess pressure (Pa) at recording site

MF = magnification factor due to atmospheric focusing

r = distance from source to microphone (m)

r_o = reduced distance (set at 1 meter in this chapter)

One meter is a sensible reduced pressure distance for Strombolian eruptions because it is the approximate dimension of a bubble burst or vent opening for small explosions [Sparks, 1997]. Although the acoustic approximation may not be quite valid at one meter, reduced pressure serves as an effective comparative measurement.

The radiated acoustic energy recovered from infrasonic pressure traces is another useful quantity because it considers energy contributions from the total waveform. An acoustic record with an extended coda indicates an event with degassing signals that are not reflected in the reduced pressure measurement. The total acoustic energy is proportional to the integrated square of the excess pressure time function. For a hemispherical source radiating energy into the atmosphere with known magnification factor (MF), the total radiated acoustic energy is (see appendix A):

$$E_a = \frac{2\pi r^2}{\rho_a c} \int \frac{\Delta P^2}{MF^2} dt \tag{2.3}$$

ρ_a = air density (1.189 kg/m^3 at standard temperature and pressure)

c = sound speed (340 m/s at standard temperature and pressure)

Unfortunately, acoustic pressure traces frequently suffer from noise caused by wind (see appendix B). Because wind noise is broad-band and impossible to remove during post-processing, accurate acoustic energy determinations may only be made for traces with good signal-to-noise ratios.
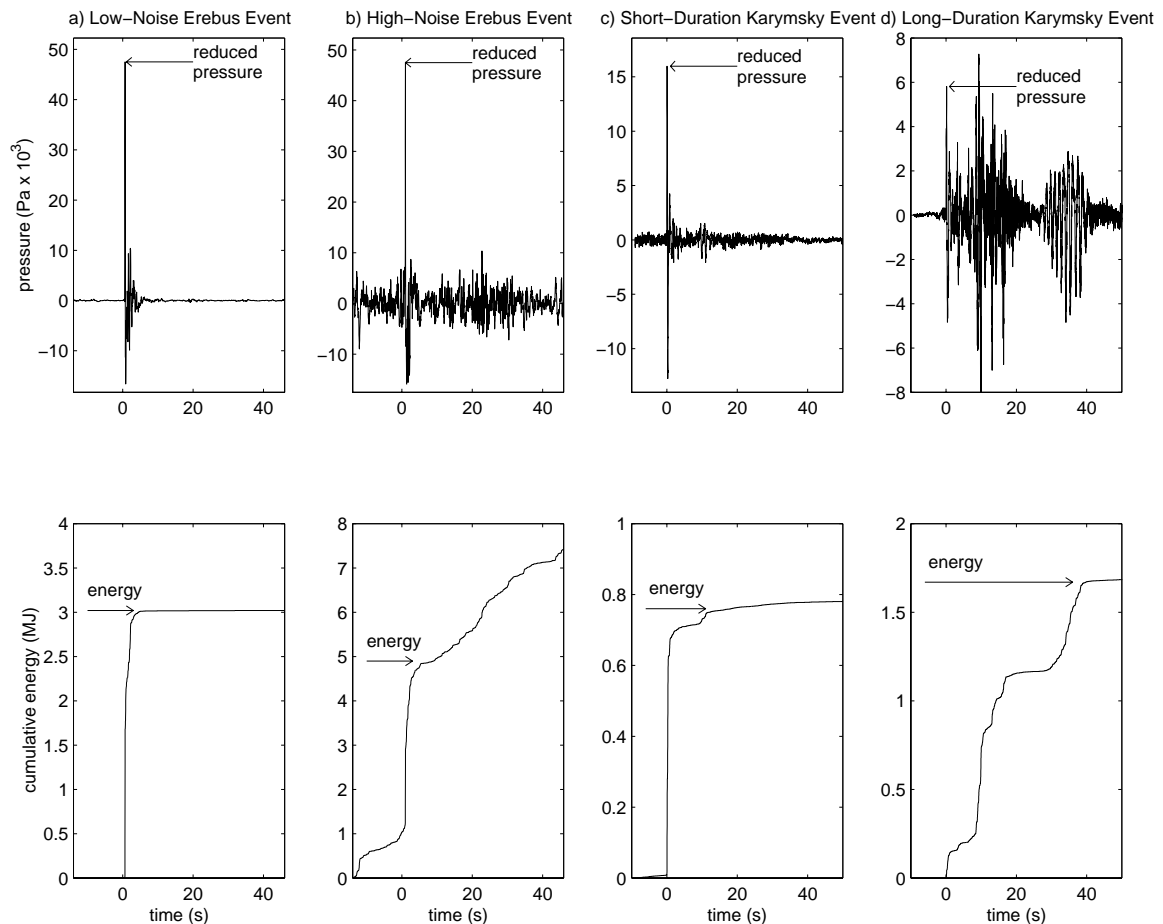

Figure 2.3 Acoustic Reduced Pressure and Energy - Reduced pressure traces (top) and cumulative energy plots (bottom) for two explosions at both Erebus and Karymsky. Reduced pressure is the maximum excess pressure after applying a correction for propagation distance and atmospheric focusing. Radiated acoustic energy is derived from the integrated square of the pressure trace. The Erebus explosion examples consist of: a) a good signal-to-noise event and b) a poor signal-to-noise event. The low-noise explosion is more appropriate for accurate energy calculations. The Karymsky explosions illustrate the differences between c) a short-duration event and d) an event with extended coda. Despite having a smaller reduced pressure, the long-duration event has greater total energy than the short-duration event.

A comparison between reduced pressure and acoustic trace energy is provided in figure 2.4 to illustrate the differences in the two parameters. The relationship between reduced pressure and acoustic trace energy is best fit by a parabolic curve with a constant (k) that is dependent upon the particular data suite:

$$E_A = kP_R^2 \qquad (2.4)$$

where:

$$E_{A(ERE)} = 1400 \times P_{R(ERE)}^2 \text{ with a standard deviation for k of 26\%.}$$

$$E_{A(K98)} = 5700 \times P_{R(K98)}^2 \text{ with a standard deviation for k of 81\%.}$$

$$E_{A(K99)} = 7300 \times P_{R(K99)}^2 \text{ with a standard deviation for k of 64\%.}$$

The constant (k) is low for explosions which have high reduced pressure and low acoustic trace energy. Erebus explosions have low values for k because the codas are short. Erebus explosions deviate only slightly from the best fit line because of the self-similarity of different acoustic events. Deviation from the best fit line for Karymsky explosions in 1998 and 1999 is significant and can be attributed to variable coda length. Because of the non-unique relationship at Karymsky, acoustic excess pressure alone can not be used to accurately estimate the radiated acoustic energy.

2.4 Seismic Reduced Displacement and Energy

Seismic reduced displacement is analogous to acoustic reduced pressure because both are measures of maximum amplitude at a fixed distance. Reduced displacement (D_R) for body waves may be defined as follows [Aki & Koyanagi, 1981]:

$$D_R = \frac{A \cdot r}{2\sqrt{2}} \qquad (2.5)$$

A = displacement amplitude in cm

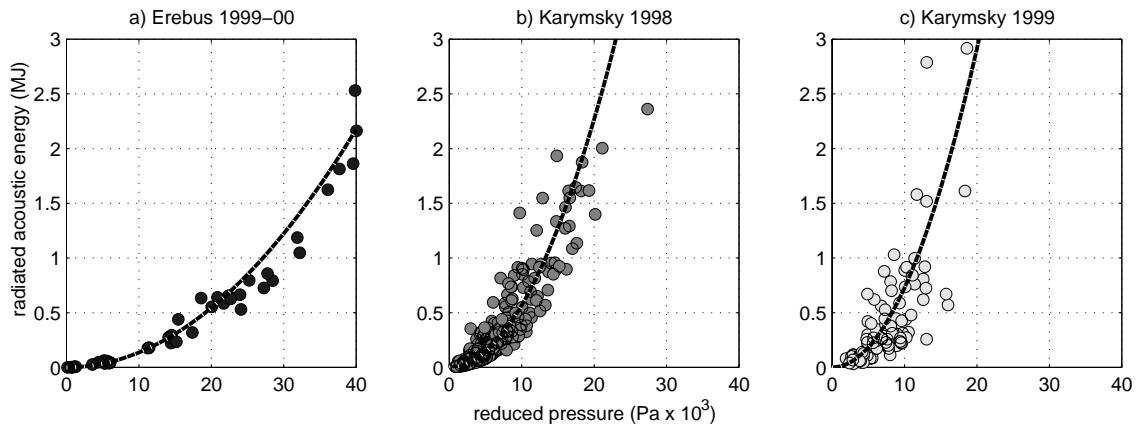r = distance from source to seismic station in cm

Figure 2.4 Reduced Pressure vs. Acoustic Energy - Reduced acoustic pressures at one meter (x-axis) plotted against radiated acoustic energy (y-axis) for: a) 49 Erebus 1999-2000 explosions recorded at EHUT (1900 m from vent), b) 272 Karymksy 1998 explosions recorded at Kry1 (1620 m from vent), and c) 106 Karymsky 1999 explosions recorded at Krm3 (1760 m from vent). Lines are best fit parabolic curves according to equation 2.4.

And reduced displacement for surface waves is defined according to Fehler (1983):

$$D_R = \frac{A \cdot \sqrt{\lambda \cdot r}}{2\sqrt{2}} \tag{2.6}$$

λ = wavelength in cm

For seismograms at intermediate distances from the explosion source (1 to 3 km), the formulas for either body wave or surface wave reduced displacements are oversimplified because seismic traces are a complex combination of wave types [Chouet et al., 1998]. However, body wave reduced displacements appear to be a better model for Erebus explosion earthquakes. Figure 2.5c,d illustrates reduced seismic displacement calculations for six stations located on the flanks of Erebus according to equations 2.5 and 2.6. Although the decay of seismic displacements with distance is somewhat ambiguous because of uncertain site responses and radiation patterns, reduced displacements are more consistent for body wave amplitudes that decay inversely with radius. Thus body wave reduced displacements will be used exclusively in this chapter for both Erebus and Karymsky.
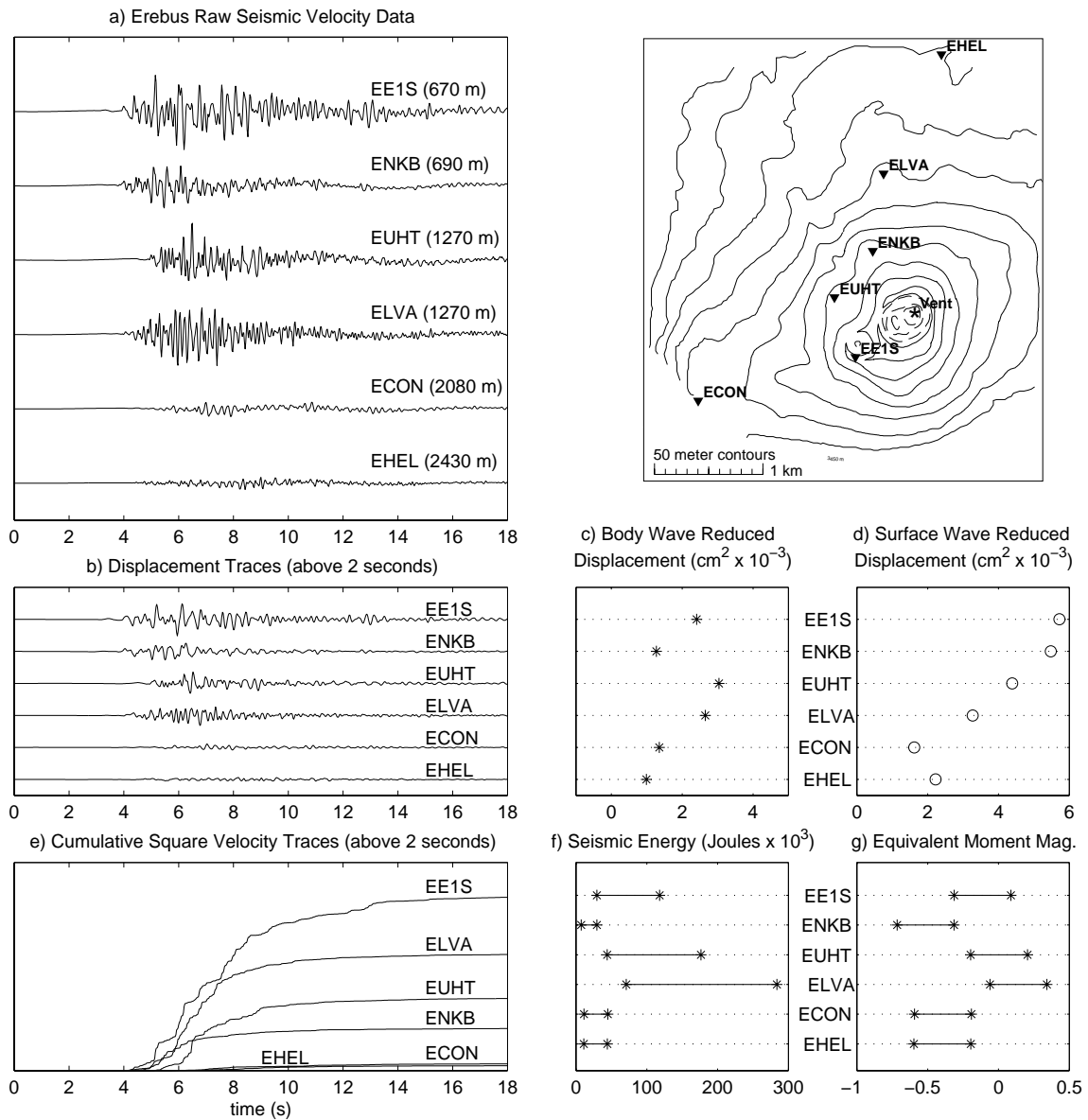
Figure 2.5 Seismic Reduced Displacement and Energy - a) Raw seismic traces recorded at six stations for an explosion at Erebus Volcano. b) Displacement traces and corresponding reduced displacements for c) body waves and d) 1-second surface waves. Reduced displacement values at the six stations appear more consistent for the body wave formula (equation 2.5). e) Cumulative squared velocity traces (filtered above 2 seconds to remove tidal noise) and f) corresponding seismic body wave energy (for phase velocities ranging from 500 m/s to 3000 m/s calculated according to equation 2.7). g) Body wave energy estimates converted to equivalent moment magnitude ($M_o = (\log(E_s) - 4.94)/1.5$ [Lay & Wallace, 1995]).

As for radiated acoustic energy, the radiated seismic energy is dependent upon the time duration of the seismic coda. For non-dispersive elastic waves in the earth, energy is proportional to the integrated square of the velocity trace [Lay & Wallace, 1995]. Approximate seismic energy release can be determined if assumptions are made about the radiation pattern of seismic waves, intrinsic seismic wave velocity, and seismometer site response. For body waves generated by an isotropic source at the top of a homogeneous half space, total energy is proportional to [Boatwright, 1980]:

$$E_s = 2\pi r^2 \rho_e V \int (SU)^2 dt \tag{2.7}$$

ρ_e = density of ground

V = body wave velocity

S = site response

U = particle velocity

Because the bulk of the recorded ground displacement appears to be body waves and not surface waves (refer to figure 2.5c-d), seismic energy estimates in this chapter use equation 2.7 exclusively. In figure 2.5f, seismic trace energy is calculated for body wave velocities ranging between 500 m/s and 3000 m/s [Dibble, 1994; Johnson & Lees, 2000]. In both cases, ground density is estimated as 2500 kg/m^3 and the site response (s) is assumed to be unity.

Unfortunately, precise calculation of energy contained within a seismic trace is difficult due to the unknown seismometer site responses. The most reliable method of assessing site response is to calibrate site responses with earthquakes of known magnitudes. However, during the field seasons at Erebus and Karymsky, local and regional earthquakes are almost wholly absent. Only one local earthquake is evident in the records of Karymsky during the three field seasons. This particular earthquake suggests that a unity site response (s) is appropriate (see appendix C). However, throughout this chapter, seismic energy release should be considered accurate only to within an order of magnitude.

The relationship between reduced seismic displacements and radiated seismic inferred from seismic traces is displayed in figure 2.6 for the three datasets. As in the comparison between reduced acoustic pressure and radiated acoustic energy, a best fit line can be defined by a parabola:

$$E_A = kD_R^2 \tag{2.8}$$

where:

$$E_{A(ERE)} = 187 \times D_{R(ERE)}^2 \text{ with a standard deviation for k of 30\%.}$$

$$E_{A(K98)} = 136 \times D_{R(K98)}^2 \text{ with a standard deviation for k of 37\%.}$$

$$E_{A(K99)} = 86 \times D_{R(K99)}^2 \text{ with a standard deviation for k of 45\%.}$$

Deviation from the best fit line is smallest at Erebus indicating self-similarity of seismic waveforms despite variable explosion sizes.
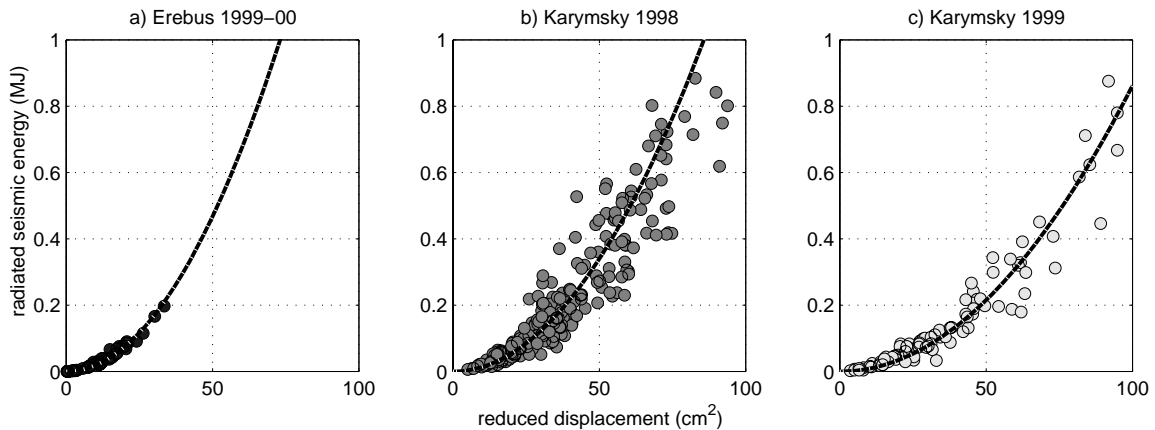
Figure 2.6 Reduced Displacement vs. Seismic Energy - Reduced displacements (x-axis) plotted against radiated seismic energy (y-axis) for: a) 64 Erebus 1999-2000 explosions recorded at EE1S (670 m from vent), b) 427 Karymksy 1998 explosions recorded at Kry1 (1620 m from vent), and c) 189 Karymsky 1999 explosions recorded at Krm3 (1760 m from vent). Lines are best fit parabolic curves with origin at zero according to equation 2.8.

Though seismic waves are subject to the vagaries of propagation and site response, ground propagation filters (unlike atmospheric propagation filters) remain relatively

constant over time. Differences between seismic explosion waveforms must then only be attributed to differences in the explosion source. For Strombolian explosions at Erebus, the source is confined to the surface of the lava lake where large bubble bursts have been observed [Dibble, 1994]. Seismic radiation from such a source should be isotropic and is evidenced by consistent radiation at azimuthally distributed seismic stations at Erebus (see figure 2.7a). At Karymsky, however, seismic radiation is less consistent (see figure 2.7b). Though explosions probably originate in the uppermost meters of the Karymsky conduit [Sparks, 1997], there appears to be directionality associated with certain explosions, a behavior that is more consistent with earthquake sources in a solid than in a fluid. Azimuthally distinct stations have a standard deviation from a fixed seismic radiation ratio of 32% at Karymsky compared to only 15% at Erebus. Though the deviation at Karymsky is more significant than at Erebus, it will be shown in the next section that variations in seismo-acoustic energy partitioning at the explosion source are much greater.
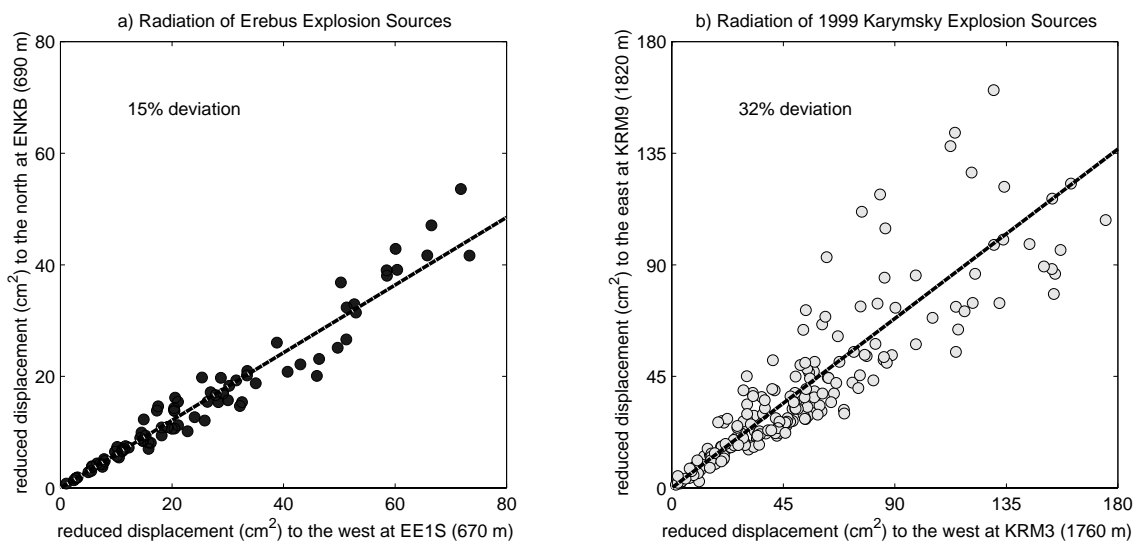
Figure 2.7 Seismic Source Directionality - Display of reduced seismic displacements for two azimuthally distinct seismic stations at: a) Erebus (90 degree aperture, 84 explosions) and b) Karymsky in 1999 (170 degree aperture, 207 explosions).

2.5 Seismo-acoustic Reduced Amplitude Scatter at Karymsky and Erebus

It is possible to observe significant scatter in raw seismo-acoustic amplitude ratios for suites of explosions recorded at Erebus, Karymsky, and many other volcanoes (Langila, [Mori et al., 1989], Arenal [Garces et al., 1998a], Unzen [Yamasato, 1998]) before accounting for atmospheric propagation effects. Some explosions appear infrasonically 'loud' with small seismic displacements while others are 'quiet' with relatively large seismic displacements. In raw data collected at Strombolian-type volcanoes, seismo-acoustic reduced amplitude ratios may span several orders of magnitude for stations located only a few kilometers from the explosion source (see figures 2.8 and 2.11). The scatter in seismo-acoustic amplitude ratios is due to the combined influences of atmospheric propagation effects and explosion source variability. Impressive scatter is evident in the data recorded at Karymsky Volcano in 1998 and 1999, but is relatively insignificant for data recorded at Erebus Volcano in 1999-2000 (see figure 2.8). Atmospheric propagation effects may be responsible for the minimal scatter in seismo-acoustic amplitude ratios at Erebus, but differences in source-energy partitioning are the likely explanation for the marked scatter in seismo-acoustic amplitude ratios at Karymsky.

The relationship between reduced acoustic pressures and reduced seismic displacements can be used to quantify the acoustic efficiency (relative to seismic) for a particular suite of explosions. A linear relationship ($D_R = kP_R$) can be used to describe the relationship between the mean reduced pressure and mean reduced displacement:

$$D_{R(ERE)} = 0.0005 \times P_{R(ERE)} \text{ with a standard deviation of 30\%.}$$

$$D_{R(K98)} = 0.0071 \times P_{R(K98)} \text{ with a standard deviation of 59\%.}$$

$$D_{R(K99)} = 0.0053 \times P_{R(K99)} \text{ with a standard deviation of 56\%.}$$

From the data presented in figure 2.8, it is apparent that the acoustic efficiency at Erebus is greater than at Karymsky by about an order of magnitude. It is also evident that the
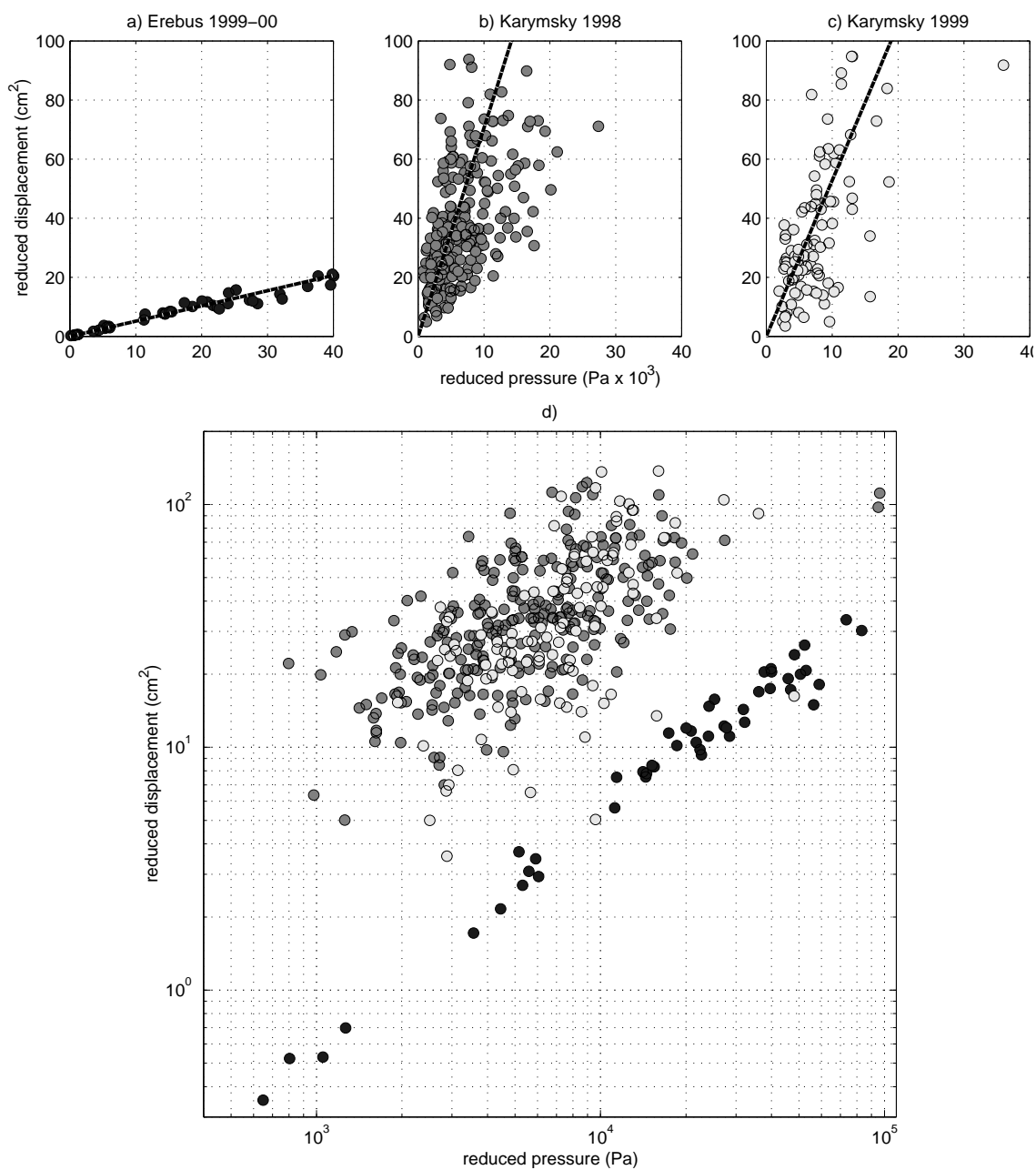
Figure 2.8 Reduced Pressure vs. Reduced Displacement - Reduced acoustic pressures at one meters (x-axis) plotted against reduced seismic displacement (y-axis) for: a) 64 Erebus 1999-2000 explosions (dark) recorded at EHUT (acoustic, 670 m from vent) and EE1S (seismic, 1900 m from vent), b) 427 Karymksy 1998 explosions (grey) recorded at Kry1 (1620 m from vent), c) 189 Karymsky 1999 explosions (light) recorded at Krm3 (1760 m from vent), and d) a logarithmic plot of all three datasets. Linear best fit lines are shown in panels a-c.

deviation from a fixed seismo-acoustic amplitude ratio is greater at Karymksy than at Erebus. The deviation in seismo-acoustic amplitude ratios at Karymsky (59% in 1998 and 56% in 1999) is more significant than the seismic scatter attributed to variable seismic source radiation directivity (see figure 2.7).

Deviation from a fixed seismo-acoustic ratio at Erebus is small enough that it may be wholly attributed to the effects of atmospheric transmission. A magnification factor (MF) of 1.5 is sufficient to bring 95 percent of Erebus explosions into a fixed ratio defined by the relationship $(R_{D(ERE)} = 0.0005 \times R_P)$. The filtering effects of variable atmospheric conditions may be observed by comparing the reduced pressures for an array of microphones distributed about Erebus. For a suite of explosions, two microphones co-located at a single station record similar excess pressures (figure 2.9a), but two stations separated from each other are subject to the influences of atmospheric propagation filters and thus record varying pressures (figures 2.9b-c). Transmission distances affect the degree to which atmospheric structure influences infrasonic amplitudes (refer to chapter 1). At further offsets, larger deviation in seismo-acoustic amplitude ratios is observed.

Deviation from a fixed seismo-acoustic ratio is considerable at Karymsky (see figures 2.8b,c and 2.11b,c) and can not be entirely attributed to variable atmospheric structure. Assuming realistic temperature or wind gradients in the vicinity of the volcano, geometric focusing should not significantly affect infrasonic pressure amplitudes for stations located within a couple of kilometers of the vent (refer to chapter 1, figure 1.5). A magnification factor (MF) of 1.5 is an appropriate maximum correction for conditions at Erebus and Karymsky where microphones were deployed within 2 km of the source and weather conditions were relatively calm (acoustic explosion signals recorded during stormy conditions are not considered because they are usually obscured by wind). Figure 2.10 shows bounds (dashed lines) corresponding to a MF of 1.5 for a suite of Erebus and Karymsky explosions. The points that fall within the dashed lines indicate explosions which may have constant seismo-acoustic source radiation. It is evident that many
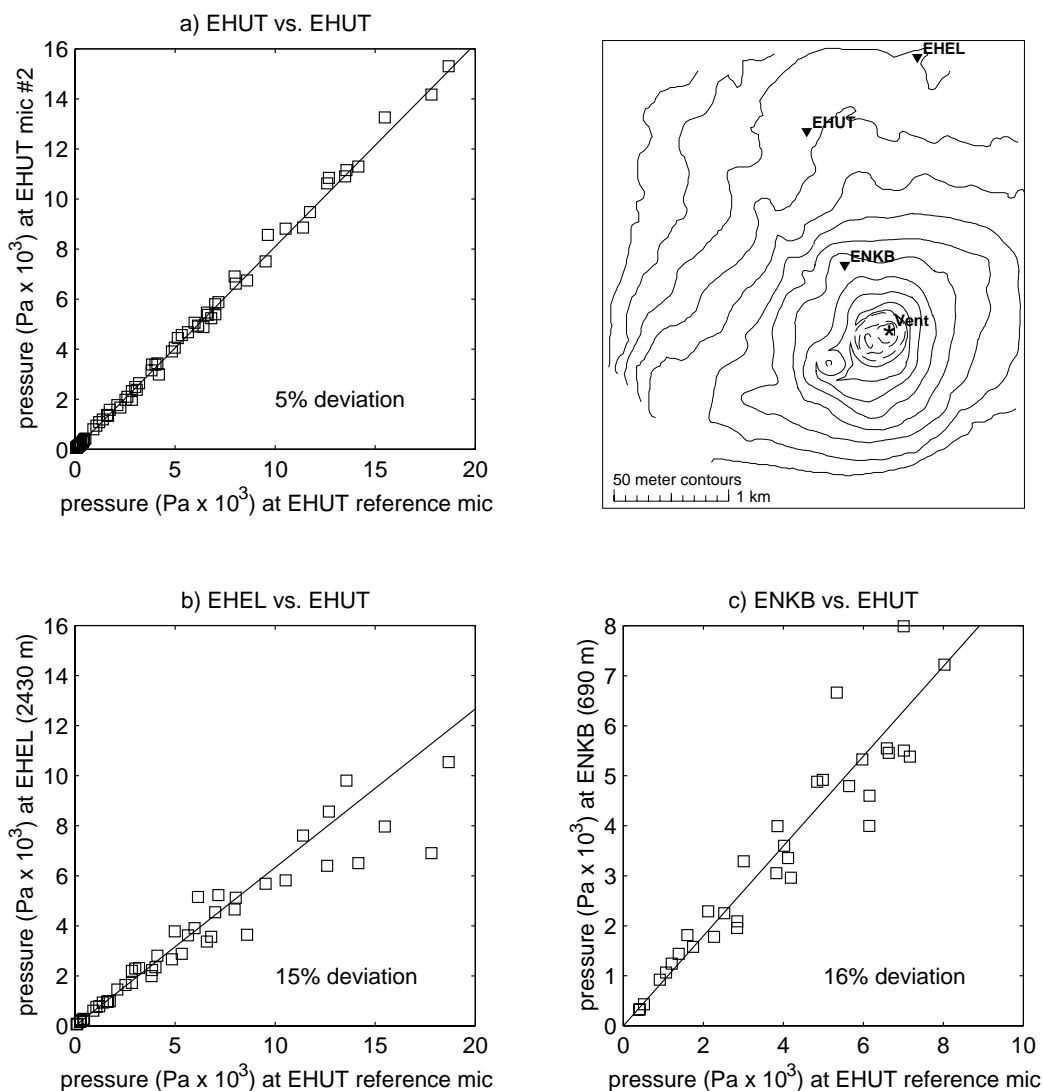
Figure 2.9 Reduced Pressure Variability Due to Wind - a) Acoustic pressure amplitudes from two microphones co-located at EHUT (1900 m from vent) indicate similar excess pressures because they sample the same airwaves. b-c) Microphones that are spatially separated sample variable excess pressures suggesting that atmospheric propagation has an important filtering effect on acoustic amplitudes. Acoustic pressures are bandpassed between 4 Hz and 5 Hz and reduced to distances of one meter for comparison.

explosions at Karymsky lie outside this region. For these events, the deviation in seismo-acoustic amplitude ratios can not be solely attributed to geometric focusing. Much of the variability in seismo-acoustic amplitudes must then be due to variable mechanisms for source-energy partitioning.
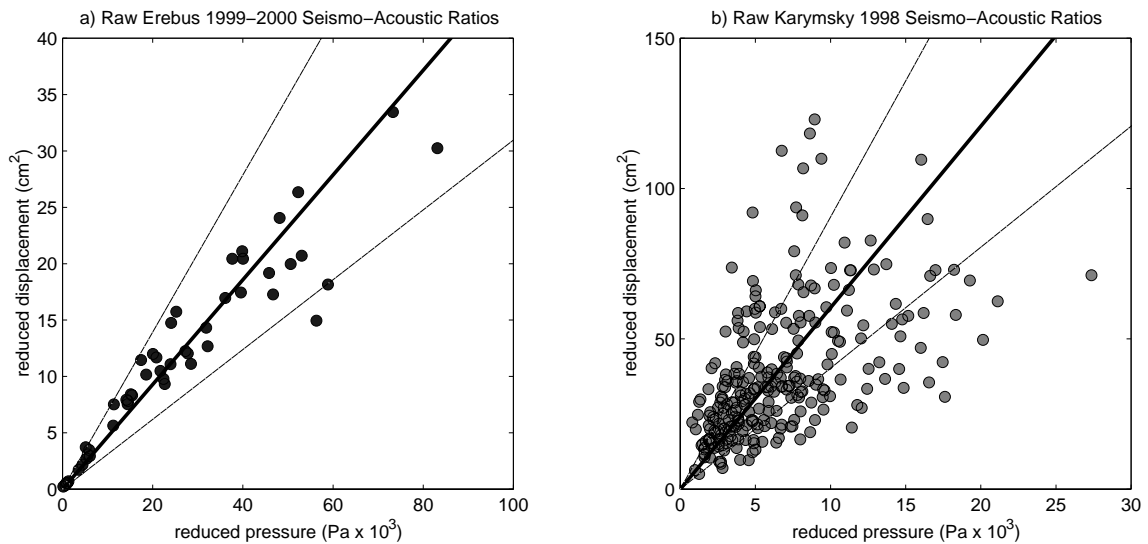
Figure 2.10 Seismo-acoustic Scatter at Erebus and Karymsky - a) Acoustic reduced amplitudes are plotted against reduced displacements for a) 49 explosions at Erebus recorded at EHUT (1900 meters from vent) and b) 270 explosions at Karymsky in 1998 recorded at Kry1 (1620 meters from vent). Solid line is a best fit for each suite of explosions. Dotted lines represent the possible deviation in acoustic pressures due to an arbitrary magnification factor (MF) of 1.5.

Though the relationship between acoustic and seismic reduced amplitudes offers insight into the partitioning of the seismo-acoustic explosion source, it is ultimately the relationship between the energy contained in the seismic and acoustic wavefields that is most important. Unfortunately, accurate determination of total acoustic and seismic energies is difficult because acoustic traces are often corrupted by noise and adequate site responses are lacking for Karymsky and Erebus seismic stations. Figure 2.11 shows comparisons of best estimates for radiated seismic and acoustic energy interpreted from seismic and acoustic traces for a low-noise subset of the three suites of explosions.

According to figure 2.11, energy partitioning for the three datasets can be summarized by the following linear relationships:

$$E_{S(ERE)} = 0.03 \times E_{A(ERE)} \text{ with a standard deviation of } 40\%.$$

$$E_{S(K98)} = 1.18 \times E_{A(K98)} \text{ with a standard deviation of } 121\%.$$

$$E_{S(K99)} = 0.52 \times E_{A(K99)} \text{ with a standard deviation of } 87\%.$$
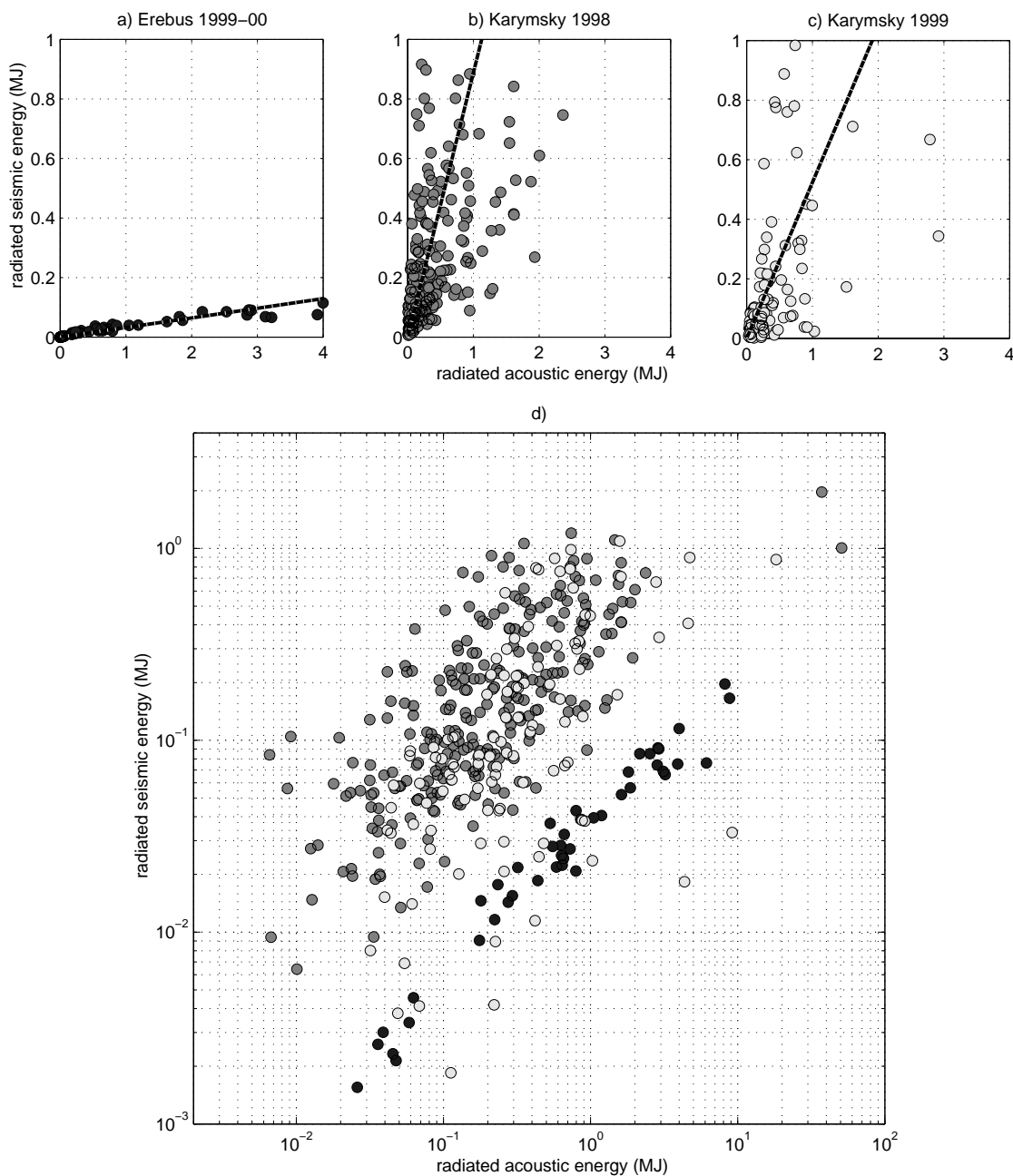
Figure 2.11 Acoustic Trace Energy vs. Seismic Trace Energy - Radiated acoustic energy (x-axis) plotted against radiated seismic energy (y-axis) for: a) 49 Erebus 1999-2000 explosions (dark) recorded at the EHUT microphone (670 m from vent) and EE1S seismometer (1900 m from vent), b) 272 Karymksy 1998 explosions (grey) recorded at Kry1 (1620 m from vent), c) 106 Karymsky 1999 explosions (light) recorded at Krm3 (1760 m from vent), and d) a logarithmic plot of all three datasets. Linear best fit lines are shown in panels a-c. Acoustic energies are calculated according to equation 2.3 and seismic energies are calculated according to equation 2.7.

For explosions at Karymsky Volcano, the average partitioning of energy between acoustic and seismic wavefields is approximately equal, with a slightly greater acoustic efficiency in 1999. In this context, acoustic efficiency is defined as the relative apportioning of radiated acoustic energy compared to radiated seismic energy. Compared to Karymsky, explosions at Erebus were consistently able to propagate a much more significant portion of their explosion energy into the atmosphere. Reasons for the extremely high acoustic efficiency at Erebus relative to Karymsky will be discussed in detail in a section 2.12.

2.6 Comparison of Seismic and Acoustic Amplitudes with Visual Records

Ejection velocities and plume volume growth can be recovered from the digitized video of volcanic explosions at Karymsky Volcano. Ejection velocity, akin to muzzle velocity, is an important parameter that is traditionally sought in volcanic investigations because it provides information about volcanic explosivity and vent overpressures [Wilson, 1980]. Muzzle velocities are typically determined through tedious field work mapping tephra and bomb sizes against flight distances. To recover muzzle velocities, much speculation about the duration of thrust forces and projectile aerodynamics is necessary. Digital image processing, first employed at Stromboli Volcano [Ripepe et al., 1993], offers a more efficient means of estimating the muzzle velocities of projectiles and gas. In conjunction with information about the plume density and composition, vital parameters, such as total material flux and kinetic energy, may be estimated.

A Sony CCD-TRU75 Hi8 camcorder was used to film Karymsky explosions during three consecutive nights in 1999, resulting in footage of 90 distinct explosions, 35 which are accompanied by high quality infrasonic records (see summary in table 2). All explosions were filmed from the same promontory, 600 meters below and 2200 meters from the vent (see figure 2.12). All events were filmed with an infrared-sensitive night vision filter which was able to adequately record the incandescence from ballistics and hot ash clouds while remaining at a fixed exposure. Using the full optical zoom, frame dimensions at

the vent were approximately 90 meters by 60 meters. Accurate video timing (to within 0.1 seconds) was accomplished by calibration of the camera's internal clock with GPS time. Footage from the series of nighttime explosions was transferred to mini-DV and digitized at 0.1 second intervals to still images for analysis.

Figure 2.12 Photo of Karymsky Video Site - View of Karymsky from video recording site, situated ~2300 meters from the vent. Box shows the field of view of the digitized video frames.

Two important quantities are easily recovered from the video data: the time series of the relative luminescence of explosions and gas and ballistic emission velocities. Relative luminescence is defined as the average pixel brightness across the field of view (grayscale pixel values range from 0 to 255). In the absence of an eruption, average background luminescence is about 27 out of 255. The time series of relative luminescence offers a means of comparing material emissions from the vent with acoustic and seismic traces. Fluctuations in acoustic energy are clearly associated with emissions of luminescent juvenile material (see figure 2.13). Bright flashes and the impulsive ejection of material correspond to high-amplitude infrasonic pulses while

continuous jetting of gas is often associated with broad-band acoustic tremor. The relationship between seismic and video is less obvious because the explosion source is strongly filtered by seismic propagation filters within the volcano [Johnson & Lees, 2000].
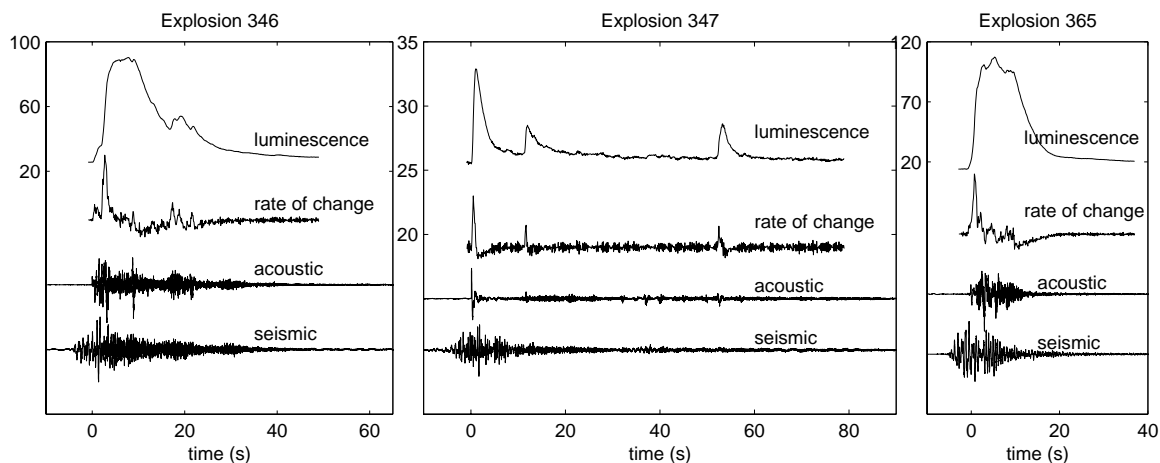

Figure 2.13 Video Luminescence Time Series - Three explosions recorded acoustically, seismically, and with video. In addition to normalized acoustic pressure and seismic velocity traces, the plots show a luminescence time series (units are average pixel grayscale levels out of 255) and the time-derivative of the luminescent time series. Acoustic and seismic time series have been advanced by 5 seconds to better illustrate correlation with the luminescence time series.

Gas and ballistic ejection velocities can be recovered from the digitized video by measuring the growth rate of the incandescent plume during the first second of visible emissions. Only a small portion of the crater (less than ~500 cubic meters and ~5 meters of depth) is hidden from the camera's vantage point. As a result, the explosion onset determined from video lags behind the onset of material emission by less than 0.1 s (one frame) for the more powerful explosions. For the calculation of ejection velocities, the areal growth of ejected material is evaluated for each still image by counting the number of pixels which surpass a threshold value. False-color grayscale images are constructed for pixels which surpass a grayscale threshold of 30, 60, 100, and 150 out of a possible 255 grayscale levels (see figure 2.14a). The minimum useful threshold level is about 30

because it is slightly brighter than the background average nighttime level. This minimum threshold appears to be satisfactory for all but the smallest explosions where the ratio of dark gas to incandescent ejecta is especially high and portions of the plume can be obscured by dark gas emissions. During most explosions, luminescent pixel areas are biased to some degree by dark clouds of gas which leak from the vent several seconds after the explosion onsets. Fortunately, opaque emissions do not tend to corrupt the explosion onsets. The explosion onsets are the most critical time interval for evaluation of the incandescent plume growth because they corresponds to the initial impulsive acoustic blasts that are usually associated with the highest acoustic excess pressures. The three events displayed in figure 2.14 provide examples of areal plume growth during the very onset of Karymsky explosions. Corresponding acoustic and seismic trace are provided for comparison.

The areal extent of incandescent material can be converted to plume volume and material ejection velocities for a plume expansion which is approximated as hemispherical. The volume of incandescent material is related to the area of incandescence by (see appendix A):

$$V_I = \sqrt{\frac{32}{9\pi}} A_I^{3/2} \tag{2.9}$$

$$A_I = \text{area of incandescence (8 pixels per meter)}$$

And the plume ejection velocity is related to the expansion of the area occupied by incandescent pixels (see appendix A):

$$U_M = \frac{1}{\sqrt{2\pi A_I}} \left(\frac{dA_I}{dt} \right) \tag{2.10}$$

For consistency, the maximum velocity during the first second of an explosion is used for all muzzle velocity calculations at Karymsky in 1999. During the onset of these explosions, an expanding incandescent cloud precedes bombs for the first few tenths of seconds of an explosion. As air resistance slows the progression of finer particles, individual bombs begin to outrace the expanding ash/gas cloud front (see explosions 356
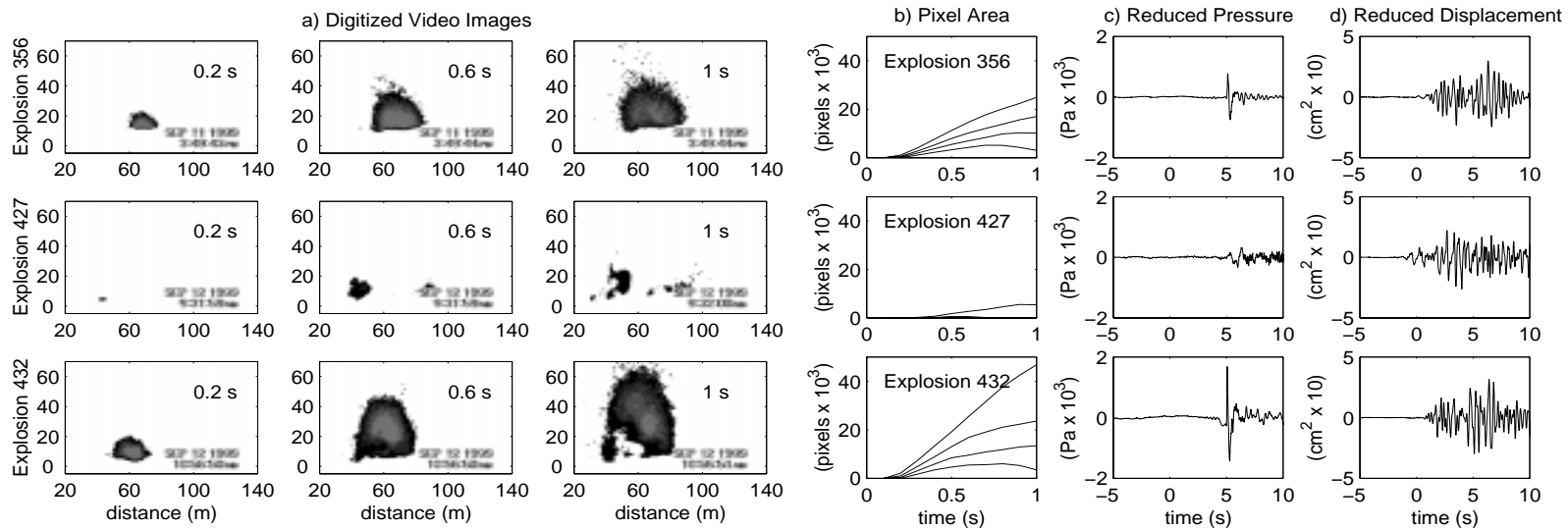
Figure 2.14 Seismo-acoustic-video Comparison - a) False-color image of three different explosions together with their associated b) video, c) acoustic, and d) seismic data. Image frames are displayed at 0.4 second intervals. Clock stamp at lower right of frames is 0.2 seconds fast relative to GMT. Grayscale contours in each individual image correspond to pixel threshold values of 30, 60, 100, and 150 out of 256. b) Raw pixels areas occupied by each grayscale level (8 pixels equals one meter). c) Associated acoustic pulses and d) seismic traces recorded at Krm3 (1760 m from vent). Plots b-d are all plotted using the same time scale. Visual emissions precede acoustic waves by about 5 seconds and seismic waves by about 1 second for 1760 meter propagation distance.

and 432 in figure 2.14). At this time, individual ballistic projectile velocities could be recovered from the digitized still images. However the selection of individual bombs introduces a whole series of complications involving which bombs should be sampled, the determination of the projectile trajectory planes, and aerodynamic efficiencies [Ripepe et al., 1993; Wilson, 1980]. Gas plume ejection velocities are a more robust measurement and are representative of explosivity. The 1999 video records summarized in table 2 indicate a maximum gas plume ejection velocity of approximately 27 m/s during the first second of an explosion.

Table 2 Video Data - A summary of statistics for 35 Karymsky explosions that are accompanied by high-quality acoustic records and have ejection velocities in excess of 5 m/s. For each explosion, reduced pressures at one meter and seismic reduced displacements are compared with the area occupied by incandescent pixels area after 1 second of explosion (64 pixels^2 = 1 m^2), the gas volume occupied after 1 second of eruption, the maximum ejection velocity during the first 1 second of the explosion, and the brightness index (%). The brightness index is defined as the percentage of the incandescent pixels which exceed a grayscale value of 60.

Explosion Times (day:hr:mn:sec)	Explosion Number	Reduced Pressure (Pa)	Reduced Displacement (cm^2)	Pixel Area (pixel^2)	Volume (m^3)	Ejection Velocity (m/s)	Brightness Index (%)
254:09:27:02	328	825	29	21958	6760	33	45
254:09:53:55	329	934	58	8271	1560	22	36
254:10:00:34	330	322	20	14873	3770	24	43
254:10:12:07	331	603	15	9978	2070	26	22
254:10:27:42	333	704	9	13049	3100	27	33
254:12:24:34	340	957	25	23391	7430	39	40
254:12:38:08	341	248	15	7502	1350	14	3
254:13:24:55	343	3794	105	61552	31730	59	61
254:13:51:35	346	1309	13	29097	10310	30	48
254:13:57:58	347	852	5	28922	10220	37	60
254:14:10:39	348	339	22	5413	830	17	10
254:15:08:36	354	227	14	1667	140	21	9
254:15:32:03	355	433	25	2864	320	23	13
254:15:49:43	356	872	31	20153	5940	33	69
254:16:29:35	359	407	25	4867	710	20	11
254:16:35:45	360	673	27	14745	3720	30	68

Table 2 (continued) Video Data

Explosion Times (day:hr:mn:sec)	Explosion Number	Reduced Pressure (Pa)	Reduced Displacement (cm^2)	Pixel Area $(pixel^2)$	Volume (m^3)	Ejection Velocity (m/s)	Brightness Index (%)
254:16:57:42	361	808	23	11112	2430	25	56
254:17:01:48	362	485	21	2712	290	21	23
254:17:22:31	365	989	73	15312	3940	24	55
254:17:34:05	366	636	20	14231	3530	24	55
254:17:44:48	367	1070	74	26078	8750	41	64
255:08:37:33	423	1026	43	17466	4800	45	28
255:09:02:20	425	590	9	1142	80	14	3
255:09:31:59	427	379	43	4628	650	16	14
255:09:56:47	429	1155	54	13159	3140	26	60
255:10:31:27	430	826	31	16687	4480	36	37
255:10:56:50	432	1681	34	37658	15180	46	56
255:11:34:57	435	261	12	1768	150	15	36
255:12:37:56	440	479	3	7931	1470	18	54
255:12:53:43	441	1024	12	8974	1770	22	73
255:13:09:42	442	425	22	7143	1250	17	57
255:13:48:02	445	450	7	5262	790	20	61
255:14:27:59	447	987	89	11524	2570	29	62
255:14:35:11	448	673	44	2637	280	26	14
255:14:54:40	449	1004	117	9484	1920	26	52

Gas plume ejection velocities from Karymsky explosions scale very well with acoustic amplitudes, but not well with seismic amplitudes as evidenced by comparisons of reduced pressures (see figure 2.15a,c) and reduced displacements (figure 2.15b,d) with maximum ejection velocities and plume volumes. Reduced amplitudes are used instead of trace energies in this comparison because they are a more accurate measure of the strength of the initial explosive pulse. Also, acoustic reduced pressures are less affected by wind noise than the radiated acoustic energy estimations.   From the video observations, higher amplitude infrasound is associated with more impulsive gas release. However, there is no correlation between seismic signal strength and ejection velocities determined through the video records (see figure 2.15b and selected explosions in figure

2.14b,d). Because seismic amplitudes at Karymsky appear unrelated to both acoustic and video observations they probably reflect internal processes within the conduit.
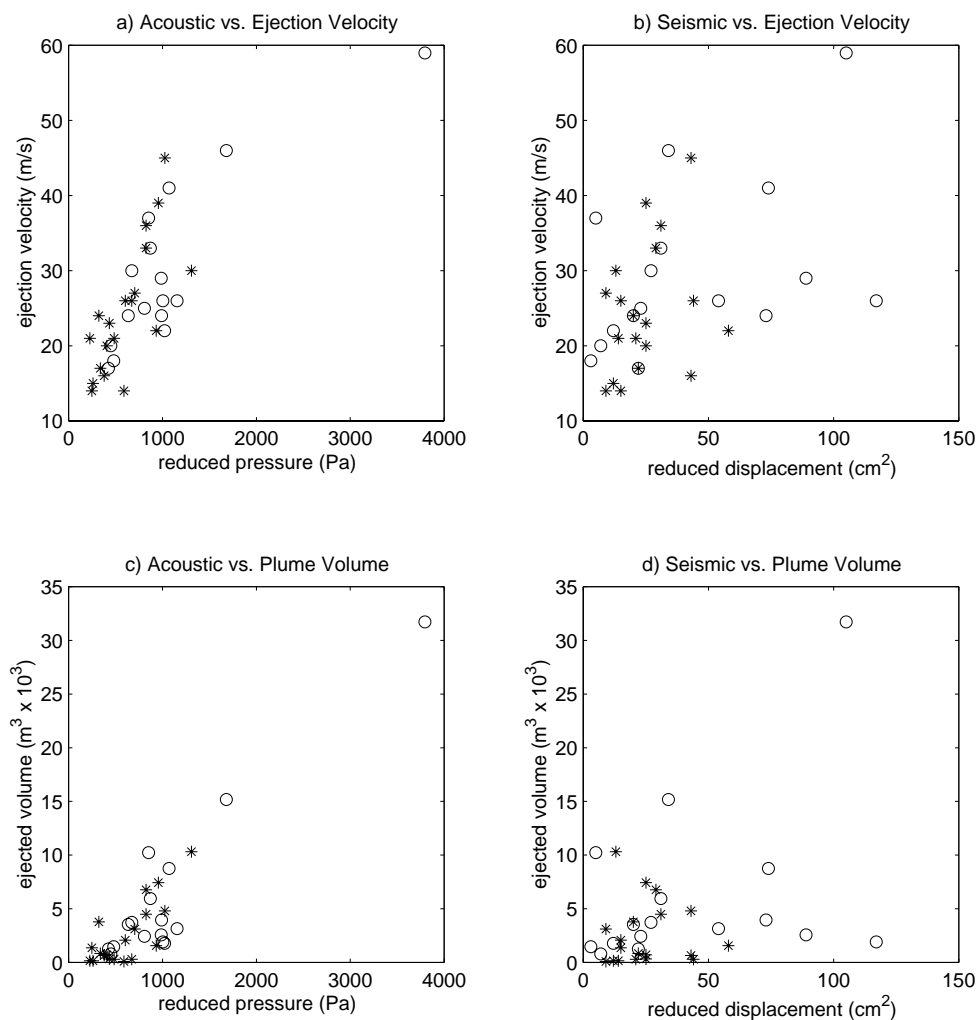

Figure 2.15 Reduced Amplitudes vs. Ejection Velocity and Plume Volume - Comparisons of maximum plume ejection velocity during the first second of an explosion with: a) reduced acoustic pressures and b) reduced seismic displacements. Comparisons of plume volume after one second of eruption with: c) reduced acoustic pressures and d) reduced seismic displacements. Ejection velocities and plume volume values are calculated for digitized images with pixel grayscale values greater than 30 out of 255. Events denoted by circles (o) correspond to explosions with brightness indices that exceed 50% (meaning that more than half the incandescent pixels have a grayscale level higher than 60). The darker, ash-laden events are denoted by stars (*). Only explosions with plume ejection velocities in excess of 5 m/s are displayed in this figure.

2.7 Erebus Explosive Gas Flux and Bubble Size

Video records from Karymsky in 1999 demonstrate a positive relationship between infrasound amplitude and gas ejection velocity leading to the conclusion that an energetic explosion is able to perturb the atmosphere more significantly. For a hemispherical explosion source, the acoustic pressure trace is proportional to the rate of change in the gas mass outflow (see chapter 1). Thus an impulsive explosion (high gas acceleration) is able to generate a much higher amplitude infrasonic pulse than a steady-state flow of gas. For both Karymsky and Erebus explosions, the onset of most acoustic explosion signals is characterized by a high-amplitude compressional impulsive phase. This initial pulse contains information about gas mass flux during the first moments of an explosion. By integrating an infrasonic pressure trace twice with respect to time, cumulative mass flux values (equation 1.9) can be theoretically determined for the onset of an explosion (see figure 2.16):

$$M(t) = \int_0^\tau 2\pi r \left[\int_0^\tau \Delta P(t + r/c)dt \right] d\tau \qquad (2.11)$$

$M(t) = $ cumulative mass flux from source

It is important to note that cumulative mass flux determined in this manner from infrasonic pulses is susceptible to underestimation. By analyzing only the first acoustic pulse, both extended degassing signals and low-frequency infrasound are neglected. Gas emissions for the first fraction of a second may be accurate, but the total gas released during an extended-duration degassing event is greater. Furthermore, equation 2.11 is based upon a linear theory of sound generation and may be inappropriate for large explosion sources with high overpressure or ejection velocities [Lighthill, 1978].

Explosions at Erebus are reasonably well suited for accurate gas flux estimations from infrasonic records because the typical explosion source is a bubble burst from the surface of the lava lake [Dibble et al, 1994]. This type of explosion is able to liberate a large
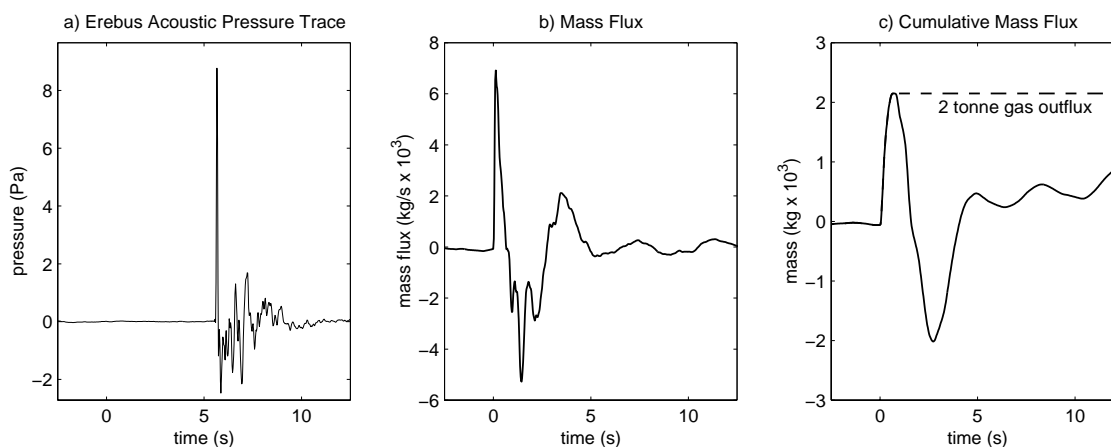
Figure 2.16 Infrasonic Pulse and Associated Mass Flux - a) Acoustic pressure trace associated with an explosion at Erebus (1999:359:06:52), recorded at EHUT (1900) meters from the vent. The example is selected because it is a low-noise, simple explosion. b) Corresponding mass flux time history and c) cumulative gas mass flux. Dashed line represents maximum mass outflux. Negative mass fluxes are probably artificial, low-frequency artifacts or alternatively, inertial effects [Kinney & Graham, 1985]. Figure is identical to figure 1.4 in chapter 1.

quantity of gas in a short amount of time, producing a very impulsive (relatively high-frequency) mass flux and an associated strong infrasonic pulse. Integrating infrasonic pressure traces twice for a suite of eruptions from Erebus in 1999-2000 provides gas mass flux values ranging from 1 to 6 tonnes, with a mean mass flux of 2.5 tonnes (see figure 2.17).

The explosive gas flux values determined from infrasonic pulses correspond to only a fraction of the total daily gas budget that passes from the Erebus vent. Average Erebus daily gas flux determined by Total Ozone Mapping Spectrometer (TOMS) is greater than $\sim 10^3$ tonnes of gas [Andres & Kasgnoc, 1998], an amount which is considerably greater than the summed emissions from individual bubble ruptures (2 to 5 explosions per day implies $\sim 10^1$ tonnes of gas per day). Significant degassing thus occurs at Erebus in the absence of large explosions. This conclusion is supported by observations of continuous non-explosive steam emissions and small bubbles (radius less than 1 meter) which
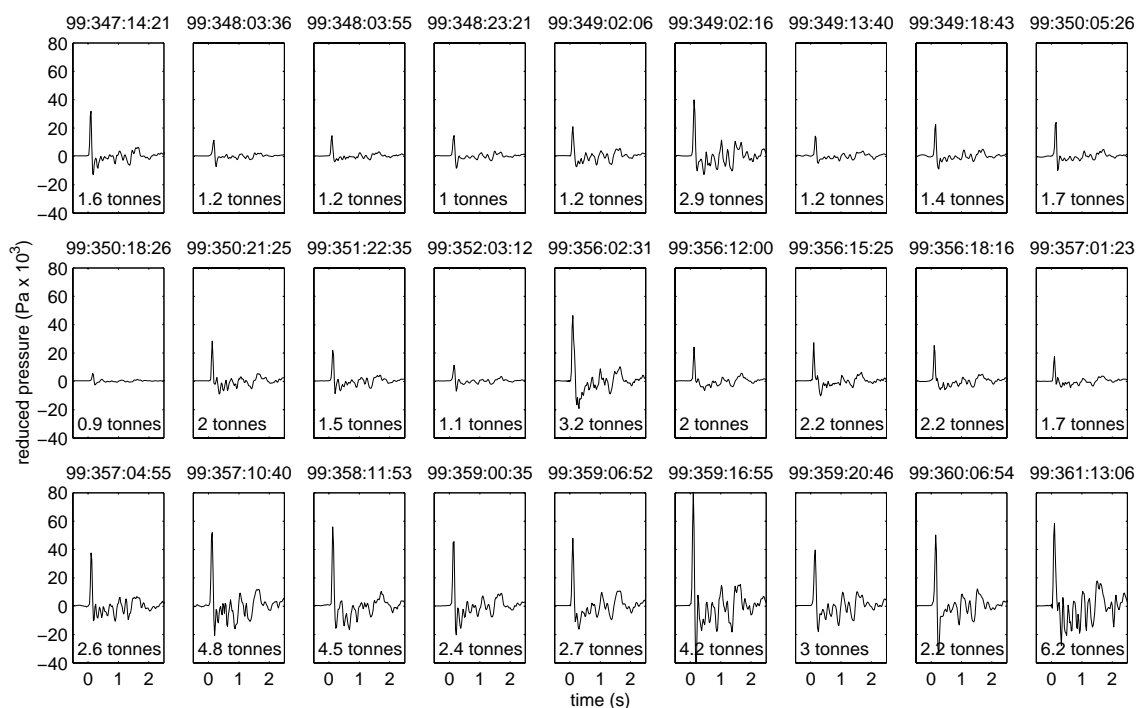
Figure 2.17 Mass Flux from Erebus Infrasonic Pulses - Acoustic pressure traces reduced to 1 meter for 27 Erebus explosions recorded at EHUT. Gas flux values correspond to maximum outflux during the first second of each explosion. Average gas mass outflux from the initial impulse for Erebus explosions recorded in 1999-2000 is 2.5 tonnes.

frequently degas at the lava lake surface (see figure 2.18a). Daily gas release totaling 10^3 tonnes could be accomplished through passive degassing at a steady flux of about 10^1 kg/s. Though this gas flux is at least three orders of magnitude smaller than the flux from explosive bubble bursts, it is a much more significant contribution over the course of a day. Acoustic and seismic events thus appear to reflect impulsive explosion sources, not the bulk gas flux from the crater.

If infrasound-derived gas mass flux estimates are contained in a single spherical volume, gas bubble radii can be estimated using assumptions about the bubble pressure prior to rupture. Gas bubble pressure is the sum of hydrostatic load, atmospheric pressure, excess residual (viscous) pressure, and surface tension [Tomaru, 1995]:

a)   b)
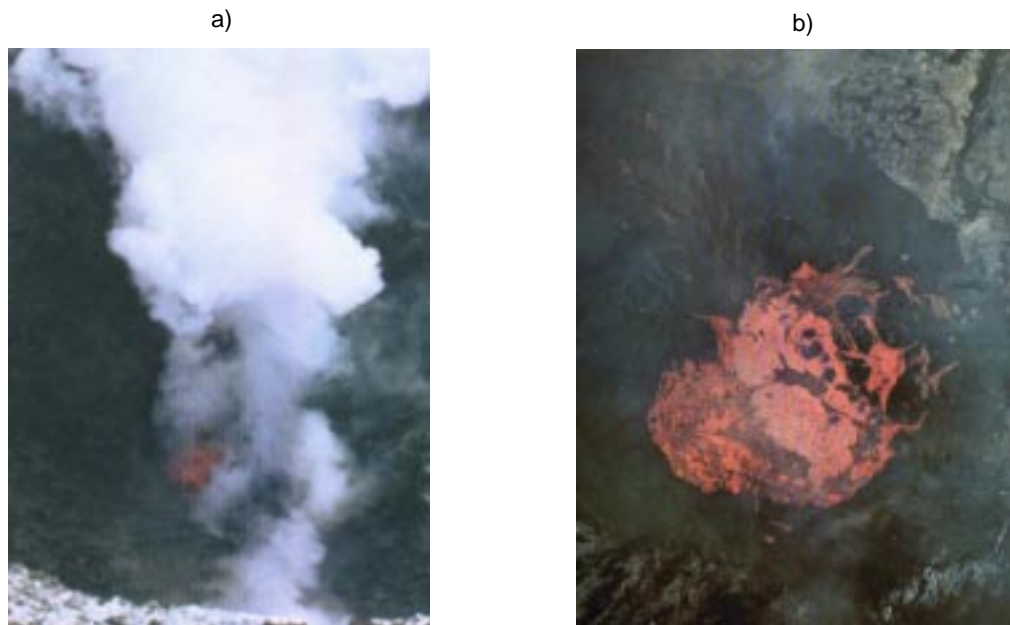
Figure 2.18 Photos of Erebus Degassing - a) Photo of passive degassing from the surface of the Erebus lava lake in 1985. Vertical field of few is about 100 meters. b) Photo of gas bubble burst from the surface of the Erebus lava lake in 1974. Dimension of bubble is approximately 50 meters. Both photos courtesy of P. Kyle.

$$\overline{P}_g = \rho_m g r_b + P_o + P_{res} + 2\sigma / r_b \qquad (2.12)$$

ρ_m = magma density (2700 kg/m^3)

g = gravity (10 m/s^2)

r_b = bubble radius (m)

P_o = atmospheric pressure (~10^5 Pa)

P_{res} = excess residual pressure

σ = surface tension - 0.4 Pa·m for basalt [Walker & Mullins, 1981]

Even for very small bubbles (with radius less than 0.001 meters), the surface tension term is a small contribution to the total gas pressure within the bubble, so gas pressure can be approximated as the sum of hydrostatic and viscous pressures. Bubble pressure can be inserted into the ideal gas law to estimate bubble size by using a spherical volume of $4/3\pi r^3$ with the top of the bubble resting at the free surface (see cartoon in figure 2.19):

$$\frac{4\pi}{3}r_b^3(\rho_m g r_b + P_o + P_{res}) = \frac{M}{m}RT \qquad (2.13)$$

M = mass of gas (kg)

m = molecular weight of gas (0.018 kg/mole for water vapor)

R = gas constant (8.314 N.m/mol.kelvin)

T = gas temperature (~1000 C)

Figure 2.19 displays the relationship between bubble size and gas mass for residual pressures ranging from 0 to 10 bars. Residual pressure refers to excess pressure that has accumulated in the bubble due to viscous or diffusive processes. Bubbles that are equilibrated to their depth will be hydrostatically pressurized, but bubbles that are actively diffusing or rising rapidly through the conduit may have an excess pressure. For Erebus gas bubbles with zero residual (viscous) pressure, the average 1999-2000 bubble radii are estimated to be 9 meters. This dimension is an overestimation if the bubbles possess excess pressure above overburden (see section 2.9) and/or the bubbles are vertically elongated slugs constrained by conduit walls [Clift et al., 1978]. Though a ~10-meter bubble radius is quite a bit larger than bubbles typically observed at open-vent basaltic volcanoes [Sparks, 1997], there is ample visual confirmation for the existence of bubbles of this size bursting from the Erebus lava lake [Phil Kyle, personal communication, 2000] (see figure 2.18b).

2.8 Karymsky Explosive Gas Flux and Bubble Foam Dimension

Though Karymsky explosions are often extended-duration degassing events lasting as long as several minutes, infrasonic pressure pulses may be integrated to recover gas flux values for the very onset of explosive degassing. In this manner, minimum gas flux values can be obtained for explosive events. Analysis of the first compressional pulse from a suite of 1998 Karymsky explosions provides mass flux values ranging from 0.5 to 2 tonnes, with an average flux of 1 tonne (see figure 2.20). Over the course of a typical day at Karymsky in 1998, 200 to 400 explosions were recorded, implying a total daily
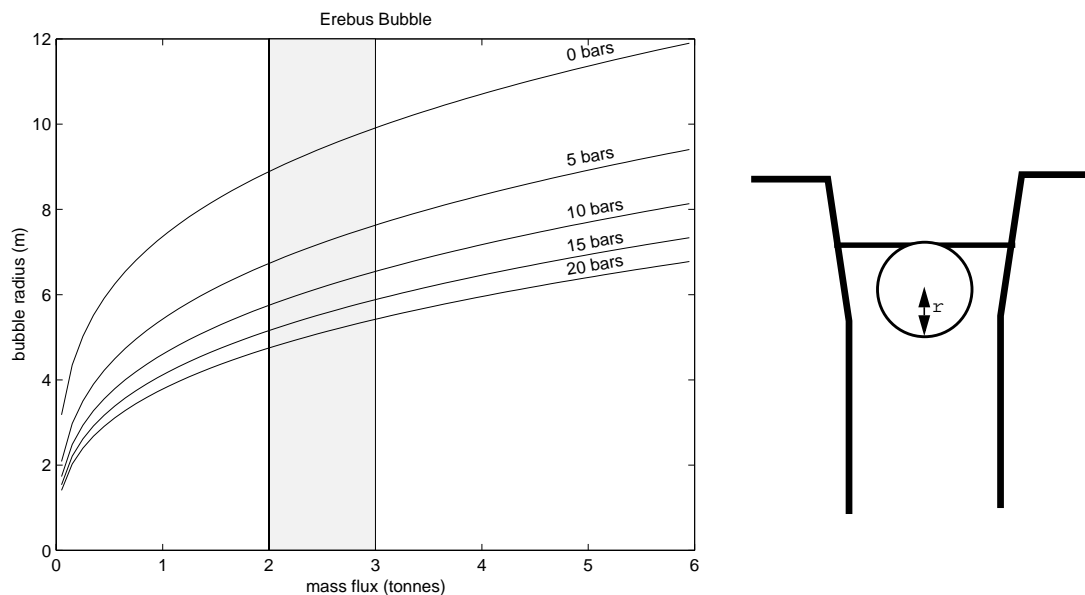
Figure 2.19 Erebus Bubble Radii - Bubble radii plotted as a function of bubble gas mass for gas bubbles (water vapor) immersed in a magma (density 2700 kg/m^3) with variable excess pressures (0, 5, 10, 15, and 20 bars). Shaded region corresponds to typical Erebus gas bubble masses. Cartoon shows bubble position with bubble top aligned with the lava lake surface.

gas flux of at least 200 to 400 tonnes. These values are certainly underestimations of the total gas flux from Karymsky because they only consider contributions from the event onset and many Karymsky events possess lengthy codas indicative of extended-duration degassing. Furthermore, as demonstrated at Erebus, significant degassing probably occurs without associated infrasound.

At Karymksy, gas mass flux estimates determined from infrasound can be corroborated with the COSPEC studies that were conducted in 1998. COSPEC remotely detects SO_2 emissions by measuring the amount of solar ultraviolet light absorbed in the eruption plume. Because the ratio of SO_2 emissions to total gas emissions remains constant at a single volcano (approximately 4 percent at Karymsky [Taran et al., 1991]), COSPEC measurements can be used to determine the total amount of gas flux through the vent. At Karymsky in 1998, all COSPEC scans, data reduction, and analysis were performed by Phil Kyle and Richard Law, researchers from New Mexico Technical University.
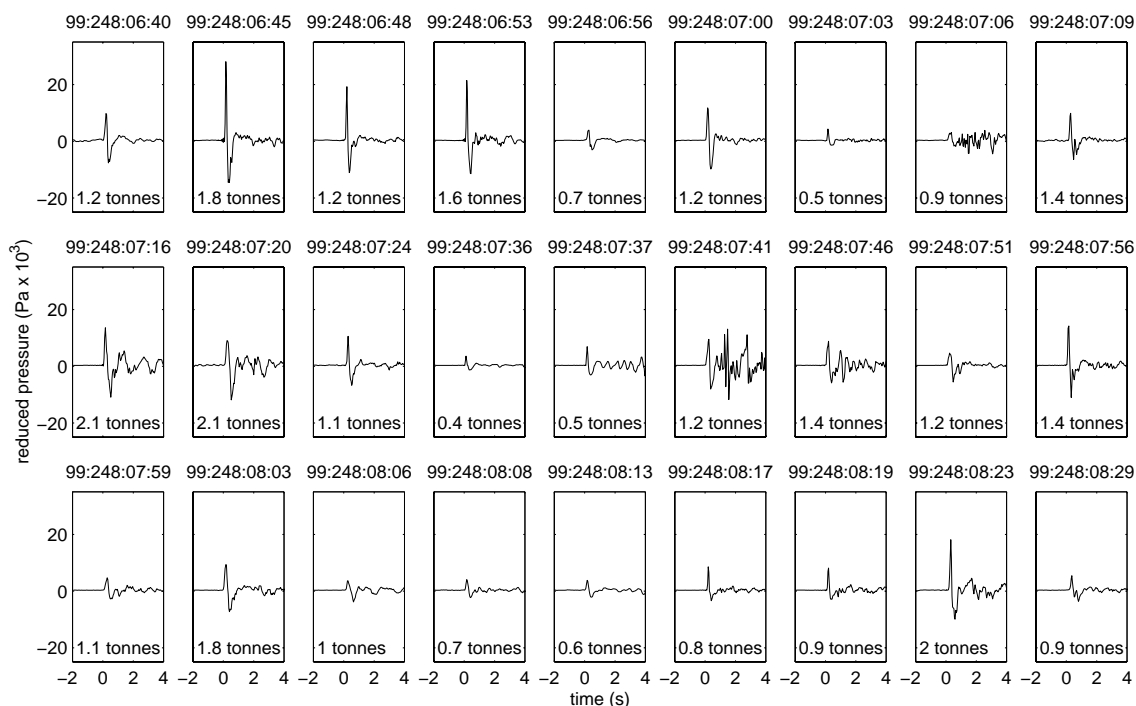
Figure 2.20 Mass Flux from Karymsky Infrasonic Pulses - Acoustic pressure traces reduced to 1 meter for 27 Karymsky 1998 explosions recorded at Kry1. Gas flux values correspond to maximum outflux during the first second of each explosion. Average gas flux from the initial impulse for Erebus explosions recorded in 1999-2000 is 1 tonne.

Repeated COSPEC scans at Karymsky were made of a section of the plume several hundred meters from the vent beginning with the first visible appearance of a plume. Because of the distance between the vent and scan transects, time resolution of Karymsky gas flux (from COSPEC measurements) is poorly constrained. Though video, acoustic, and seismic datastreams are able to document source processes occurring over time intervals of a fraction of a second, COSPEC gas flux measurements are filtered by the vagaries of atmospheric transport and suffer from low sample rates (scans of the Karymsky plume could be made only once or twice each minute). For this reason COSPEC gas flux values are smeared out over time and don't reflect impulsive gas emissions (see figure 2.21). Nevertheless, COSPEC studies in 1998 revealed fluctuations in gas emissions corresponding to discrete explosive events. These measurements are used to determine both background gas flux and gas flux associated with discrete

explosions. According to Law & Kyle (1999), background gas flux (defined by the absence of visible gas emissions) lies between 5 and 60 kg/s. Total daily gas flux is about 2000 tonnes per day [Law, 2000]. And flux per explosion ranges between 2 and 12 tonnes, with a mean value of 5.5 tonnes [Law & Kyle, 1999]. Daily gas flux from Karymsky determined through COSPEC is compatible with the values determined by TOMS (~10^3 tonnes) [Andres & Kasgoc, 1998].
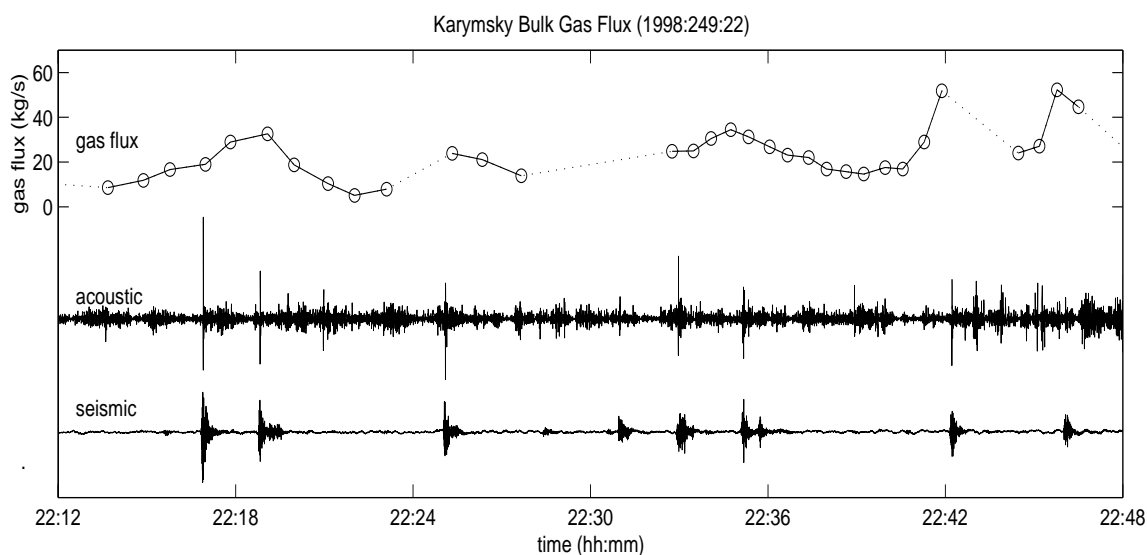

Figure 2.21 Karymsky Gas Flux Time Series - Total gas flux values (determined from COSPEC) plotted together with raw acoustic pressure traces and raw seismic velocity traces for 36 minutes of Karymsky degassing activity in 1998. Circles are individual scan measurements. Gaps between measurements (dotted lines) indicate periods of time where scans were not made. At the scale of the plot, many of the infrasonic signals associated with explosions are obscured by wind noise.

Average Karymsky explosive gas flux determined from infrasound records of the initial pressure pulse is 1.0 tonnes, corresponding to about 20% of the total explosion gas flux determined through COSPEC studies [Law & Kyle, 1999]. If one tonne of gas is released as a single impulsive bubble rupture at the surface of an open conduit, the corresponding spherical bubble (with zero residual pressure) would have a 7 meter radius. However bubbles of this dimension are improbable for explosions at Karymsky, because magma viscosity and yield strength are higher than at Erebus, effectively

preventing the formation of very large vesicles [Sparks, 1997]. Furthermore, the conduit radius at Karymsky may be narrower than 7 meters [Wada, 1994], requiring a vertically-elongated gas volume. It is likely that the andesitic Strombolian explosions at Karymsky represent bubble foam fragmentation sources [Sparks, 1997]. Small bubbles accumulate in foams with void fractions that increase with decompression and diffusion. Once a critical void fraction is reached (67-80% in most cases [Sparks, 1978]), bubble disruption occurs and the fragmentation front migrates rapidly downward into the magma conduit. For a critical bubble foam occupying a conduit with zero excess pressure relative to overburden, the gas volume depends upon conduit width and the overlying material load:

$$\overline{P}_g \ = \ \rho_m g(h + l/2) + P_o + P_{res} + 2\sigma/r_b \tag{2.14}$$

$h \ = \ $ vertical extent of cap rock (m)

$l \ = \ $ length of bubble foam

For foams of bubbles located beneath a cap rock of height (h), residual pressure and surface tension forces are small compared to the overburden. Putting the hydrostatic pressure contributions into the ideal gas law for a cylindrical volume gives:

$$V_f A l(\rho_m g l/2 + \rho_m g h + P_o) \ = \ \frac{M}{m}RT \tag{2.15}$$

$V_f \ = \ $ void fraction of gas (75%)

$A \ = \ $ conduit cross-section (m^2)

According to equation 2.15, the vertical extent of the bubble foam is only dependent upon cross-sectional area and the overlying load of gas-depleted material. Both the cap rock thickness (lithostatic load) and cross-sectional conduit area are very uncertain quantities for the andesitic Strombolian-type activity at Karymsky. Observations from overflights of the vent indicate a rubble-choked orifice which may be several meters wide. However, both the depth to the fragmentation front and conduit width at depth are still the subject of speculation. Figure 2.22 demonstrates the relationship between the bubble foam dimension and gas mass for a variety of different conduit parameters.
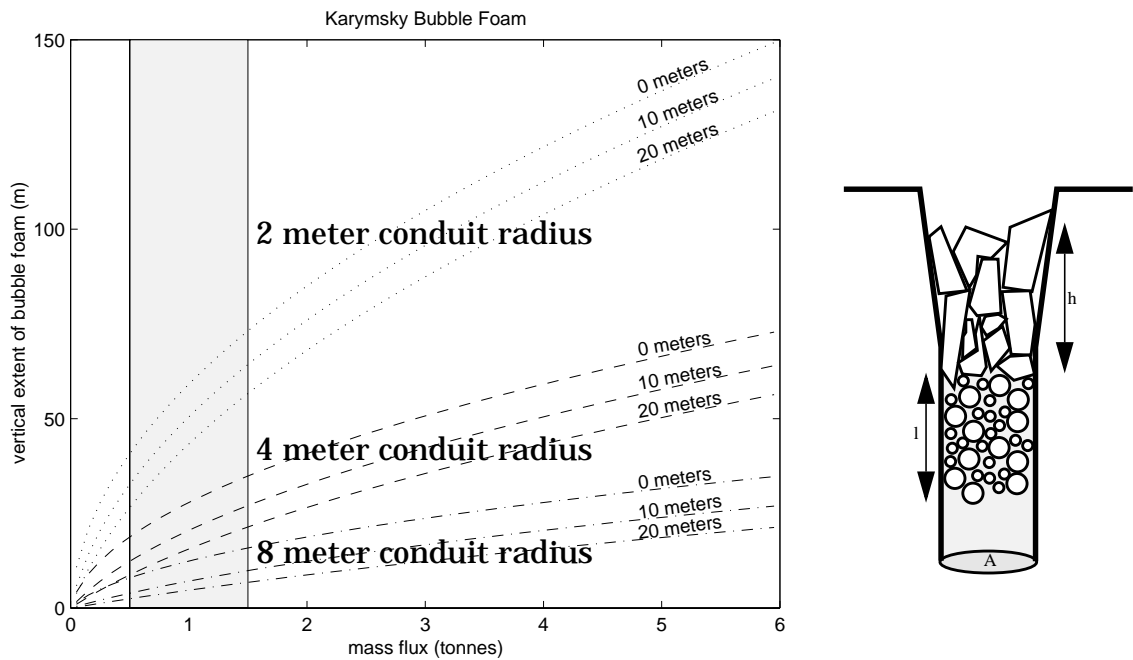
Figure 2.22 Karymsky Bubble Foam Dimensions - Vertical extent of bubble foam (l) plotted as a function of bubble gas mass for bubbles immersed in a magma with variable lithostatic load (h) and variable conduit radii (2 meters - dotted line, 4 meters - dash-dot line, 8 meters - dashed line). Shaded region corresponds to typical gas mass flux values inferred from the initial infrasonic impulse of a Karymsky explosion. Cartoon shows the geometry of the bubble foam beneath a plug of rubble.

2.9 Potential Energy of Expanding Volatiles

If the initial pressurization of magmatic volatiles is known, the total potential energy release due to the expansion of gas can be evaluated according to thermodynamic principles. For adiabatic, isentropic explosions expanding into the atmosphere [Kinney & Graham, 1985]:

$$E_{Explosion} = \frac{M}{m}\frac{RT_i}{\gamma - 1}\left[1 - \left(\frac{P_o}{P_i}\right)^{\frac{\gamma - 1}{\gamma}}\right] \approx 5 \times 10^6 M\left[1 - \left(\frac{P_o}{P_i}\right)^{0.1}\right] \qquad (2.16)$$

T_i = initial temperature (1000-1500 K for most magmas)

P_i = initial pressure

γ = heat capacity ratio (1.1 for hot gases [Garces et al., 1998a])

The righthand equality in equation 2.16 is determined assuming a magma temperature of 1000 degrees Celsius, a molecular weight of volatiles equal to 18 g/mole (predominance of water vapor), and a heat capacity ratio of 1.1 for hot gases [Garces et al., 1998a]. The relationship between volatile overpressure (a function of depth) and potential energy per tonne of compressed gas is illustrated in figure 2.23. Gas overpressure in a bubble or bubble foam is defined as the difference between the initial and expanded pressures ($P_i - P_o$). For Strombolian explosions, bubble overpressure is most dependent upon overburden pressure. Bubble overpressure at the time of rupture is probably greater at Erebus than at Karymsky because the fragmentation depth is shallower (Erebus bubbles are observed bursting at the very surface of the lava lake).
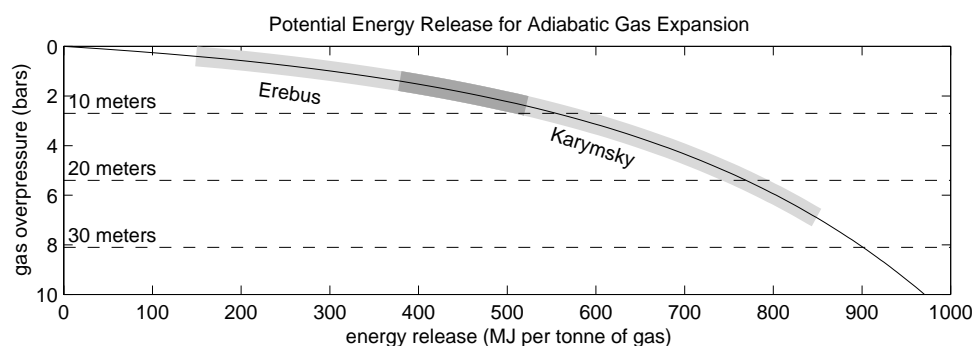
Figure 2.23 Potential Energy for Gas Expansion at Erebus and Karymsky - Potential energy released during adiabatic expansion of pressurized water vapor from an initial temperature of 1000 degrees C according to equation 2.16. Equivalent hydrostatic load pressures at 10, 20, and 30 meters are plotted assuming a fluid magma bulk density of 2700 kg/m³. Pressures and energies corresponding to possible fragmentation regimes are outlined for the Erebus and Karymsky magmas.

Excess pressure relative to the surrounding magma is generally a small contribution that is a balance of diffusive bubble growth and viscous and interfacial (surface tension) forces. In the volatile-depleted uppermost section of the conduit, diffusion may be negligible and surface tension will be small. Excess bubble pressure is then determined by viscous resistance to bubble expansion as the rising bubble is depressurized [Tomaru, 1995]:

$$P_g - P_m = \frac{4\eta}{r}\frac{dr_b}{dt} \tag{2.17}$$

P_g = pressure of gas

P_m = pressure of magma

η = fluid viscosity (Pa•s)

The pressure in a fluid magma at the depth of the bubble center is equal to the overburden:

$$P_m = \rho_m gh \tag{2.18}$$

ρ_m = magma density (2700 kg/m^3 [Dibble, 1994])

g = gravity (10m/s^2)

h = height of overlying magma

And the pressure in the gas bubble can be calculated according to the ideal gas law:

$$P_g = \frac{M}{m}\frac{RT}{(4/3)\pi r_b^3} \tag{2.19}$$

As bubbles ascend toward the surface and the overburden decreases, bubble radius increases to compensate for the pressure differential. If bubble rise velocities are fast enough, an excess pressure can accumulate in the bubble due to viscous resistance of the fluid. The Stokes rise velocity for a spherical bubble in a Newtonian fluid is [Clift et al., 1978]:

$$U_T = \frac{2gr_b^2(\rho_m - \rho_g)}{9\eta} \tag{2.20}$$

U_T = terminal velocity (m/s)

ρ_g = density of gas (usually $\rho_m - \rho_g \approx \rho_m$)

For an isolated bubble with a radius of ten meters rising in a relatively low viscosity phonolitic lava lake (viscosity $\sim 10^4$ Pa·s [Dibble et al., 1984]), terminal rise velocities may exceed 10 m/s. In andesitic systems, bubble rise velocities should be much slower because bubble dimensions are smaller and viscosity is greater (at least 10^5 Pa·s [Sparks,

1998]). Under these conditions, centimeter-sized vesicles, commonly observed in Karymsky bombs and lava flows, might ascend at a rate of about 1 mm/hour, seven orders of magnitude slower than the rise rate for large bubbles in basaltic or phonolitic magmas. This rise velocity is much too slow to be the primary mechanism for Karymsky gas escape where explosions occur about ten times each hour. The high explosion frequency and high melt viscosity at Karymsky hints that there is an associated magmatic flux from the conduit, a theory that is supported by the observations of an active block lava flow issuing from the Karymsky vent. If gas flux is accompanied by a corresponding flux of exsolved magma, rise rates may be roughly estimated. Using an initial 2% by weight volatile concentration and a typical 5.5 tonne gas flux per explosion (determined from COSPEC), the average amount of extruded, dense (2700 kg/m^3) degassed magma should be ~10^2 m^3 per explosion. If this volume is extruded from a four-meter radius conduit ten times each hour, the rise rate is approximately 0.005 m/s.

If the rise velocity (depressurization rate) is known, bubble growth in the absence of diffusion can be roughly modeled according to equations 2.17-2.20. Figure 2.24 illustrates bubble expansion and overpressure in the uppermost 40 meters of the conduit (where overburden drops the most abruptly) under a range of conditions (a-b) large bubbles - low viscosity and c-d) small bubbles - higher viscosity). From figure 2.24b,d it is evident that the primary contribution to bubble overpressure is overburden. For the calculated fluid rise rates at Karymsky (0.005 m/s), excess viscous pressure is negligible. Excess viscous pressures are similar in magnitude to overburden only for rapidly ascending bubbles approaching the Erebus lava lake surface (at depths shallower than the typical Erebus bubble radius).

The potential energy released during explosive degassing at Erebus and Karymsky can be estimated according to equation 2.16 for estimated bubble overpressures. For an average 2.5 tonne gas bubble at Erebus, the calculated depth of the bubble center prior to rupture is 5 to 10 meters, and the corresponding explosive yield may be 500 to 1000 MJ (refer to
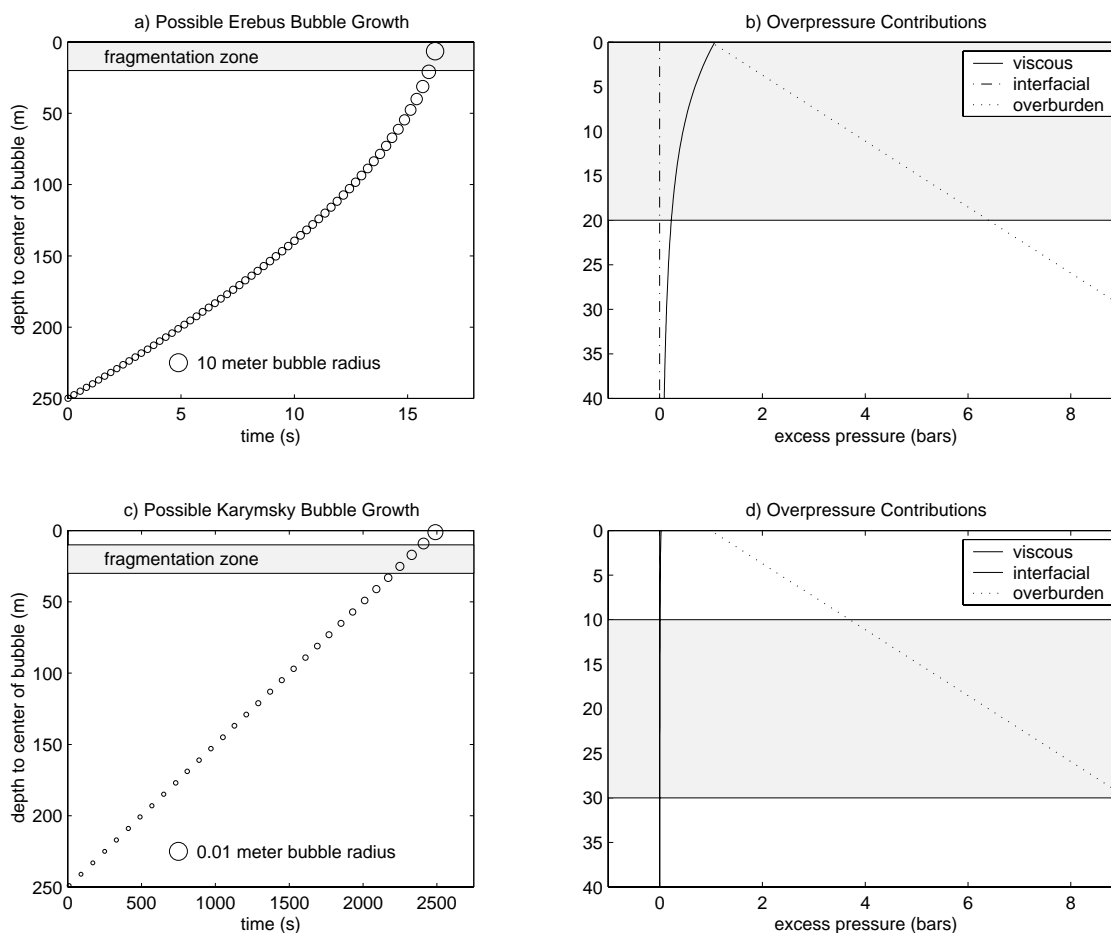
Figure 2.24 Bubble Expansion History at Erebus and Karymsky - a) Large bubbles at Erebus ascend through the magma conduit, accelerating as they expand (bubbles drafted at true relative size). The modeled bubble (mass 2500 kg and initial radius ~4 m) begins with zero excess pressure at a depth of 250 meters. b) Excess pressure contributions within the fragmentation zone for the rising Erebus bubble. Overburden assumes a magma fluid density of 2700 kg/m^3. c) Small bubbles at Karymsky ascend at constant velocity along with magma in a two-phase flow. The modeled bubble (mass 10^{-7} kg and initial radius ~10^{-3} m) begins with zero overpressure at a depth of 250 meters. d) Excess bubble pressure contributions for the Karymsky bubble are dependent only on overburden.

figure 2.23). For an average 1 tonne explosion at Karymsky with a 10 to 30 meter depth at the center of the foam, the explosive yield is a similar magnitude. It is important to note however, that these potential energy yields are estimations for the initial explosive onset at Erebus and Karymsky only. Extended degassing events at Karymsky are

certainly more energetic because more gas is decompressed. Energy yields of ~10^9 Joules may be appropriate minimum bounds for large Strombolian explosions.

2.10 Energy Budget for Eruptions:

Potential energy released during the expansion of magmatic gases is the fundamental source of the seismic and acoustic energy generated during Strombolian-type degassing. The following sections focus on the energy transferal that results from bursting of bubble(s) during discrete Strombolian events. Some energy is certainly dissipated prior to the explosion during viscous two-phase flow in the conduit [Vergniolle et al., 1996], but this process is not analyzed here because it is not readily observed in the acoustic and seismic records from Erebus and Karymsky.

During a Strombolian explosion, the rapid expansion of magmatic gases from the vent involves transferal of energy to a variety of modes including: (1) thermal, (2) chemical, (3) kinetic, (4) deformational (viscous), and (5) elastic. The largest portion of the energy budget is the thermal energy released during the ejection and cooling of magma and gas (refer to chapter 1). However, conversion of thermal energy to elastic energy and/or kinetic energy is ignored in this chapter because the explosive expansion of pressurized gases is nearly adiabatic [Kinney & Graham, 1985] and heat conduction to the ground and atmosphere is probably not rapid enough to generate elastic waves. Potential entropic energy release is also ignored in this discussion because the primary volatiles liberated during volcanic explosions (H_2O - 87%, CO_2 - 6.5%, SO_2 - 4.3%, HCl - 1.7% [Taran et al., 1991]) are too stable to recombine chemically. As a result, only elastic, kinetic, and viscous dissipation are left for consideration here.

$$E_{Explosion} = E_{Elastic} + E_{Conduit} + E_{Kinetic} \qquad (2.21)$$

In the next three sections, the energy budget will be discussed for the very onset of the Strombolian explosions at Erebus and Karymsky. As discussed previously, Karymsky

explosions are often complicated degassing events with fluctuations in material emissions lasting tens of seconds to several minutes. The relatively simple onsets of these explosions appear to be the most energetic portion of the explosion, with the most vigorous exodus of gas and material and the highest amplitude acoustic signals. Infrasonic signals from the explosion onset can be interpreted in terms of mass emissions so that potential energy values may be compared with radiated elastic and kinetic energy.

2.10.1 Elastic Energy

Acoustic and seismic energies are the simplest components of the energy budget to recover because they can be measured directly from acoustic and seismic pressure traces. Radiated elastic energy may be estimated according to equations 2.3 and 2.7 with the assumption that acoustic and seismic wavefields are reasonably well represented in the frequencies of interest by the sensors and data acquisition systems. This is an appropriate assumption for acoustic energy above the Nyquist frequency (20 Hz for Erebus, 62.5 Hz for Karymsky) because the fundamental explosion source does not produce significant acoustic energy in the audible band (refer to chapter 1). For seismic energy, sample rates are also appropriate because corner frequencies for explosion earthquakes are observed to be well below the Nyquist frequency. Broadband seismic instrumentation at Erebus and Karymsky also provides a suitable response at lower frequencies as evidenced by the observation of low-amplitude, ultra low-frequency events at Erebus [Rowe et al., 2000]. Similarly, broad-band acoustic data (from pressure transducers with frequency responses down to DC) at various different Strombolian-type volcanoes (Erebus [Rowe et al., 2000], Arenal [Hagerty et al., 2000], and Stromboli [Vergniolle et al., 1996]) indicates that the bulk of the infrasonic energy is above 1 Hz and is thus adequately recorded by the electret condenser microphones deployed at Karymsky and Erebus (see appendix B for more information on microphone specifications).

Elastic energy attenuation losses, scattering, focusing, anisotropic radiation, and site responses are effects which can be understood with foresight. Generally they are not

significant contributions to seismo-acoustic energy estimates for microphones and seismometers deployed at intermediate distances (several kilometers) from the explosion source (see chapter 1). As a rule, the acoustic and seismic energy budgets can be much better quantified than the energy sinks associated with kinetic energy and viscous dissipation in the conduit or lava lake.

2.10.2 Kinetic Energy

The kinetic energy released during volcanic explosions can be roughly estimated from video footage [Ripepe et al., 1993] or by analysis of the distribution of ballistics [Wilson, 1980; Fagents & Wilson, 1993]. However, both methods provide values that may have considerable error. For many explosions, the maximum gas or ballistic ejection velocities can be reasonably well determined, but the integrated mass flux is much more difficult to quantify. Video records from Karymsky in 1999 provide records of ejection velocities because they reveal how plume volume increases with time. Since infrasonic records constrain gas mass outflux for the onset of the explosive events, kinetic energy can be determined if assumptions are made about the ratio of ejected gas to solid particles.

For a suite of simple impulse events from the 1999 Karymsky record, kinetic energy can be estimated for known ejection velocities (determined from video) and gas mass fluxes (determined from acoustic pressure traces). Figure 2.25 shows examples of a series of explosions together with inferred gas flux, ejection velocities, kinetic energy (associated only with the gas flux), and acoustic trace energy. The kinetic energy estimates are calculated assuming a uniform escape velocity for the entire mass of pure gas, neglecting kinetic energy contribution from bombs or particles contained in the ash-laden plumes. For the gas phase only, Karymsky explosion onsets appear to have kinetic energies of 10^5 to 10^6 Joules which are comparable to the radiated acoustic energy inferred from the infrasonic pressure traces (according to equation 2.3). As an upper bounds on the total kinetic energy for an ash and ballistics-rich plume, it is possible to consider the fragmentation of a bubble foam that carries with it a corresponding volume of degassed

magma. Using a 2% volatile weight [Law, 2000], a one tonne gas release implies 50 tonnes of exsolved magma. Ejection velocities from the vent, however, are probably not uniform for gas and the associated degassed magma. At Karymsky, much of the solid flux escapes relatively effusively as part of block lava flows. Wilson (1980) estimates that the gas mass percentage for Strombolian ejections is as high as 5 to 30%. Therefore, it is improbable that the total kinetic energy exceeds the gas-related kinetic energy by more than about an order-of-magnitude at Karymsky.

At Erebus the kinetic energy associated with gas emissions may be a large percentage of the total kinetic energy released during the explosion because bubble skins are fairly thin and contain a relatively small amount of magma mass. At Stromboli, bubble surfaces are thought to be only a few centimeters thick [Ripepe & Gordeev, 1999; Vergniolle et al., 1996], implying a total bubble skin mass of about 10^3 kg for a 10 meter radius bubbles. Average Stromboli explosion kinetic energy calculated by McGetchin & Chouet (1979) is 4 x 10^5 J, corresponding to 240 kg of gas ejected at 60 m/s. Ripepe et al. (1993) also estimated kinetic energy for Stromboli explosions by summing kinetic energy contributions from individual bombs ($E_{Kinetic} = \frac{1}{2}\sum m_i v_i^2$) and found slightly larger kinetic energy values ranging from 5 x 10^5 J to 5 x 10^6 J for a suite of six explosions. The largest of these explosions had a mean ejection velocity of 16 m/s for 4.4 tonnes of solid material (excluding the gas phase).

Explosion sources may be very similar at both Erebus and Stromboli because large bubble ruptures occur at the very surface of an open, low-viscosity magma column [Vergniolle et al., 1996; Dibble, 1994]. At both volcanoes, bubble slugs can percolate up through the fluid and erupt at the surface without ejecting a proportionate amount of exsolved magma [Sparks, 1997; Dibble, 1994]. Though it is sensible to use Stromboli explosions as an analog for Erebus explosions, the kinetic energy release must be scaled up considerably for Erebus explosions because both mass flux and ejection velocities are
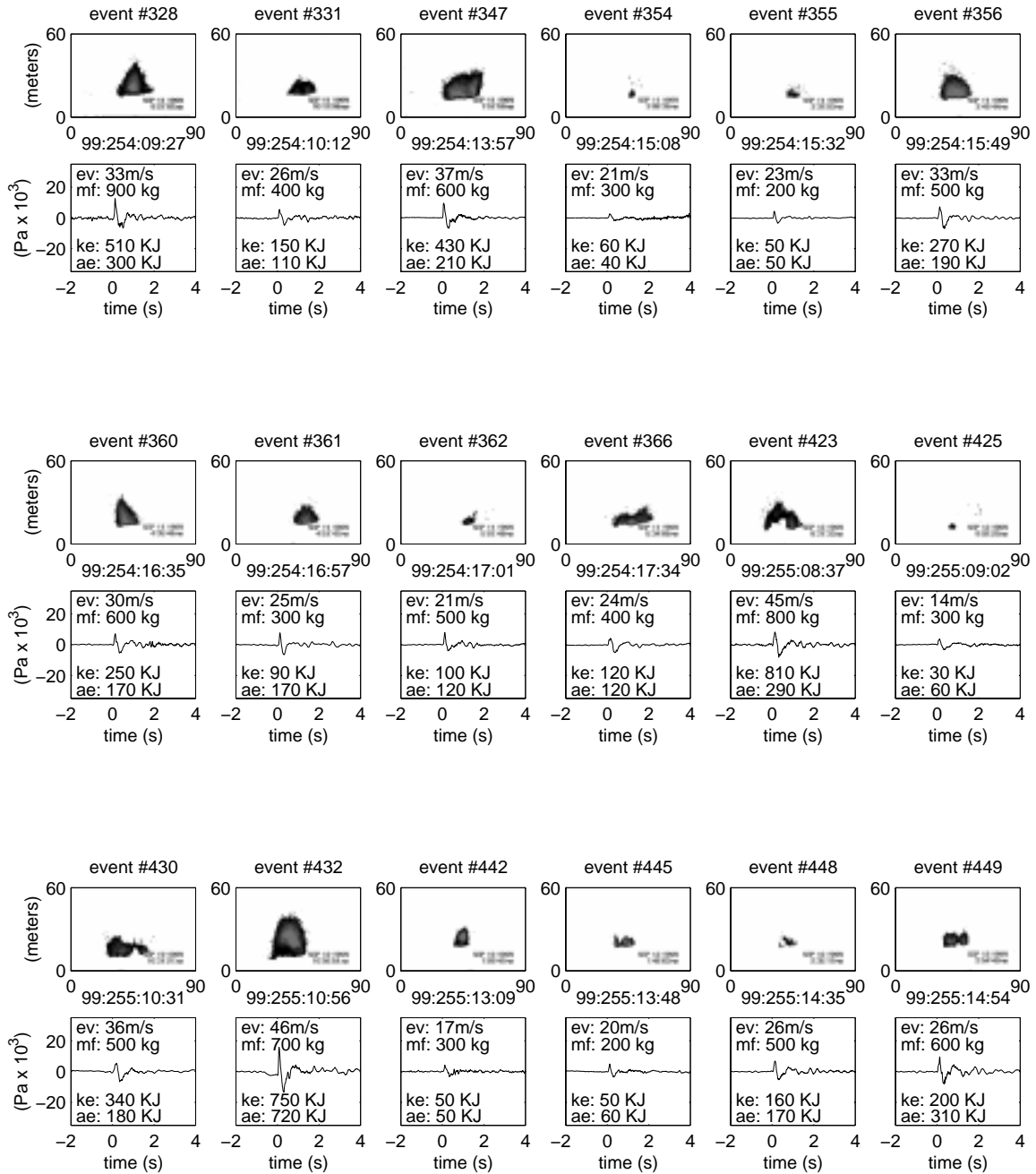
Figure 2.25 Kinetic Energy Estimates for Erebus Explosions - False color images of explosion plumes after 1.0 seconds (top panels) and associated acoustic waveforms (bottom panel) for 18 Karymksy 1999 explosions. The explosions are selected because they consist primarily of a single, low-noise acoustic pulse. Each event is provided with: ejection velocities (ev) determined from the first second of an explosion, mass flux (mf) determined according to equation 2.11, kinetic energy (ke) of the gas phase, and acoustic energy (ae) determined by equation 2.3.

greater than at Stromboli. The maximum ballistic ejection velocity of 70 m/s for the 5 x 10^5 J Stromboli explosion [Ripepe et al., 1993] is somewhat slower than the maximum ballistic ejection velocity estimated at Erebus. At Erebus, projectiles are frequently thrown outside the crater rim which is 200 meters above and 200 to 500 horizontal meters away from the vent [Bjorn Johns, personal communication, 2000]. From simple trajectory analysis [Wilson, 1980] these projectile distances imply muzzle velocities in excess of 100 m/s. For the gas phase only (average mass flux of 2.5 tonnes), these muzzle velocities imply kinetic energy values of ~10^7 Joules.

Kinetic energy is dissipated by frictional resistance (heat generation) in the atmosphere and by transferal of momentum to the atmosphere (acoustic) and ground (seismic). The contributions to the seismic energy budget from bombs impacting the ground is not readily evident in seismic traces, but the momentum transferal from expanding gas to compressional sound waves is the source of infrasound (see chapter 1). An efficient transferal of gas momentum to infrasound would imply that the kinetic energy from Strombolian explosions is transient and not dissipated by frictional heat loss. Infrasound is most efficiently produced by gas expansion rather than bomb or particle ejection because the associated volume displacement is much higher for gas. The kinetic energy of individual bombs may be high, but they tend to penetrate the overlying atmosphere and contribute little energy to infrasonic wave generation. The transfer efficiency of kinetic energy to infrasound should be dependent upon the size of ballistics and the ratio of gas phase to solid phase in an eruption plume.

2.10.3 Energy Dissipation in the Conduit

The seismic wave generation from a tectonic earthquake source is considered an inefficient process where the work done by frictional forces of sliding fault surfaces is dissipated by heat production and/or chemical or phase changes to the wall rock [Dobrovol'skiy, 1994]. In an explosion earthquake, the potential energy released during gas expansion also appears to be far greater than the radiated elastic (or kinetic) energy.

For explosion earthquakes, seismo-acoustic-kinetic inefficiency may reflect work spent on fluid ascent and gas escape (dissipation) in the conduit.

Viscous dissipation of energy (heat generation) in the conduit is non-recoverable work that requires consideration in the energy budget. In the absence of brittle failure of conduit rock, energy may be dissipated by viscous flow. During an explosion, overpressure at the fragmentation depth may be substantially larger than overpressure at the orifice owing to head loss within the conduit. Energy dissipated by viscous flow is directly proportional to pressure drop within the conduit. For a constant pressure gradient (dP/dl), conduit diameter, and average flow velocity, the energy decrease over a length of conduit is (see appendix A):

$$\Delta E = \frac{dP}{dl}\left(\frac{\pi L D^2}{4}\right)\overline{V}t \qquad (2.22)$$

L = conduit length (m)

D = conduit diameter (m)

$\overline{V}$ = average flow velocity (m/s)

t = elapsed time (s)

For isothermal turbulent gas flow, the pressure gradient is determined by [Fay, 1994]:

$$\frac{dP}{dl} = -\frac{f}{D}\left(\frac{\rho_f \overline{V}^2}{2}\right) \qquad (2.23)$$

ρ_f = fluid density

f = frictional factor

Where the frictional factor for flow in a cylindrical conduit with smooth walls is dependent upon Reynolds Number [Fay, 1994]:

$$f = 64/Re_D \qquad (2.24)$$

And the Reynolds Number is a dimensionless parameter defined by:

$$Re_D = \rho_f \overline{V} D/\eta \qquad (2.25)$$

η = viscosity (Pa·s)

Combining equations 2.19 and 2.20 gives the energy dissipation from head loss (pressure decrease) in a conduit:

$$E_{Conduit} = -\frac{\pi f}{8}\rho_f \overline{V}^3 LDt \qquad (2.26)$$

And the energy dissipation for flow in a cylindrical conduit with smooth walls is:

$$E_{Conduit} = -8\pi\eta \overline{V}^2 Lt \qquad (2.27)$$

Unfortunately, viscous flow losses are difficult to quantify because flow properties such as fluid viscosity, fluid density, and conduit length are unknown. The viscosity of ideal gases at 1000 degrees Celsius lies between 10^{-3} and 10^{-4} Pa·s [Fay, 1994]. However, turbulent gas flow with significant particle entrainment may serve to dramatically increase the effective viscosity. At Karymsky, it is certainly possible to imagine situations where viscous dissipation is significant given rapid flow (ejection) velocities, lengthy conduits, and high eddy viscosities. However, at Erebus the bulk of the gas does not escape through conduits or cracks, and viscous dissipation during bubble rupture should be minimal. The absence of viscous dissipation may explain why Erebus explosions are acoustically efficient relative to Karymsky.

2.11 Models for Variable Seismo-acoustic Energy Partitioning:

The relative partitioning of energy between acoustic and seismic wavefields is easily determined from seismic and infrasonic data and may provide insight into fundamental properties of a volcano including the geometry and geology of the volcanic plumbing system and the physical source motions of the explosion. Prior to the current study of seismo-acoustic energy partitioning at Karymsky, other researchers observed evidence for variable seismo-acoustic amplitude ratios and suggested several different models: Mori et al. (1989) analyzed a suite of explosions at Langila Volcano, measuring seismic displacements and the amplitudes of associated air phases (acoustic airwaves coupled to the ground). They noticed significant variability in seismo-acoustic relative amplitudes and offered an explanation of variable transferal of acoustic energy into the mechanical

energy required to blast material from the vent. Garces et al. (1998a) argued alternatively that variable seismo-acoustic ratios at Arenal Volcano can be explained by time-varying melt properties which dramatically affect impedance contrasts. Rowe et al. (2000) examined a suite of explosions at Erebus volcano and noticed a drop in seismic efficiency for the very smallest explosions (explosions much smaller than the Erebus explosions examined in the current dataset). They suggested that the smaller explosions are very superficial and are seismically isolated from the wall rock surrounding the conduit and/or lava lake. Finally, Thompson et al. (in press) analyzed acoustic waves associated with both Plinian and Strombolian eruptions at Shishaldin. They associated larger acoustic signals with the later stages of the eruption when both the vent and conduit were relatively open. Though these investigators do not explicitly consider changing atmospheric conditions that can affect recorded acoustic pressure amplitudes (see chapter 1), they are each convinced that the variable seismo-acoustic ratios at these volcanoes represent source-related phenomena and are not artifacts of propagation.

a) Wind (weather)

b) Kinetic Dissipation

c) Changing Magma Impedance

d) Dissipation in Conduit
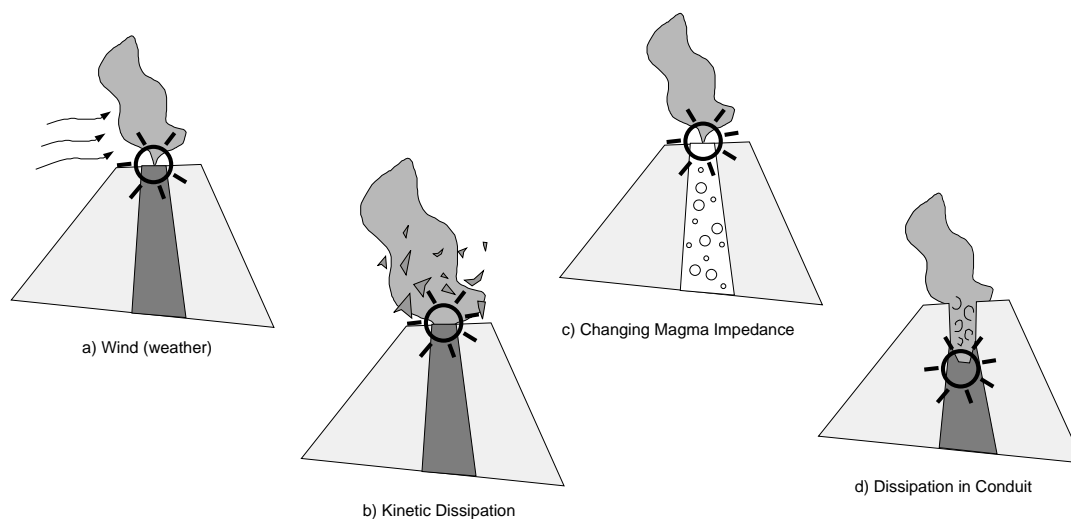
Figure 2.26 Mechanisms for Variable Seismo-acoustic Partitioning - Cartoon of possible mechanisms responsible for variable seismo-acoustic ratios within a suite of explosion earthquakes: a) effects of variable atmospheric conditions, b) transferal of acoustic energy to kinetic energy, c) variable magma impedance, d) viscous dissipation in the conduit.

In the Erebus dataset, energy partitioning into the seismic and acoustic wavefields is relatively uniform and slight variation in seismo-acoustic reduced amplitude ratios may

be attributed primarily to variable atmospheric structure. However, at Karymsky seismo-acoustic reduced amplitudes ratios have a great deal of scatter and should be attributed primarily to variations in source dynamics. The next sections detail source mechanisms that could be responsible for variable source energy partitioning at Karymsky.

2.11.1 Kinetic Energy Sink

Mori et al. (1989) propose that a finite explosion energy budget is distributed between acoustic energy and kinetic energy (figure 2.26b). They argue that intense emissions of ash and/or ballistics are accompanied by 'softer' explosions because energy is needed to propel the denser ejecta. This hypothesis is plausible because acoustic and kinetic energy release can be of the same order of magnitude for some Strombolian explosions (see figure 2.25). Ripepe et al. (1993) propose a similar mechanism at Stromboli Volcano where they claims an inverse relationship between material ejection velocities (related to kinetic energy) and seismic reduced displacements (related to seismic energy). Ripepe et al. (1993) theorize that explosions have source directionality that is either vertical (with elevated ejection velocities) or radial (with strong seismic coupling into the ground).

As determined through video records at Karymsky in 1999, there is not an inverse relationship between ejection velocities (proportional to kinetic energy values) and either the acoustic reduced displacements or the seismic reduced displacements (see figure 2.15). There is a positive correlation between ejection velocity and acoustic signal strength, and no correlation between ejection velocity and seismic signal strength. In itself, this does not preclude a relationship between elevated kinetic energy and a deficit of radiated acoustic or seismic energy because ejection velocities are not necessarily representative of kinetic energy. A dense plume with a low ejection velocity may still have a high kinetic energy because of a surplus of entrained mass. Unfortunately, it is difficult to quantify the amount of mass entrained in a plume through visual observations.

For the Karymsky 1999 dataset, an attempt to measure the relative plume density is made by assessing the proportion of ejected juvenile material in a plume. Relative plume brightness, inferred from video observations in 1999, may be an indicator of low entrained mass because dense, ash-laden plumes are relatively dark. Relative explosion brightness can be determined from video by comparing the percentage of incandescent pixels in the plume which have grayscale values that exceed 60. This brightness index may be compared with seismo-acoustic amplitude ratios (see figure 2.27) to determine if there is a positive relationship between high acoustic efficiencies (relative to seismic) and low-density plumes. A positive correlation between brightness (low plume density) and relatively low kinetic energy (high acoustic efficiency) could substantiate the Mori et al., (1989) observations that dense plumes diminish the energy contained in acoustic waves. However, this relationship is not readily evident at Karymsky and the Mori et al. (1993) theory of variable transferal of acoustic energy to kinetic energy may not apply to the Strombolian explosions at Karymsky. It is possible that explosions at Langila have much more variable plume densities than explosions at Karymsky.

2.11.2 Variable Magma Impedance

Nicholls (1962) uses impedance contrast variabilities to explain coupling of explosive energy to rock (radiated seismic energy) for chemical explosives. Similarly Garces et al. (1998a) speculates that impedance contrasts between a fluid-filled conduit, the atmosphere, and the ground dictate the relative seismic and acoustic radiation efficiencies during volcanic explosions. Garces et al. (1998a) argue that a seismic source immersed in a fluid-filled medium transmits energy to the wall rock with an efficiency that is dependent upon the void fraction of the melt, a property which may vary over time. Experimental studies show that bubble-rich magmas may have densities as low as 1000 kg/m^3 and compressional wave velocities as low as 10 m/s [Miksis & Ting, 1986]. However, if the gas phase is absent from the magma, p-wave velocity can exceed 2000 m/s and the density may reach 2500 kg/m^3 [Miksis & Ting, 1986]. In these two
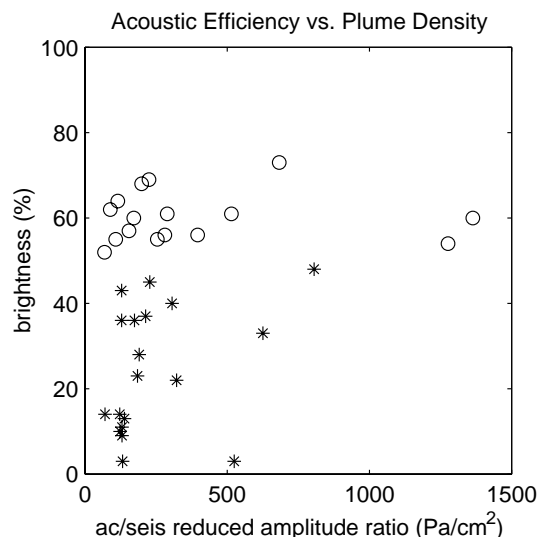
Acoustic Efficiency vs. Plume Density

Figure 2.27 Acoustic Energy vs. Plume Density - A comparison of acoustic efficiency (relative to seismic) with plume brightness (possibly related to plume density) for 35 Karymsky 1999 explosions. Starred events (*) denote brightness indices below 50% and circled events (o) correspond to brightness greater than 50%. There is no clear relationship between acoustic amplitudes and bright plumes (a possible indicator of low density explosions).

scenarios, perpendicularly incident seismic transmission coefficients across the boundary between melt and wall rock can vary by two orders of magnitude [Garces et al., 1998a].

The Garces et al. (1998a) model for isolation of radiated seismic energy is applied by Rowe et al. (2000) to explain a drop in observed seismic efficiency (relative to acoustic) for very small explosion sources at Erebus (reduced pressures less than ~100 Pa). Smaller explosion sources imply smaller bubbles which may not penetrate into the faster, denser portion of a stratified lava lake [Rowe et al., 2000]. At Karymsky, there is no obvious relationship between acoustic signal strength and relative energy partitioning (refer to figure 2.8 and 2.11), so variable seismo-acoustic energy partitioning appears not to be a size-dependent phenomenon.

Nevertheless, reduced acoustic pressures at Karymsky scale well with observed ejection velocities while reduced displacements have variable amplitudes that could conceivably be a function of magma impedance. Variable magma impedance may still be consistent

with the Garces et al. (1998a) model that uses time-varying melt properties rather than spatial variations to explain fluctuations in seismo-acoustic energy partitioning. However, temporal dependence implies that magma impedance must change dramatically over short time scales. For the double-pulse explosion displayed in figure 2.28, magma impedance would have to change by a factor of ~5 in less than one minute. In the upper portion of Karymsky's conduit, exsolved, microlite-rich andesitic magma has a high enough viscosity (greater than 10^5 Pa.s [Sparks, 1997]), that bubble nucleation and growth may not be able to occur at these time scales. Though further investigation is warranted, rapidly changing impedance contrasts is not the most plausible explanation for variable seismo-acoustic energy partitioning from a geochemical standpoint.
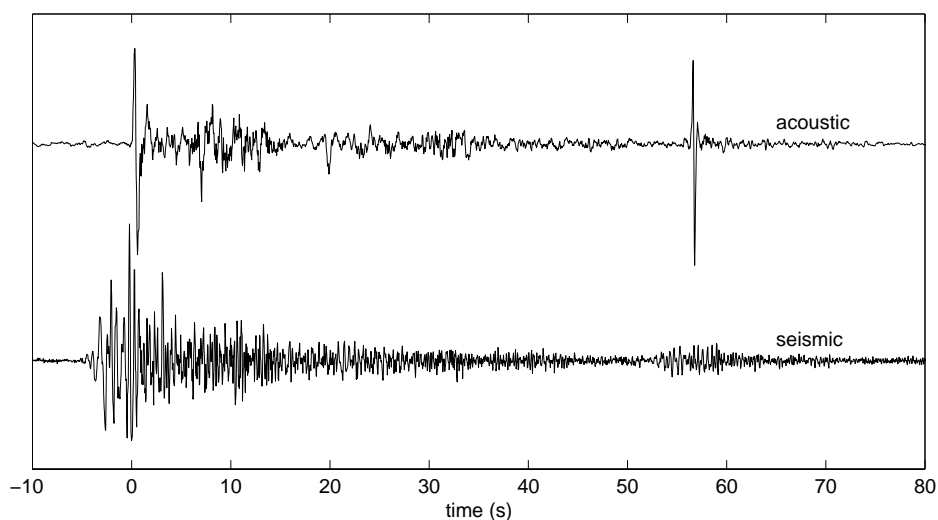
Figure 2.28 Karymsky Double Pulse Explosion With Variable Acoustic Efficiency - Double-pulsed explosion example from Karymsky (1998:248:17:02) demonstrates a rapid change from low acoustic efficiency (relative to seismic) to high acoustic efficiency for the second pulse.

2.11.3 Energy Dissipation in the Conduit

Observations at Shishaldin in 1998 reveal a dramatic increase in acoustic efficiency (relative to seismic) after a large eruption of juvenile material in the initial throat-clearing stage of the eruption [Thompson et al., in press; oral communication, Steve McNutt, 2000]. McNutt proposes that in the initial stage of the eruption, energy partitioning to the seismic wavefield is greatest because rocks are being fractured and the conduit reamed

open. In the later stage of the eruption, gas escapes easily through the open conduit and less seismic energy is required to eject gas and material.

An analogous though extreme scenario is the comparison of an explosion source that occurs freely in the atmosphere with an explosion source that is buried in the ground. In the underground explosion, the ground must rupture to the surface in order for escaping gas to produce infrasonic waves. Because aerial photos of the Karymsky summit crater reveal a vent choked with blocks and ash, it is likely that the Karymsky bubble foam fragmentation surface lies beneath a plug of variable depth. Thus muffling of gas emissions in the conduit and subsequent infrasonic signal diminution is the preferred model for explaining the variable seismo-acoustic amplitude ratios at Karymsky. If the conduit is cleared of debris, acoustic efficiency (relative to seismic) increases dramatically as evidenced by high-frequency jetting which tends to occur at the end of many explosion events. The explosion example in figure 2.29 shows an extended duration degassing event which terminates with a high amplitude acoustic signal and corresponding seismic signal that approach background levels. This type of event is very common in the Karymsky record.

Erebus explosions result from bubble rupture at the surface of a lava lake and do not contend with a conduit filled with impediments. Each explosion at Erebus is able to occur in a similar manner at the surface of the lava lake. Thus seismo-acoustic ratios are consistent and acoustic radiation (relative to seismic) is much more efficient than at Karymsky.

2.12 Model for Seismo-acoustic Energy Partitioning at Karymsky

Radiated acoustic energy at Erebus and Karymsky reflects the rate change of gas outflux from the vent. By Newton's 3rd Law, the acceleration of both gas and solid mass from the vent exerts a force upon the underlying magma. At Mount St. Helens, this force has been modeled as an inverted thrust or a terrestrial monopole by Brodsky et al. (1999) and
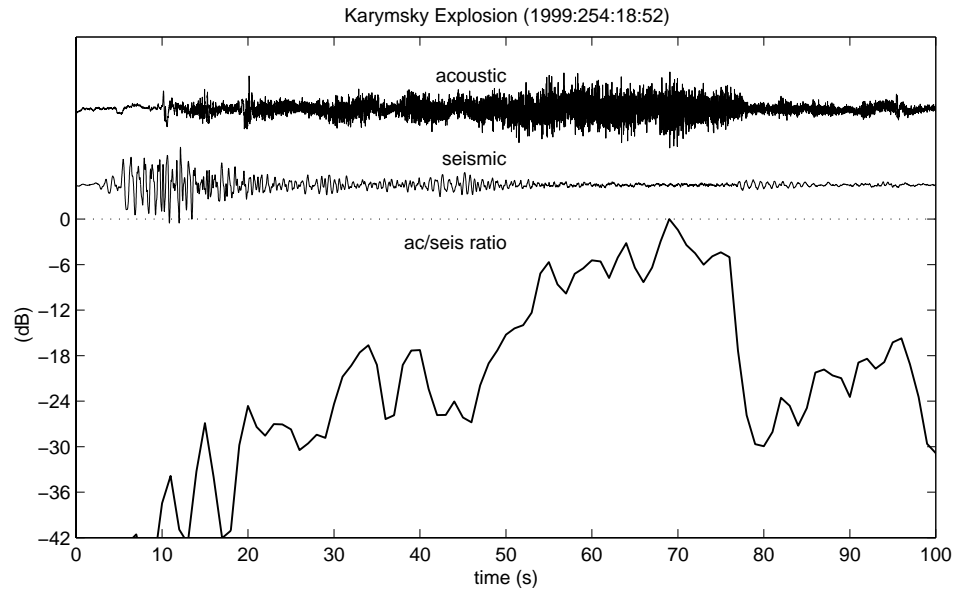
Figure 2.29 Karymsky Explosion With Increasing Acoustic Efficiency - Evolution of seismo-acoustic ratio for a selected event from Karymsky (1999:254:18:52). Normalized acoustic and seismic traces are plotted above the ratio of their smoothed envelopes. Acoustic and seismic envelopes are convolved with a 2-second box-car function to obtain a smooth ac/seis ratio plot.

Kanamori & Given (1982). At Erebus, a simple monopole appears also to be a reasonable mechanism for the thrust force exerted by gas vacating a burst bubble. Radiated body wave energy can be calculated in a wholespace according to Kanamori & Given (1982):

$$E_{seismic} = \frac{1}{6\pi\rho_e}\left[\frac{1}{2V_P^3} + \frac{1}{V_S^3}\right]\int_{-\infty}^{\infty}[\dot{F}(t)]^2 dt \tag{2.28}$$

$\dot{F}(t) =$ time derivative of force function

V_P and $V_s =$ body wave velocities

The effective force function ($F(t)$) is the critical unknown in equation 2.28. Kanamori & Given (1982) model their force function as a bell-shaped pulse:

$$F = \begin{cases} \frac{1}{2}f_o\left(1 - \cos\left(\frac{t}{\tau}\pi\right)\right) & \text{for } (0 < t < 2\tau) \\ 0 & \text{for } (t > 2\tau) \end{cases} \tag{2.29}$$

$$f_o = \text{maximum thrust force}$$

$$\tau = \text{duration of thrust}$$

For an ejected mass (M), it can then be shown that the maximum thrust force is equal to the net gain in momentum divided by the time constant (see appendix A):

$$f_o = \frac{MV}{\tau} \tag{2.30}$$

Combining equations 2.28-2.30 results in an equation for seismic energy that is dependent upon the cube of the time constant (see appendix A).

$$E_{seismic} \approx \frac{\pi}{24} \frac{(MV)^2}{\rho \tau^3} \left[\frac{1}{2V_P^3} + \frac{1}{V_S^3} \right] \tag{2.31}$$

For reasonable values of momentum (10^5 kg·m/s using a mass of 10^3 kg, ejection velocity of 10^2 m/s), reasonable body wave velocities (10^3 m/s), and reasonable earth densities (2.5×10^3), the time constant (τ) must be on the order of 10^{-2} seconds. This constant indicates the time necessary to accelerate gas and magma to the vent muzzle velocity. This acceleration of gas is directly responsible for the generation of infrasound at Erebus which is why acoustic and seismic energies scale with each other.

A similar thrust force is a likely source of seismic energy at Karymsky, but the force balance is more complicated because the source does not occur directly at the free surface. For bubble foam fragmentation that occurs at some depth within the conduit, gas acceleration from the vent (infrasound amplitude) is diminished as conduit flow imparts energy to the walls (seismic wave generation) and net energy is lost (through viscous dissipation). Energy dissipation by viscous flow and conduit wall interaction results in a conduit head loss so that the effective vent overpressure is less than the overpressure in the original bubble foam (see equation 2.23). In section 2.11.3, this loss was treated as non-recoverable. However, under appropriate conditions, some of the energy could be transferred to seismic wave radiation due to interactions with the wall rock.

For high Reynolds Number flows, energy dissipation due to viscous fluid flow through a pipe is proportional to a non-dimensional empirical friction factor (f - see equation 2.26) that can depend upon conduit wall roughness [Fay, 1994]:

$$f = \frac{1}{4\log\left(\frac{\varepsilon/D}{3.7}\right)^2} \tag{2.32}$$

$$\varepsilon/D = \text{wall roughness height ratio}$$

In equation 2.32, the wall roughness ratio (ε/D) is defined as the average dimension of protruberances divided by the width of the conduit. Though the conduit wall roughness during volcanic degassing is an unknown parameter, a hypothetical wall roughness ratio of 0.1 produces a frictional factor of approximately 0.1. The total energy dissipation caused by rough conduit walls in this scenario then becomes (from equation 2.26 and 2.32):

$$E_{Walls} = \frac{1}{25}\rho_f \bar{V}^3 LDt \tag{2.33}$$

For turbulent Poiseulle Flow, equation 2.33 can be rewritten in terms of mass (see appendix A):

$$E_{Walls} \approx \frac{4}{25\pi}M\bar{V}^2\frac{L}{D} \tag{2.34}$$

Reasonable flow parameters for Karymsky explosions may have total masses on the order of 5×10^3 kg, flow velocities ranging from 10^1 to 10^2 m/s, and conduit length-to-width ratios ranging from 10^1 to 10^2. In this scenario, total energy dissipated by wall friction is 10^5 to 10^8 Joules. Radiated seismic trace energy at Karymsky, ranging between 10^4 and 10^6 Joules, would then be only a fraction of the total wall dissipation energy. Therefore, the majority of the wall dissipation energy is probably lost as heat.

For Karymsky explosions, it is possible to envision variations in conduit geometry or flow velocity that dramatically affect the conduit wall dissipation energy. The effective conduit length is very likely to change for different explosions as the bubble foam

Karymsky Explosion

before explosion

degassing onset

degassing coda

debris

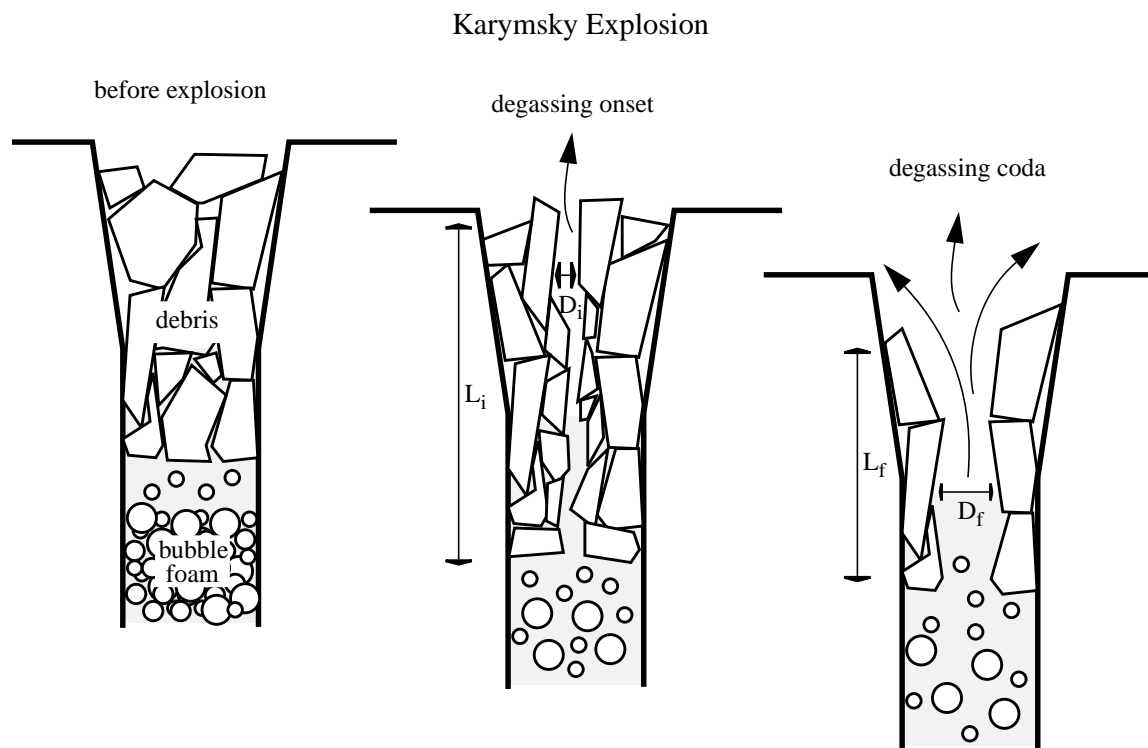D_i

L_i

bubble foam

L_f

D_f

Figure 2.30 Karymsky Model for Changing Seismo-Acoustic Energy Partitioning - Cartoon of potential conditions in the conduit at Karymsky showing the transformation from low acoustic efficiency (relative to seismic) to high acoustic efficiency for the explosion example shown in figure 2.29.

fragmentation front migrates to different levels within the conduit. The conduit width is also liable to change dramatically as the flow of gas widens the aperture through which gas and magma escape. This variation in conduit width is the most likely mechanism for the commonly observed increase in acoustic efficiency (relative to seismic) that occurs towards the end of extended-duration Karymsky explosions (refer to figures 2.29-2.30).

2.13 Summary and Conclusion

Strombolian explosions encompass a relatively large range of magma types and are not limited to the basalt of Stromboli, phonolite of Erebus, or andesite of Karymsky. Although each of these volcanoes is able to generate discrete and frequent VEI I or VEI II explosions, degassing mechanisms at the volcanoes may be quite different. Erebus explosions, for example, are highly repeatable, nearly instantaneous gas bubble bursts

from the surface of a lava lake, whereas Karymsky explosions involve longer duration degassing from some depth within the conduit. Erebus explosion elastic energy is consistently partitioned between acoustic and seismic wavefields whereas Karymsky explosions exhibit variable seismo-acoustic amplitude ratios. Finally, acoustic energy is radiated more efficiently at Erebus than at Karymsky. For two explosions with the same associated seismic reduced displacement, the corresponding Erebus infrasonic pulse averages about 20 dB 'louder' than the Karymsky infrasonic signal.

At the onset of Karymsky explosions, gas release is impulsive and acoustic amplitudes scale well with observed muzzle velocities. Associated reduced seismic amplitudes do not scale well with the muzzle velocities because the radiated seismic energy is highly dependent upon ephemeral properties of the conduit. Conditions in the conduit of Karymsky, such as the depth of the fragmentation front, crack widths, and/or gas escape velocity may be highly variable and can change during the course of an explosion. Hence acoustic magnitudes often scale poorly with seismic amplitudes. At Erebus, the bubble rupture location and lava lake conditions are fixed, resulting in consistent seismo-acoustic partitioning for all explosions.

In terms of the total energy budget at both Erebus and Karymsky, radiated elastic energy (acoustic and seismic) is only a fraction of the total potential energy released during the expansion of compressed volcanic gases. For the three datasets, seismic trace energy ranges from 10^3 to 10^7 Joules and acoustic trace energy ranges from 10^4 to 10^7 Joules. Kinetic energy is roughly comparable to the acoustic radiation while potential energy released from the expansion of gases during Karymsky and Erebus explosions is probably close to 10^9 Joules. The inefficiency of elastic energy radiation likely reflects viscous dissipation within the conduit or lava lake and an inefficient transferal of energy into the acoustic and seismic wavefields. Radiated elastic energy efficiencies on the order of 1% are similar to seismic efficiencies from both tectonic earthquakes [Dobrovol'skiy, 1994] and underground explosions [Duvall & Stephenson, 1965].

Chapter 3 - Interpretation and Utility of Infrasonic Records from Erupting Volcanoes

3.1 Chapter Overview

In the most rudimentary seismo-acoustic studies, infrasound monitoring enables differentiation between sub-surface seismicity and the seismicity associated with gas release. Under optimal conditions, complicated degassing signals can be understood, relative explosion size can be assessed, and variable seismo-acoustic energy partitioning can be interpreted (refer to chapter 2). The extent to which these points can be investigated depends upon the quality of the infrasonic records (a function of background wind noise, microphone sensitivity, and proximity of microphone to the source) and the type of activity generated by the volcano (frequency of explosions, bandwidth of the signals, and coupling efficiency of explosion energy to acoustic energy). To illustrate the benefits and limitations of infrasonic recordings at volcanoes, this chapter showcases acoustic and seismic records from five volcanoes characterized by explosive degassing events. These five volcanoes (Erebus in Antarctica, Karymsky in Russia, and Sangay, Tungurahua, and Pichincha in Ecuador) are the focus of seismo-acoustic experiments in the last three years. Each case study provides background information about the volcano along with visual observations of the eruptive activity and associated seismo-acoustic data. The infrasonic records and eruptive activity from the five volcanoes are compared to one another and to other volcanoes that have also been the focus of infrasonic studies.

3.2 Introduction

This chapter offers an overview of seismo-acoustic experiments at five active volcanoes with different eruptive styles. Activity at these sites ranges from low and medium viscosity Strombolian explosions to Vulcanian activity and high-silica volcanism associated with an active dome. The field sites are introduced in the order of their relative eruptive vigor, beginning with Erebus and concluding with Pichincha. Each

volcano has a short section describing the background and experiment, data overview, and utility of infrasonic monitoring at that particular site. The chapter provides examples of seismo-acoustic signals, associated frequency spectra, and observations of associated volcanic degassing at volcanoes with different behaviors. Though various degassing models are discussed here, detailed analysis and interpretation of the signals are beyond the scope of this chapter. In general, data is left in a raw, unfiltered format and normalized acoustic pressure traces and raw velocity seismograms are used exclusively. For more analysis of the Karymsky and Erebus datasets, where well-calibrated microphone arrays allow comparisons of the acoustic and seismic signal amplitudes and energy radiation, refer to chapter 2. For further information on the specifications of the microphones used at the various deployments, refer to appendix B.

3.3 Erebus:

3.3.1 Background

Erebus is a 3700 meter-high shield volcano located on Ross Island, Antarctica (see figure 3.1). Since it was first sited in 1841 it has been in a continuous state of degassing. Erebus is unique because it possesses a permanently convecting lava lake through which gas freely ascends without a corresponding flux of magma [Rowe et al., 2000]. The composition of the lava lake is a phonolite, a highly alkalic magma with basic to intermediate silica content. Phonolite is a high-temperature, relatively rare magma with viscosity similar to basaltic magmas [Dibble et al., 1984]. Eruptive activity from the Erebus lava lake during the period of study, from November 1999 through January 2000, was characterized by explosive gas bubble ruptures which were able to eject small bombs approximately 400 meters vertically up and over the crater rim [Bjorn Johns, personal communication, 2000]. These bubble ruptures originate from a 10 meter radius lava lake skylight in the floor of the crater [Rick Aster, personal communication, 2000].

Figure 3.1 Photos of Erebus - a) View from McMurdo towards Erebus 40 kilometers to the north.

Figure 3.1 (continued) Photos of Erebus - b) Erebus lava lake as seen from the crater rim ~200 meters above the floor. Photo courtesy of B. Johns.

During the 1999-2000 field season, 5 stations equipped with McChesney 4-element microphones and broadband seismometers (STS-2 and CMG-3T) were deployed 670 meters to 2450 meters from the lava lake (see figure 3.2). Recording was continuous at

40 samples per second on portable Reftek dataloggers. The nearest seismo-acoustic station to the vent (EE1S) was co-located with a Dibble pressure transducer microphone and a station 1900 meters from the vent (EHUT) was equipped also with a Larson-Davis free-field precision microphone. The temporary network recorded 2 to 5 explosions each day for nearly two months.
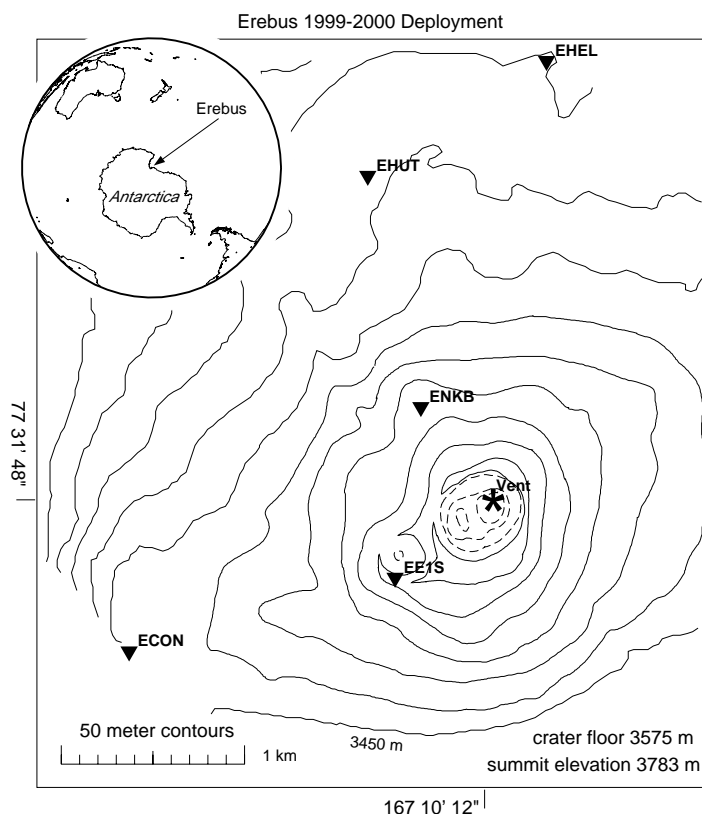
Figure 3.2 Erebus Station Map - Erebus 1999-2000 deployment map. Each of the five stations was equipped with a broadband seismometer and microphone(s). Stations EE1S and EHUT were equipped with two microphones each for calibration purposes.

3.3.2 Data Overview

Although occasional periods of windy weather corrupted portions of the infrasonic pressure traces (see long duration acoustic tremor signals in figure 3.3), about 90 percent of the explosions at Erebus were recorded clearly on the acoustic channels. This high recovery rate can be attributed to the wind-filtering benefits of the overlying snow, spatial

filtering of the 4-element microphones (see appendix B), proximity of the microphones to the explosion source, and relatively high amplitude of infrasonic pulses. All of the recorded acoustic signals from Erebus in 1999-2000 are very simple explosion events, beginning impulsively and having minimal coda. Consistent lag times between seismic and acoustic phases and self-similarity of seismic and acoustic wavelets for different explosions (see figure 3.6), indicate a very repeatable source. These explosion signals are very similar in appearance to the infrasonic pulses recorded at Stromboli Volcano [Vergniolle et al., 1996]. At both Stromboli and Erebus, large bubbles (radius greater than 1 meter) have been observed rising to the surface of a fluid magma and forming blisters before bursting.

Travel time differences between acoustic and seismic phases are dependent upon epicentral distance (see figure 3.4). Because acoustic arrivals are so impulsive, apparent acoustic velocities can be easily determined for infrasound crossing the array. For a suite of explosions, acoustic apparent velocities are 315 m/s +/- 5 m/s corresponding to temperatures ranging from negative 34 to negative 23 degrees Celsius (typical conditions at Erebus). Seismic arrivals are extremely emergent with estimated first arrival apparent velocities of about 3000 m/s. This velocity is comparable to P-wave velocities determined at Erebus by Dibble et al. (1994). With the resolution afforded by the seismo-acoustic array at Erebus in 1999-2000, it appears that the onset of both acoustic and seismic signals emanate from a synchronous source at the vent. There is no evidence of precursory seismicity prior to bubble rupture for Erebus explosions.

Low acoustic phase velocities enable accurate locations of explosion sources. Erebus explosion source locations can be determined by examining arrival times at an array of microphones. Interpreted explosion epicenters (see figure 3.5) correspond to the location of the lowest total of mean squared distance residuals (using a grid search with 2-meter resolution, equal weighting for all five stations, and a homogenous atmospheric velocity structure). Erebus explosion epicenters, determined from the five station array, have a
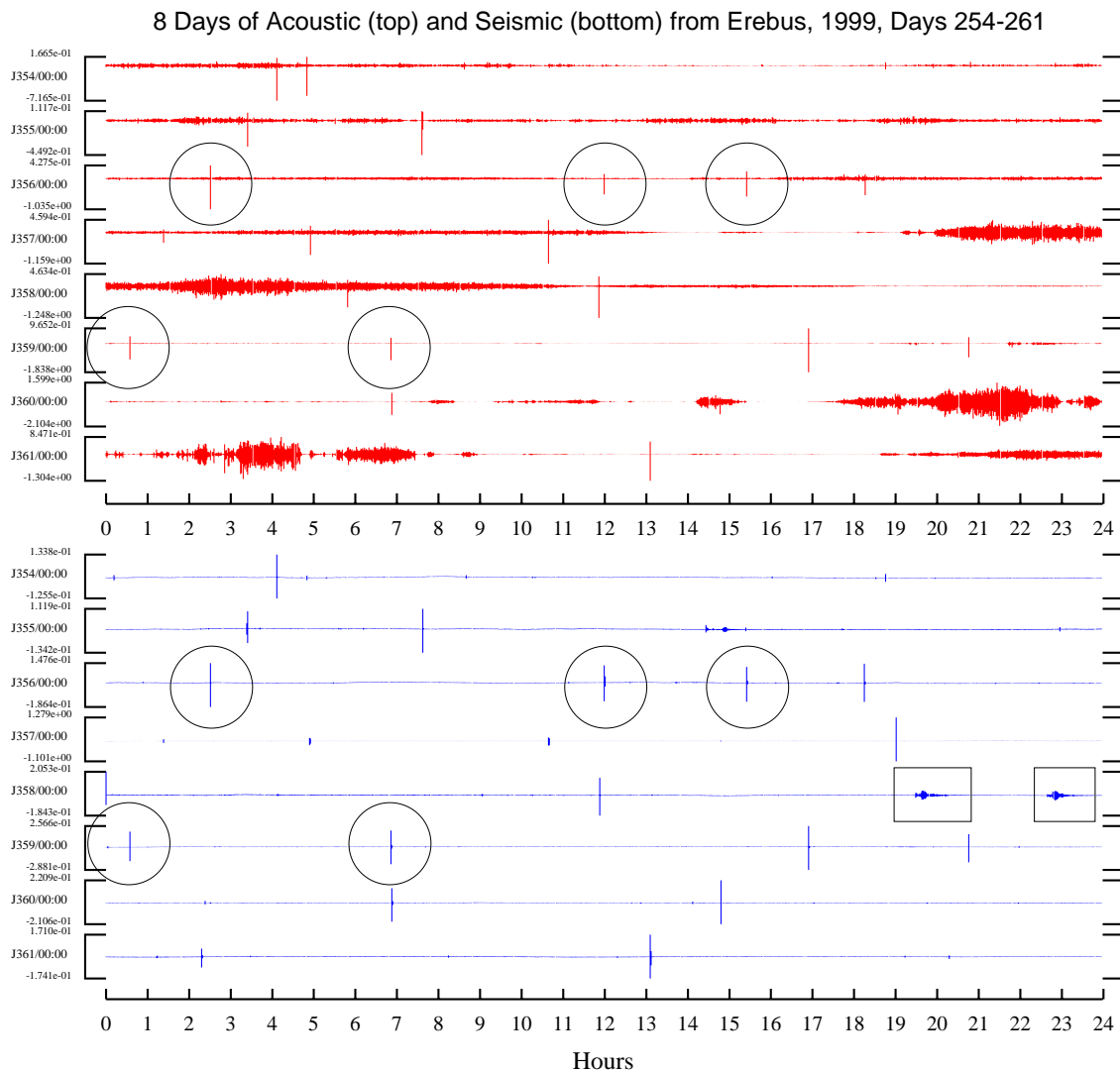
Figure 3.3 Erebus 8-day Acoustogram and Seismogram - Eight days of activity recorded at station EHUT (acoustic - top) and EE1S (seismic - bottom), days 254-261, 1999. Acoustic data is displayed from EHUT rather than EE1S because many acoustic signals are clipped at EE1S. Selected events (indicated by boxes) are teleseisms. Long-duration acoustic tremor-like signals in the top panel represent periods of high wind noise. Circles indicate events displayed in figure 3.6

spatial standard deviation of 9 meters. During the 1999-2000 field season, the phonolitic lava lake had a fixed position with a radius of 10 meters [Rick Aster, personal communication, 2000], implying that the interpreted source location variability is an effect of changeable temperature or wind structure.
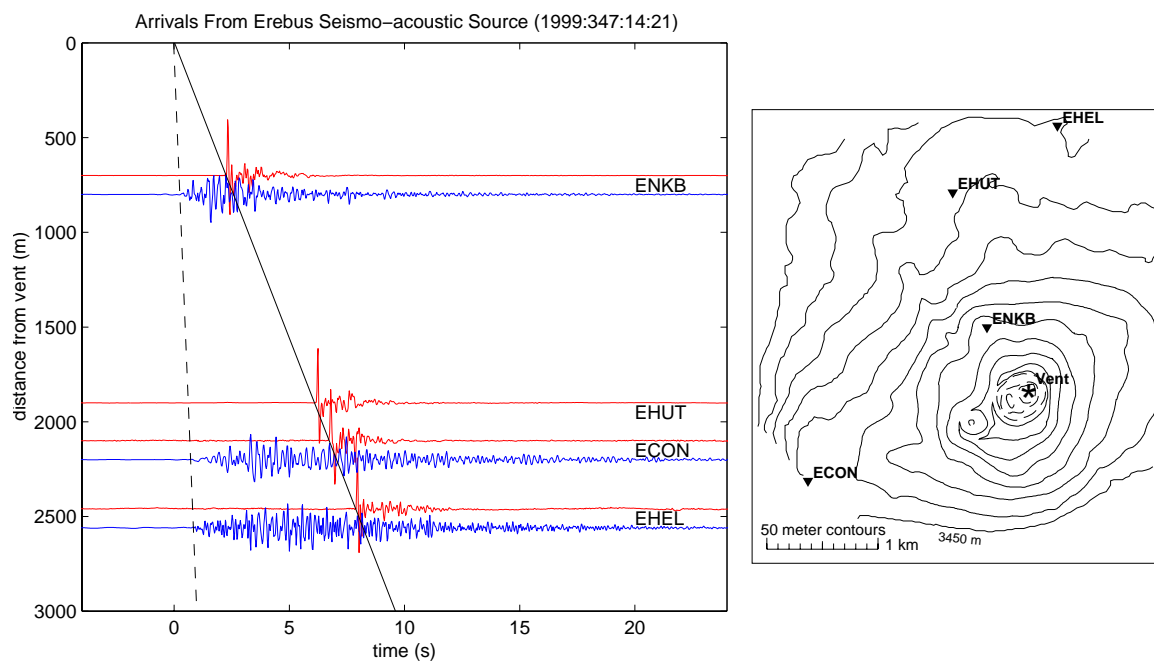
Figure 3.4 Erebus Explosion Seismo-acoustic Arrivals - Erebus explosion recorded at several stations reveals phase velocities for acoustic and seismic waves. Seismic velocity traces are filtered above 2 seconds to remove tidal noise. Apparent acoustic velocity is 313 m/s and apparent seismic velocity of the first arrivals is 3000 m/s. Body wave velocity is difficult to accurately determine due to emergent nature of the seismic waveforms.

All explosive events from Erebus are highly repeatable and correspond to bubble ruptures at the surface of the lava lake. Regardless of event size, the self-similarity of acoustic explosion signals lasts for more than 5 seconds (see overlay in figure 3.6). This short acoustic 'coda' is likely to be an artifact of propagation and may indicate reflections off the crater wall. In the overlay in figure 3.6, a second compressional pulse (marked by an arrow) follows the original acoustic pulse by about 1.7 seconds, suggesting a wall reflection about 260 meters from the vent. This dimension is compatible with the size of the Erebus crater which has a 400-meter radius.

3.3.3 Utility of Acoustic Monitoring

A defining characteristic of Erebus eruptive activity is its relatively low-viscosity phonolitic magma lake and the observation of large intact bubbles bursting at the surface [Dibble, 1994]. The absence of an acoustic coda in association with the explosion events
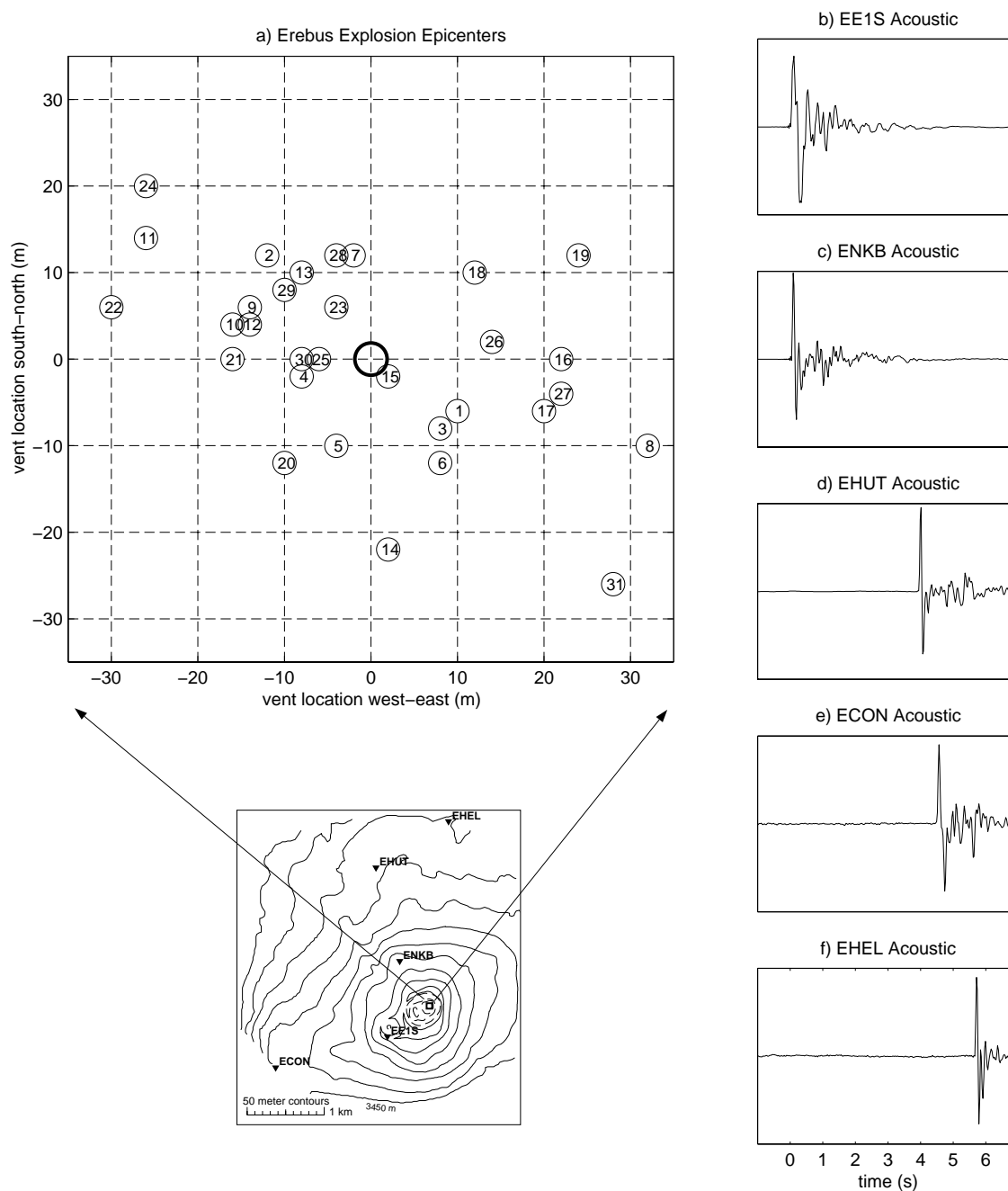
Figure 3.5 Erebus Vent Locations - a) Vent locations for a suite of 31 Erebus explosions (numbered chronologically) occurring between 1999:347:14 and 1999:362:08. Epicenters were determined by grid search assuming a homogeneous atmospheric velocity structure. b-f) An example explosion (event #1 - 1999:347:14:21) is shown as recorded by the five infrasound stations in the array.
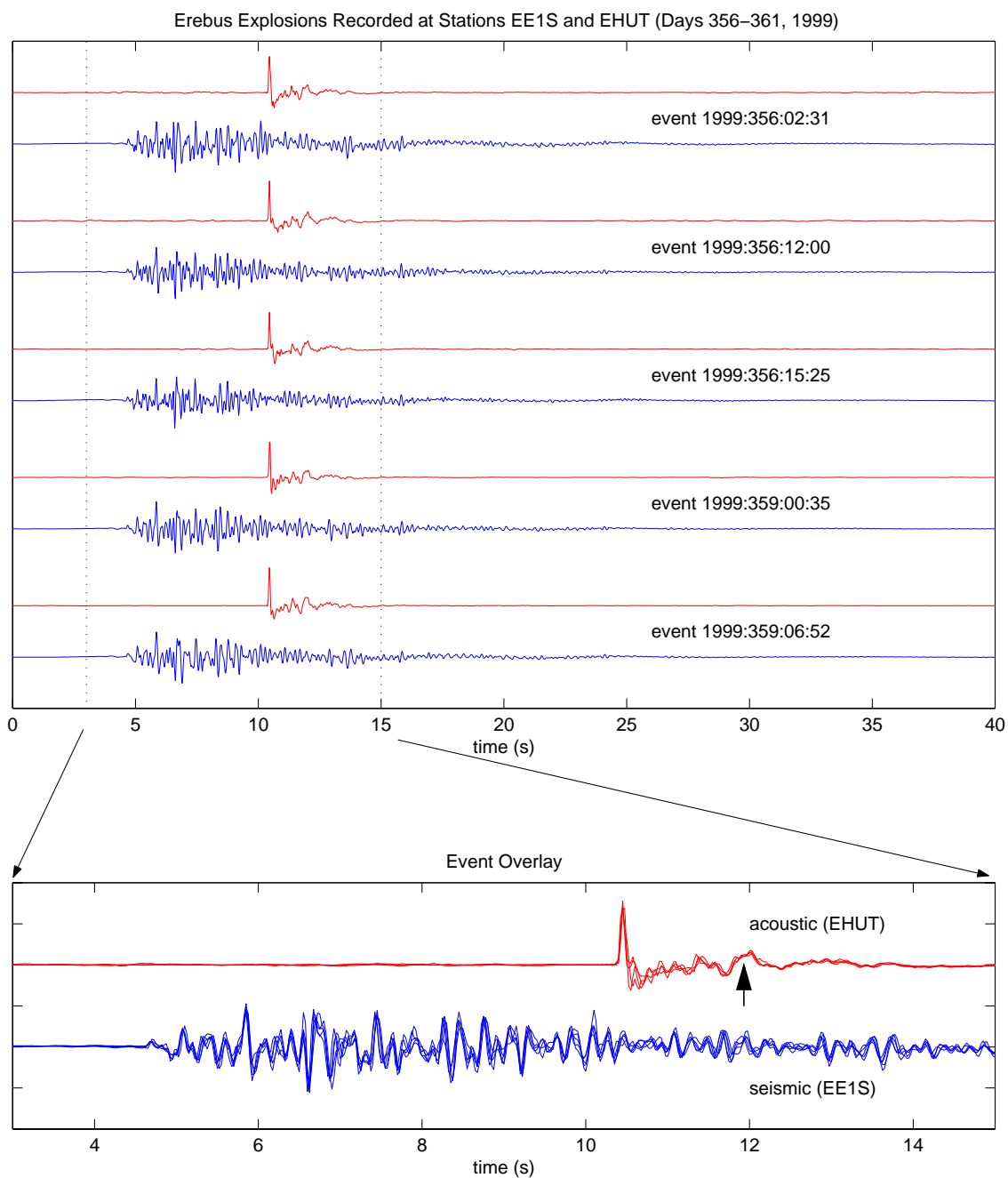
Figure 3.6 Erebus Explosion Examples - Selected normalized explosion waveforms from figure 3.3 (indicated by circles). An overlay of five events is shown at bottom. Seismic and acoustic signals show excellent self-similarity. Arrow in event overlay points to a possible echo off the Erebus crater wall.

is evidence for the open nature of the Erebus plumbing system. It is probable that all degassing events at Erebus during the 1999-2000 field season were manifested as bubble bursts at the surface of the lava lake. Variations in explosion size recorded on the seismic and acoustic channels probably reflect the volume of gas released from the bursting bubbles (refer to chapter 2).

Erebus serves as a low-viscosity endmember for explosive volcanic degassing. Because of the low viscosity, bubbles are able to rise relatively unhindered through the conduit until they reach the surface of the lava lake, generating relatively simple, short, repeatable explosions. The study at Erebus provided good azimuthal and radial coverage of the acoustic wavefield by well-calibrated microphones enabling good constraints of the explosion source-pressure time histories. The influences of weather upon inferred vent location (see figure 3.5) and acoustic pressure amplitudes (see chapter 2) can thus be studied in great detail. Microphone arrays such as the one deployed at Erebus are especially valuable for filtering out weather variations and recovering true explosion source parameters.

3.4 Karymsky (1997-1999):

3.4.1 Background

Karymsky Volcano (see figure 3.7), is a 1540 meter-tall andesitic cone located in the central portion of Kamchatka's main active arc. It began its latest eruptive phase in January, 1996 after 14 years of quiescence [Gordeev et al., 1997]. Though vigorous Vulcanian activity characterized the eruption onset, activity settled to discrete Strombolian events by the summer of 1996. Between 1996 and 1999, Karymsky's behavior consisted of discrete Strombolian explosions, with a frequency ranging from 5 to 20 events per hour. A flux of magmatic materials in the form of bombs and block lava flows accompanied the Strombolian explosions. Periods of relative explosive vigor, with associated energetic block lava flows extending over a kilometer from the summit vent, characterized activity during the summers of 1996 and 1998. The composition of lava

from recent flows at Karymsky averages 62.20 weight percent silica [Ivanov et al., 1991]. Since 1999 explosion frequency has dropped considerably [Evgenii Gordeev, personal communication, 2000], indicating that Karymsky may be settling into another characteristic period of dormancy.

Figure 3.7 Photos of Karymsky - a) View of summit crater and gas emissions from 1998.

Figure 3.7 (continued) Photos of Karymsky - b) View from the base of the active block lava flow of 1998 ~1300 meters from vent. Photo courtesy of L. Clabaugh.

Three field trips to Karymsky (August, 1997, September, 1998, and September, 1999) provided three high-quality datasets of acoustic and seismic recordings. In all experiments, portable Reftek dataloggers were deployed on the lower flanks of the volcano 600 meters to 900 meters beneath the summit vent and 1500 meters to 5000 meters distant (see figures 2.2a-c). Most seismo-acoustic stations were equipped with three-component broadband seismometers and either one or two microphones. Recording sample rates were either 100 or 125 samples per second.

In the 1997 field season (see figure 3.8a), 1 Ripepe microphone and 1 Ramey differential pressure transducer microphone were co-located with a CMG 40-T broadband seismometer that operated for three days at station Kar1 (1620 meters from the active vent). During the study, discrete explosive events occurred an average of 10 times each hour. In the 1998 field season (see figure 3.8b), 8 electret condenser microphones (1 Larson-Davis free-field precision microphone, 4 Ripepe microphones, and 3 Venema microphones) were deployed at epicentral distances ranging from 1500 to 3000 meters. Each microphone was co-located with either a CMG 40-T or a short-period seismometer. The experiment lasted 9 days with individual campaigns lasting one to two days. Campaign geometries included a linear array pointing radially towards the vent, an array with azimuthally distinct station locations, and calibration tests in which all microphones were co-located at a single site. In 1998, explosive events occurred on average 15 times each hour. During the 1999 field season (see figure 3.8c), 8 electret condenser microphones (1 Larson-Davis free-field precision microphone, 1 Venema microphone, and 6 McChesney microphones) were deployed for four days at five stations with epicentral distances ranging between 1500 meters and 5000. Several stations housed multiple microphones for calibration and wind filtering purposes (refer to appendix B for information on microphones and wind filtering). Three CMG 40-T and 2 STS-2 broadband seismometers were co-located with the microphones. On average, explosive events occurred 8 times each hour.

a) Karymsky 1997 Deployment

b) Karymsky 1998 Deployment
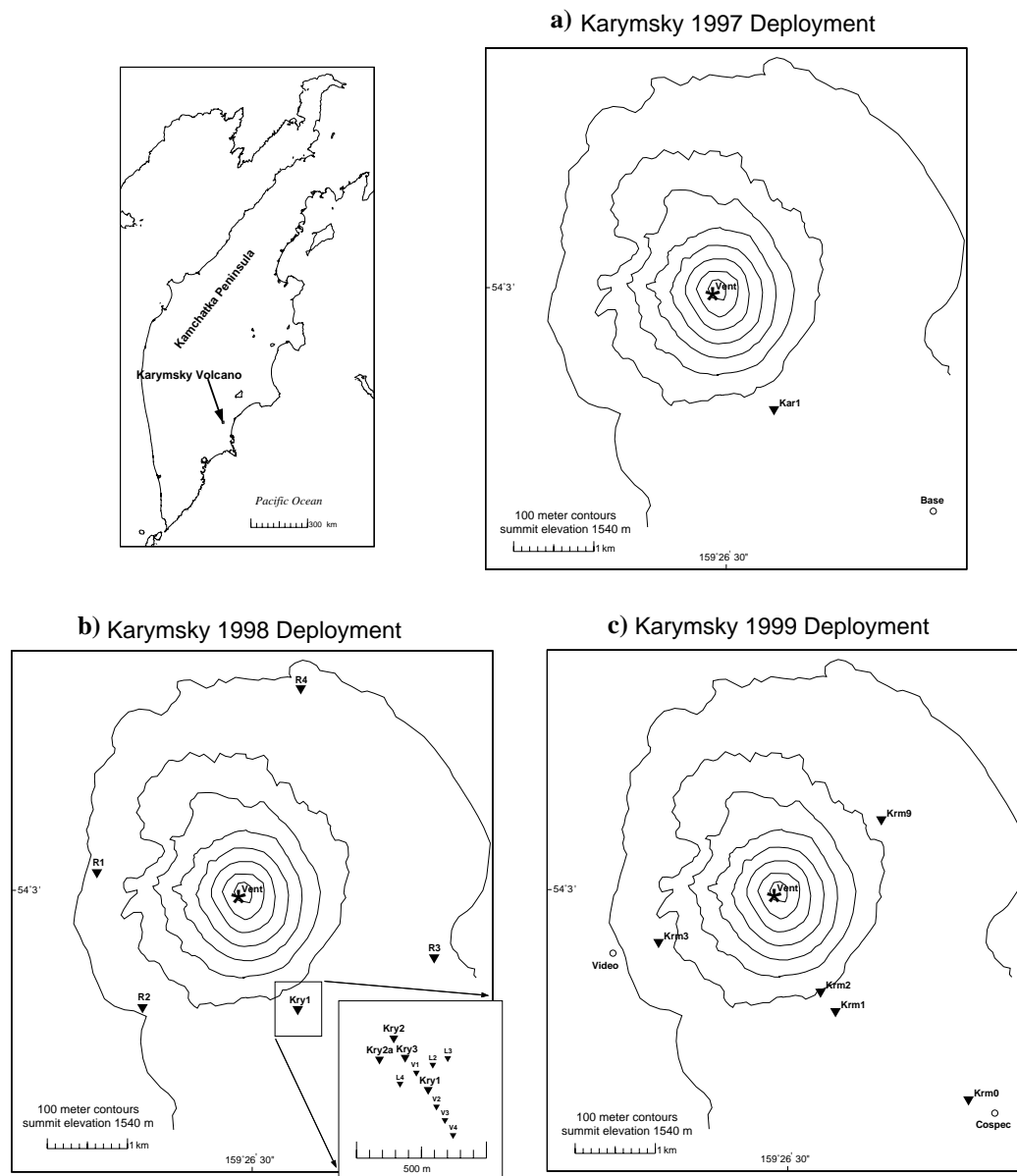
c) Karymsky 1999 Deployment

Figure 3.8 Karymsky Station Maps - a) Karymsky 1997 deployment map. Station Kar1 contained seismometer and microphones. b) Karymsky 1998 deployment map. All marked stations contained microphones and seismometers. Stations L1-4, V1-4, and R1-4 were each part of individual campaigns lasting one or two days while stations Kry1-3 were fixed for the duration of the experiment. The COSPEC scanner was located in the southeast quadrant of the map about 3 km from the vent. c) Karymsky 1999 deployment map. Video camera and COSPEC sites are marked along with seismo-acoustic station locations.

3.4.2 Data Overview

Virtually all seismic signals recorded during the three experiments at Karymsky were accompanied by acoustic signals whenever background acoustic noise is low (see figures 3.9a-c). Wind noise is a persistent problem in all three Karymsky datasets (see appendix B) that is able to partially obscure acoustic signals in about 50 percent of the explosions and completely obscure signals in an additional 15 percent of the explosions (see portions of acoustogram in figure 3.9c). Wind typically appears as a tremor signal lasting tens of seconds to hours that tends to be more prominent during daytime recording. Fortunately, the abundance and repeatability of explosions at Karymsky compensate for periods of time when acoustic data is of poor quality.

With only one exception (a regional magnitude 4.3 earthquake occurring at 1998:252:03:52:42 - see appendix C), all seismic events can be associated with acoustic signals and visual observations of ash plumes issuing from the summit vent. Karymsky explosion onsets are nearly always characterized by rapid gas and/or ballistic emission followed by gas effusion which tapers off during the course of several minutes. Discrete explosions are separated by time intervals of several minutes during which degassing is not visible. Incandescent emissions are visible only at night and most commonly at the onset of explosions.

For all Karymsky events, the explosion onset is an impulsive compressional acoustic pulse which follows an emergent seismic signal by a consistent, fixed time that is dependent upon the distance between the vent and recording station. The travel time difference between first seismic arrivals and first acoustic arrivals is roughly equal to the source-receiver distance times 2.1 seconds/km (for seismic velocities of 1200 m/s and acoustic velocities of 340 m/s). In actuality, the lag time between acoustic and seismic phase arrivals varies by about 2 percent which can be attributed to changeable weather conditions (refer to chapter 1). As at Erebus, explosion source locations can be determined by interpretation of acoustic arrival times at multiple stations. Figure 3.10
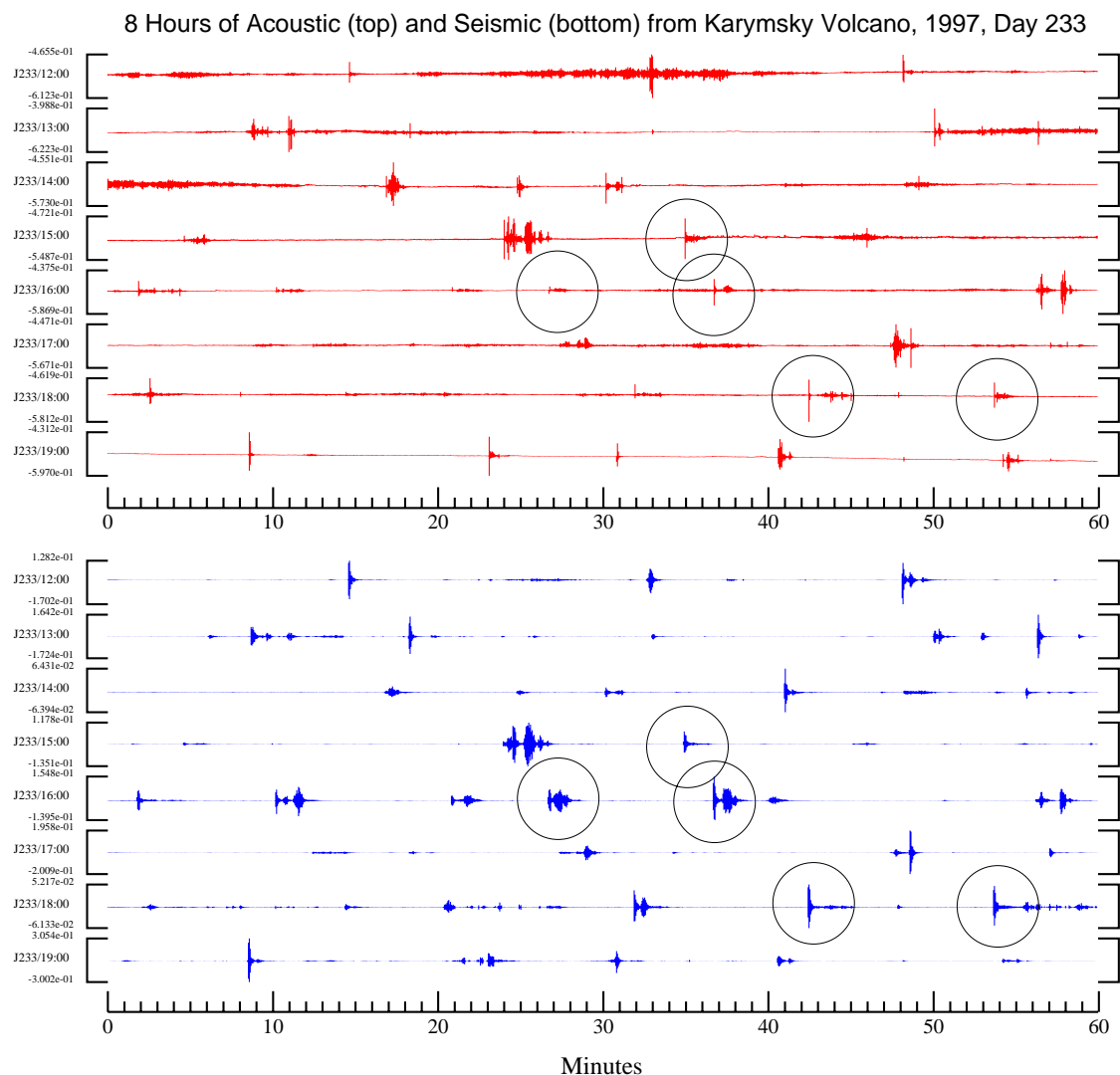
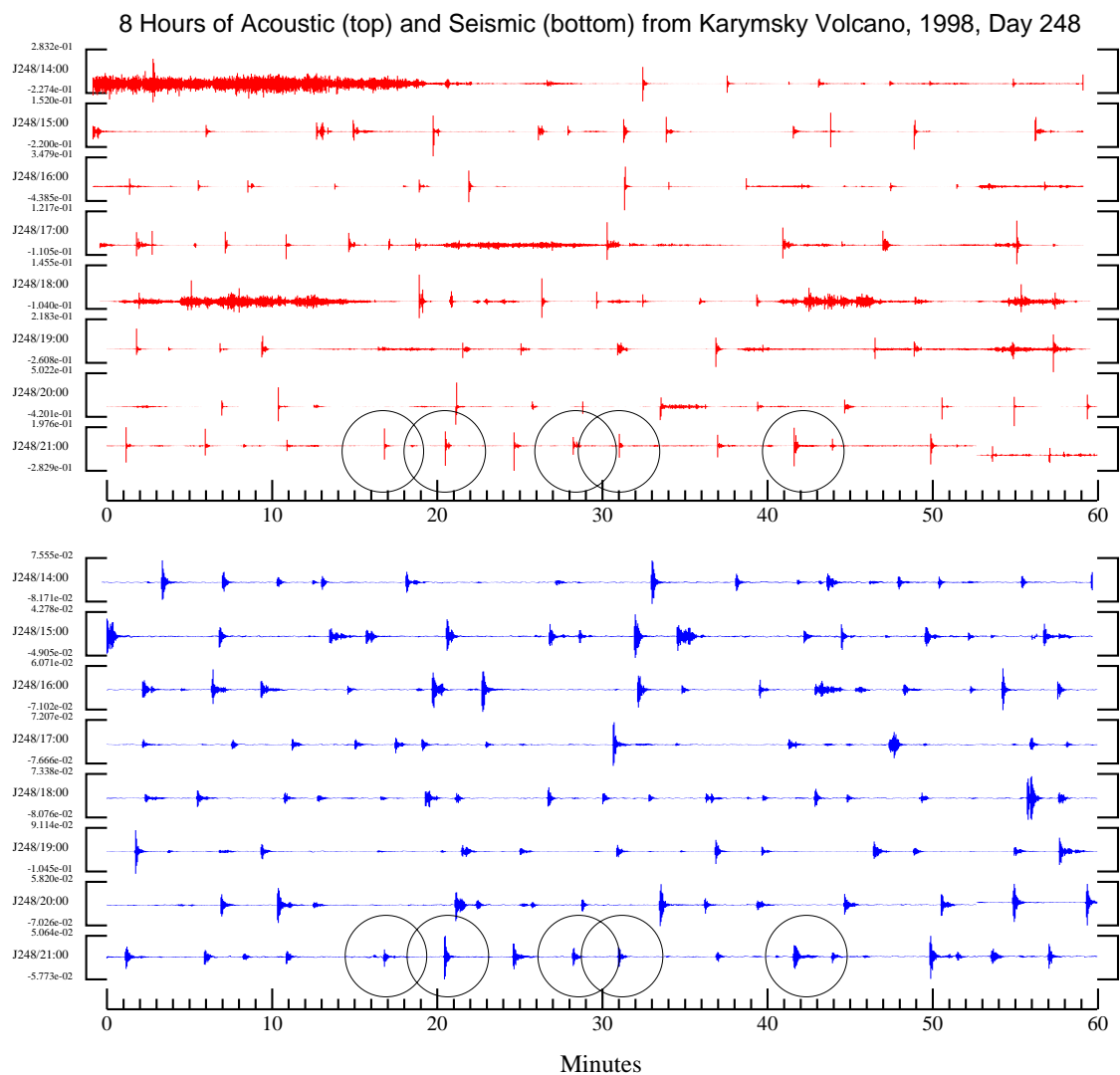**Figure 3.9 Erebus 8-hour Acoustogram and Seismogram - a) Eight hours of activity recorded at station Kar1, day 233, 1997. Acoustic signals are recorded with a Ripepe microphone (top) and seismic signals are recorded with a CMG-40T broadband seismometers (bottom). Circles indicate events which are displayed in figure 3.13a.**

shows a suite of inferred vent epicenters corresponding to lowest total mean square distance residuals (using a grid search with 2-meter resolution, equal weighting for three stations, and a homogenous atmospheric velocity structure). Since the vent is physically confined to the floor of the small summit crater (see figure 3.7a), the spatial standard deviation of 6 meters for vent locations is due to wind variability. Epicenters that are consistently offset for periods of time lasting several hours (explosions 40-57 in figure
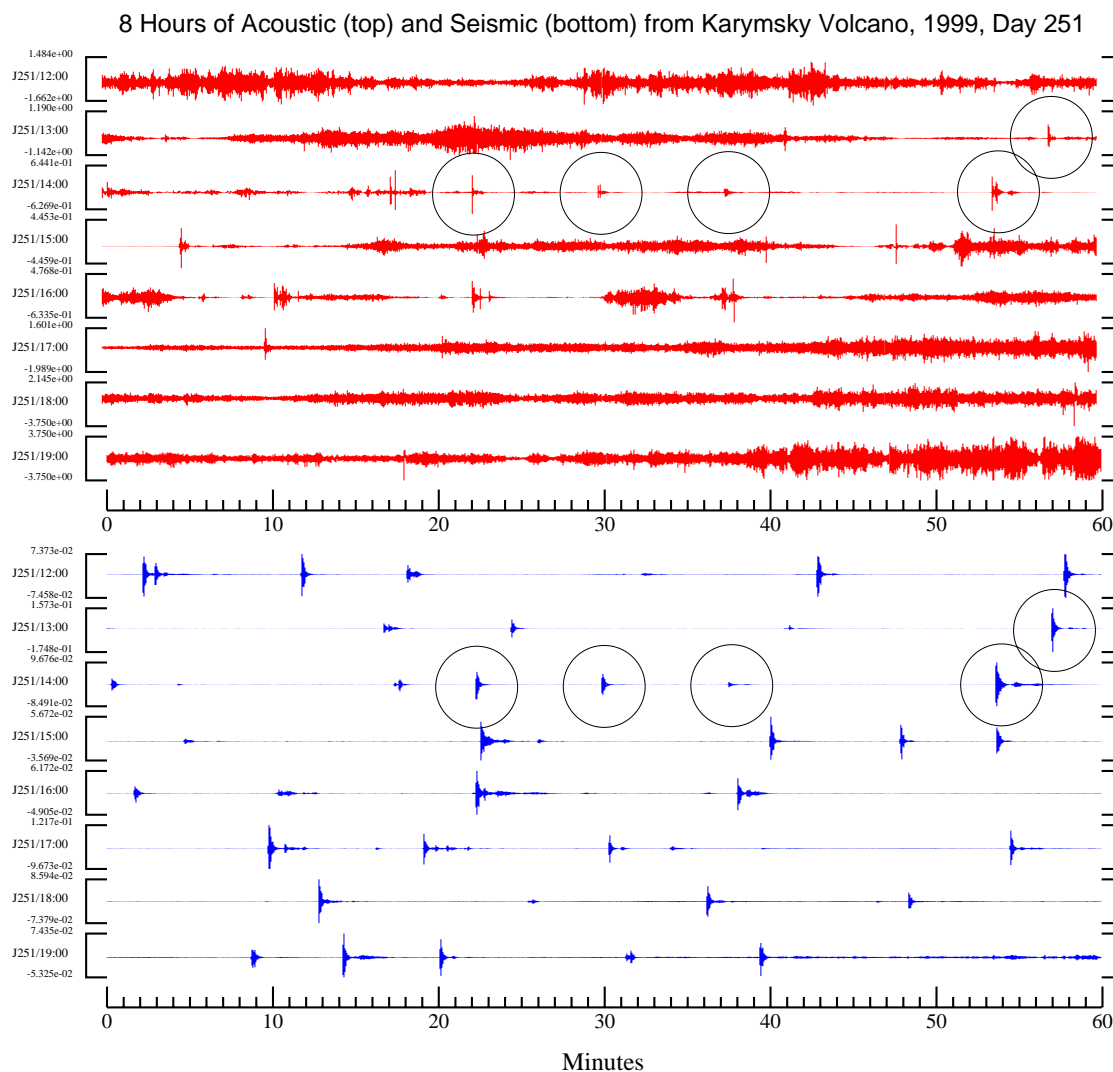
Figure 3.9 (continued) Erebus 8-hour Acoustogram and Seismogram - b) Eight hours of activity recorded at station Kry1, day 248, 1999. Acoustic signals are recorded with Larson-Davis microphone (top) and seismic signals are recorded with CMG-40T broadband seismometers (bottom). Circles indicate events which are displayed in figure 3.13b.

3.10) indicate the effects of prevailing winds. Though epicenter determination from acoustic arrivals has errors associated with the fickleness of weather, resolution is still greatly superior to source location determination through the analysis of seismic waves. Emergent arrivals and phase velocities in excess of 1200 m/s (see figure 3.11) enable seismic source locations to be accurate to within only a few hundred meters.

Figure 3.9 (continued) Erebus 8-hour Acoustogram and Seismogram - c) Eight hours of activity recorded at station Krm1, day 251, 1999. Acoustic signals are recorded with McChesney microphone (top) and seismic signals are recorded with CMG-40T broadband seismometers (bottom). Wind noise appears as tremor throughout much of the acoustogram. Circles indicate events which are displayed in figure 3.13c.

Explosion origin times and the coincidence of seismo-acoustic source motions can be investigated in detail with the linear array of 7 seismo-acoustic stations deployed at Karymksy in 1998. Apparent acoustic velocities across the array for a suite of 30 explosions, range from 339 m/s to 353 m/s which could correspond to incidence angles ranging up to about 10 degrees or alternatively, temperature fluctuations ranging from 12 degrees to 36 degrees Celsius. Because this scatter in temperature is unrealistically large
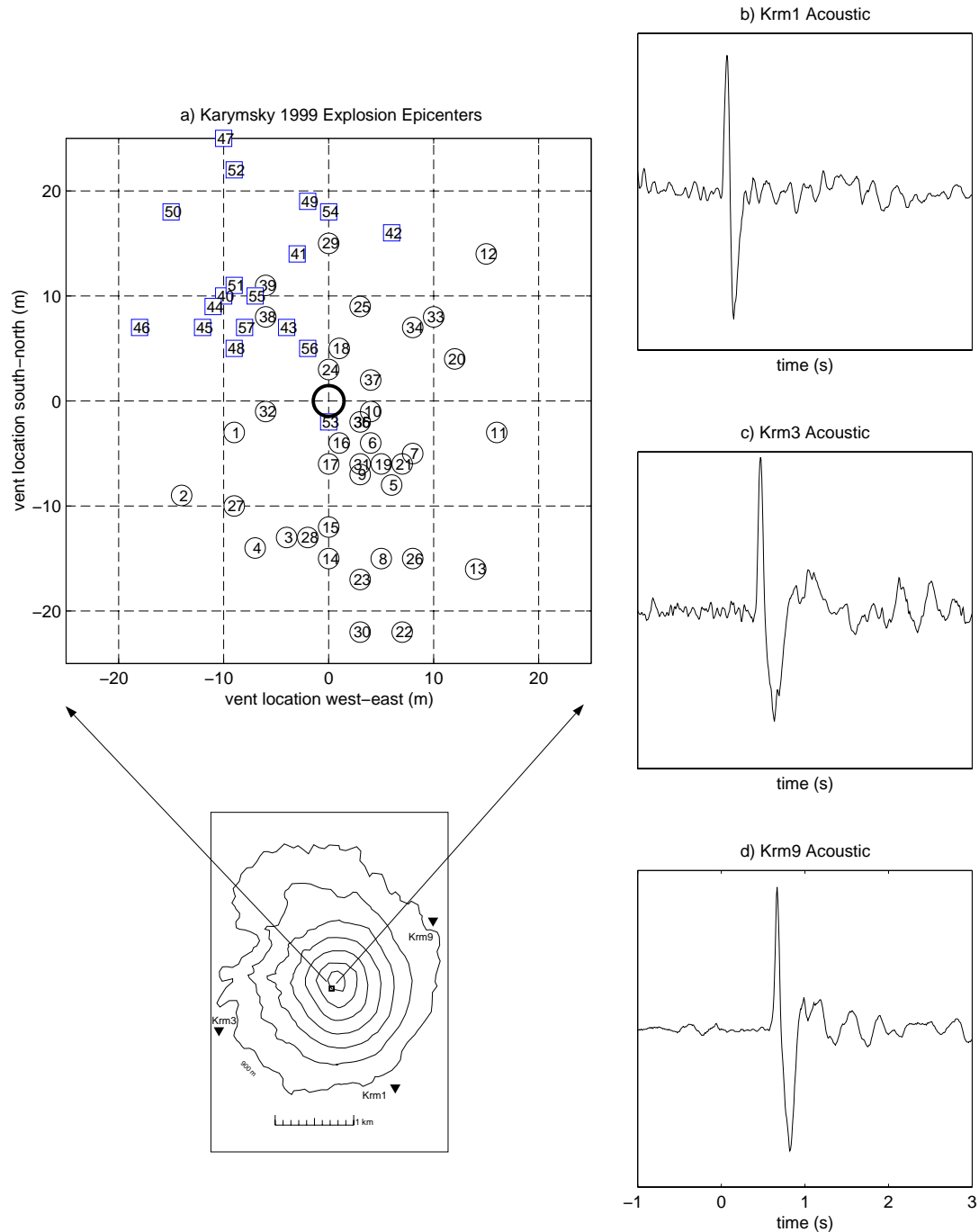
Figure 3.10 Karymsky Vent Locations - a) Calculated source locations for a suite of 57 explosions recorded between 1999:252:12:24 and 1999:255:19:25 determined by grid search assuming a homogeneous atmospheric velocity structure. Explosions are numbered chronologically and boxed events (40-57) are clustered temporally after 1999:254:19:59. Their spatial clustering indicates a prevailing wind out of the northwest. b-d) Sample explosion (event #55 - 1999:255:18:09) is shown as recorded at three azimuthally distributed stations.

during the periods of field work at Karymsky, it is more reasonable that incidence angles across the microphone array vary with changing atmospheric temperature and wind structure. A wind originating out of the northwest and blowing from the summit towards the radial array will bend acoustic raypaths downwards so that the apparent acoustic velocity is higher (refer to chapter 1, figure 1.6). Despite variations in acoustic propagation velocities, the linear array can be used to recover explosion origin times to within +/- 0.05 seconds.

As at Erebus, the time resolution of the explosion source determined by analysis of seismic traces is poor because of the emergent nature of the seismic waveforms. Even though station spacing is only 85 meters in the radial array (see figure 3.11), it is very difficult to identify coherent seismic energy crossing the array for unfiltered traces. Apparent seismic first arrival velocities can only be deduced from relatively low-frequency signals. For coherent 1 Hz energy, this apparent velocity is about 1200 m/s +/- 200 m/s. Using a 1200 m/s seismic velocity and a 346 m/s acoustic velocity, figure 3.11 displays inferred seismic and acoustic arrivals based upon a hypothetical synchronous seismo-acoustic source at the vent. For a concurrent explosion source, it is apparent from figure 3.11b that emergent seismic energy precedes the calculated seismic arrivals by about 1 second. The preliminary seismicity is low amplitude and could be attributed to either a concurrent seismo-acoustic explosion source that is located at depth within the conduit or precursory seismicity caused by rock failure or fluid movement just prior to an explosion [Johnson & Lees, 2000]. Precursory seismicity associated with the opening of a conduit prior to gas escape is reasonable if the explosion source originates beneath some sort of plug. In the discussion of Pichincha Volcano (see figures 3.27 and 3.28), large-amplitude precursory seismicity sometimes precedes the explosive release of gas by ten seconds or more.

Although some of the Karymsky explosion events consist primarily of a single impulse (similar to Erebus explosion events), many explosions have codas which last several
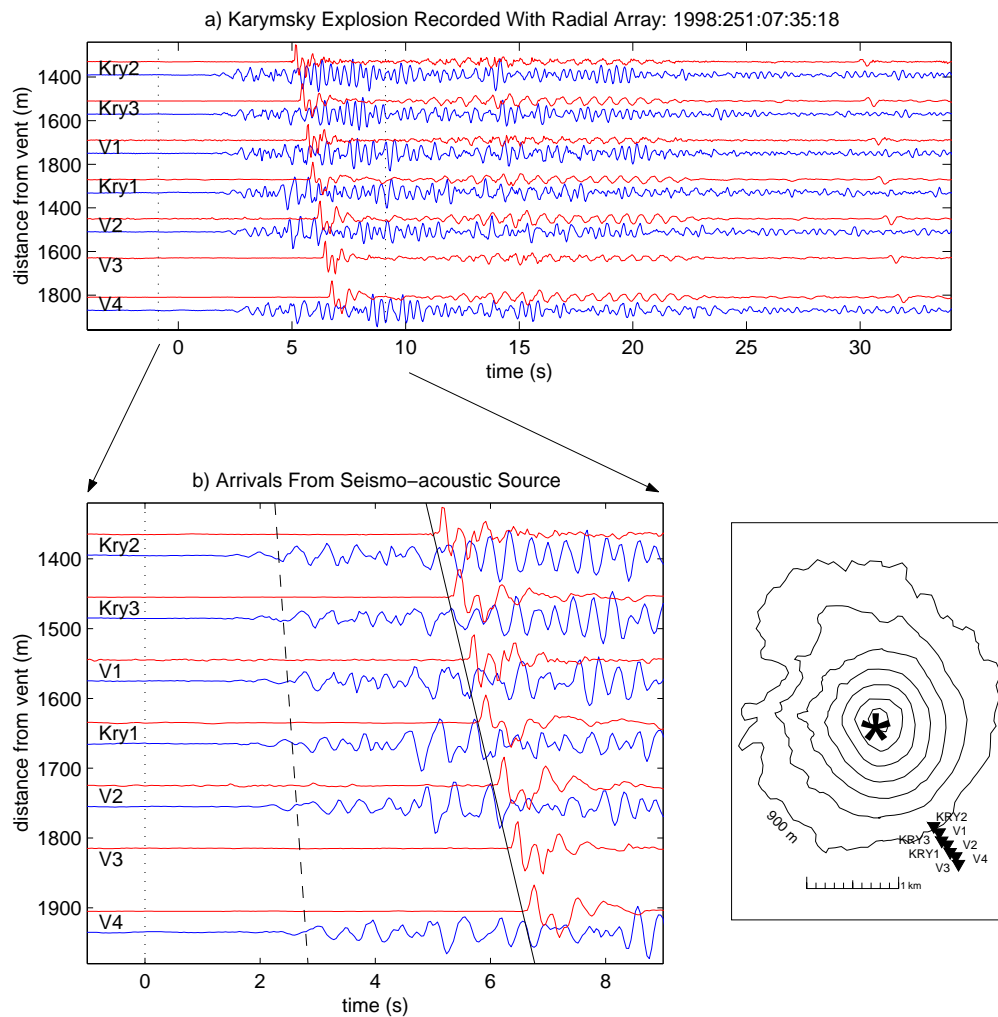
Figure 3.11 Karymsky Explosion Seismo-acoustic Arrivals - a) An explosion recorded on the linear array at Karymsky in 1998. Spacing between the 7 stations is 85 meters with a total length of 510 meters. b) Enlargement with marked arrivals shows acoustic arrival (solid line - apparent velocity 346 m/s) and inferred seismic arrival (dashed line - apparent velocity 1200 m/s). The seismic apparent velocity is determined through inspection of coherent 1 Hz energy (filtered signals not shown). Both acoustic and seismic arrivals are plotted assuming a synchronous seismo-acoustic source at an origin time of zero seconds. Seismic energy prior to the dashed line is an indicator of low-amplitude precursory seismicity.

minutes and indicate extended degassing. These longer-duration events have attributes which are similar in many ways to explosions recorded at Arenal [Hagerty et al., 2000] and Sangay [Johnson & Lees, 2000]. Karymsky explosion events can be grouped into several broad categories which include simple impulse events, high-frequency events, and chugging events [Johnson et al., 1998]. Simple impulse events (see figure 3.12a) are

manifested by a single impulsive short-duration damped acoustic oscillation (2 to 5 seconds long) and an associated brief seismic response (less than 20 seconds long). These seismic signals are the shortest signals associated with explosive gas release and are thus assumed to be the Green's Function response to an impulsive point source near the volcanic vent. Extended degassing events consist of high-frequency signals (figure 3.12b), harmonic tremor 'chugging' signals (figure 3.12c), or hybrid combinations. The high-frequency (or broad-band events) probably represent jetting of gases from the conduit into the atmosphere, whereas the chugging events are considered to be a regular sequence of gas bursts [Johnson & Lees, 2000].
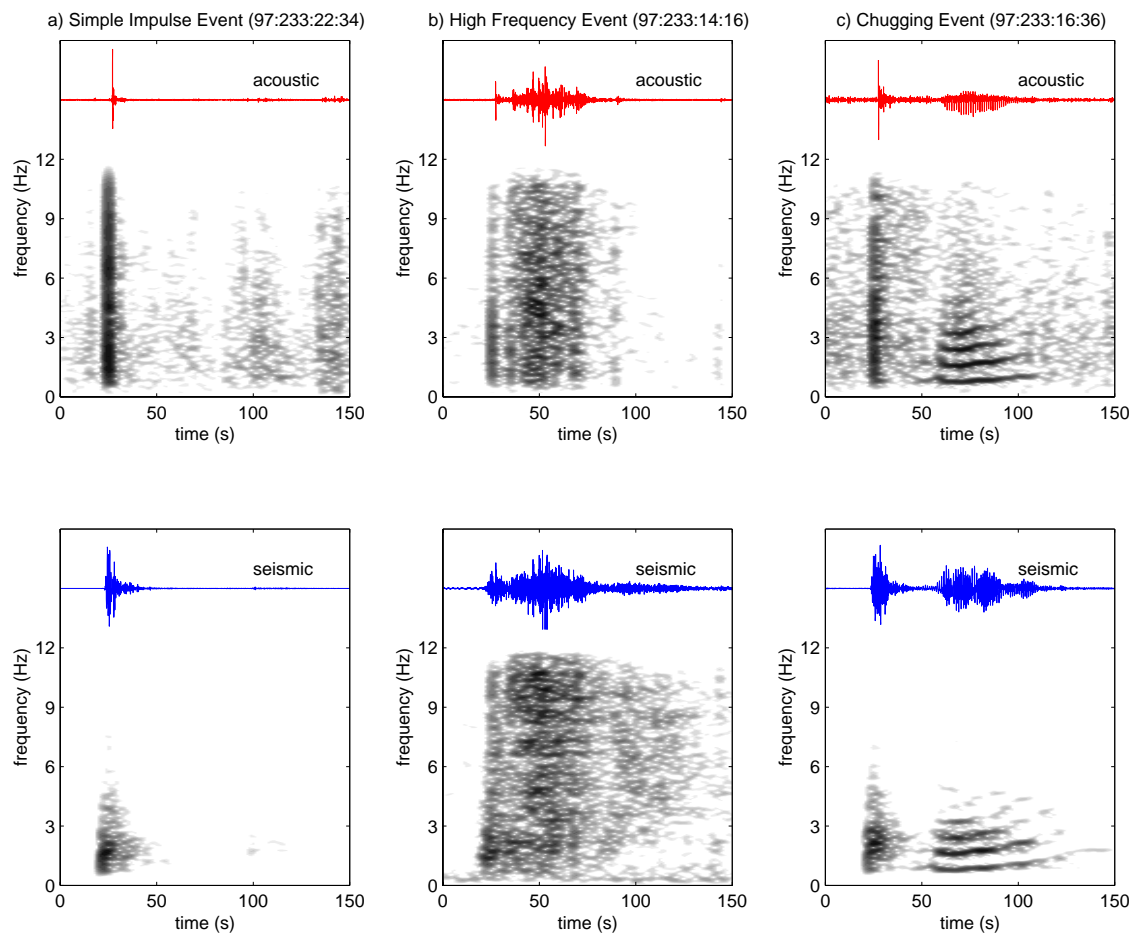
Figure 3.12 Karymsky Explosion Types - Acoustic pressure and seismic velocity traces and their spectrograms from typical types of explosions: a) simple impulse event, b) high-frequency event, and c) 'chugging' event. Spectrograms are calculated with 10 second windows at 2 second increments and are bandpassed between 4 seconds to 12.5 Hz.

Extended duration degassing events, including hybrid and chugging signals, are most common in the datasets collected in 1997 and 1999. It is likely that these extended degassing events reflect conduit conditions where the free flow of gas is impeded [Johnson & Lees, 2000]. During the 1998 field season, when explosion frequency was considerably higher than in 1997 or 1999, virtually all the events could be categorized as simple impulses. The 1998 field season is also associated with the highest magmatic flux as evidenced by the active block lava flow. A reasonable hypothesis is that during a more vigorous sequence of explosions, the conduit is continuously being cleared of material and explosions are able to degas entirely during a single impulsive burst. Visual observations from aerial overflights in 1997, 1998, and 1999 are consistent with the idea of a 'plugged' vent as rubble can clearly be observed choking the summit crater. Because the blocky andesitic lava is exsolved of volatiles at the surface, it may be viscous enough to prevent the upward percolation of gas. Instead gas must instead rise together with magma find its exit through fissures and cracks near the surface.

The primary source of radiated seismic energy is the thrust force induced by the rapid mass outflux from the volcanic conduit. However, the exact depth, extent, and first motions of the seismic source-time function is not well known. The emergent nature of the seismic signal may be due to gradually increasing source motions or may result from propagation effects. Several authors, including Neuberg et al. (2000), suggest that emergent, extended-duration seismic signals can be explained by sources in a low-impedance conduit radiating energy into the high-impedance wall rock.

Of the three datasets collected at Karymsky Volcano, the seismic explosion onsets from 1997 are the most self-similar (refer to overlays in figure 3.13a-c). Though the seismic codas are widely variable (ranging from non-existent to several minutes of chugging), the first 10 seconds of all seismic signals appear to have a very high degree of correlation. It is thus easy to believe that initial seismic source motions and locations are fairly consistent. However, in 1998 and 1999, seismic explosion onsets were not nearly as
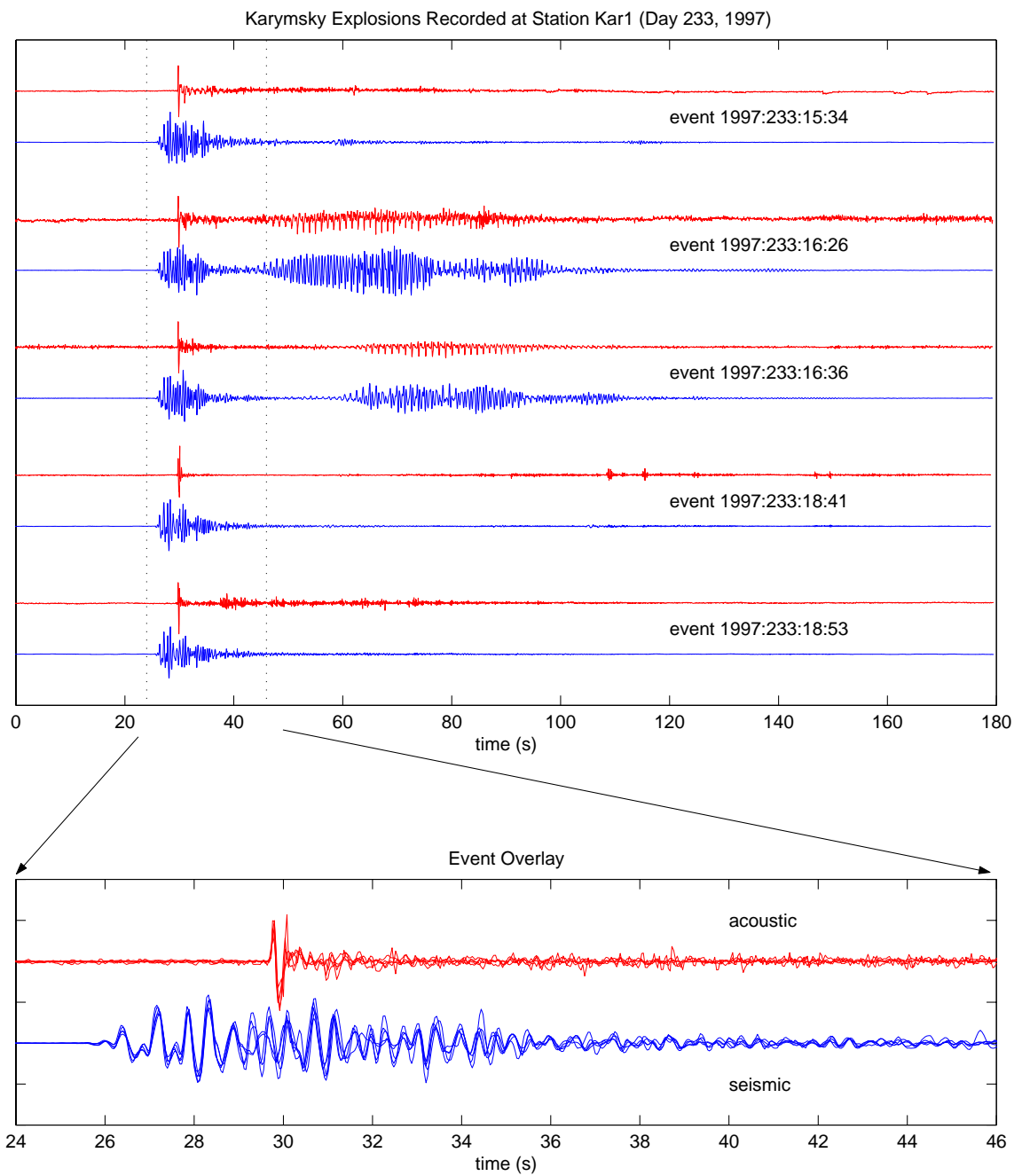
Figure 3.13 Karymsky Explosion Examples - a) Selected 1997 normalized explosion waveforms from figure 3.9a (top) and overlay of waveforms (bottom).
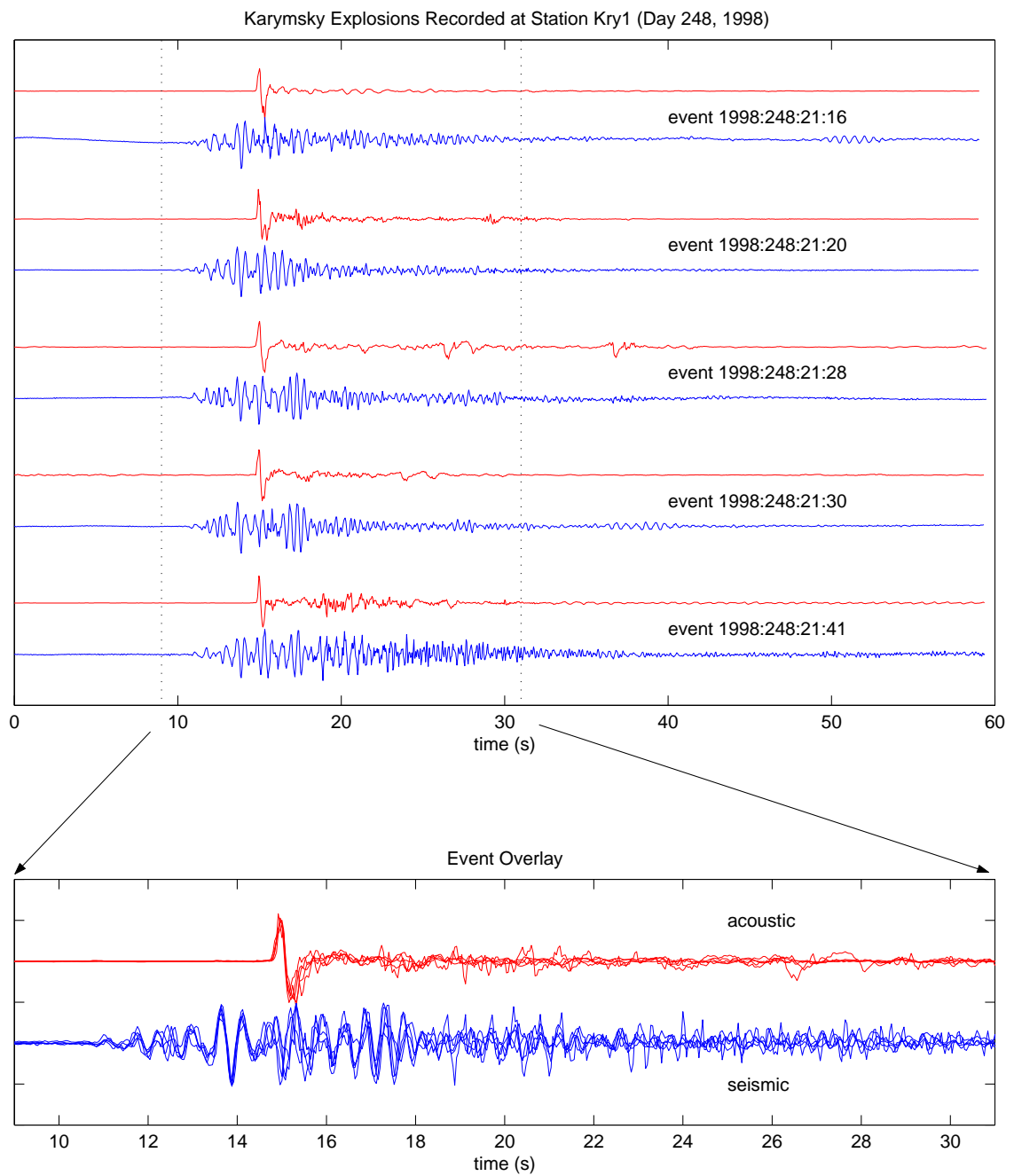
Figure 3.13 (continued) Karymsky Explosion Examples - b) Selected 1998 normalized explosion waveforms from figure 3.9b (top) and overlay of waveforms (bottom).
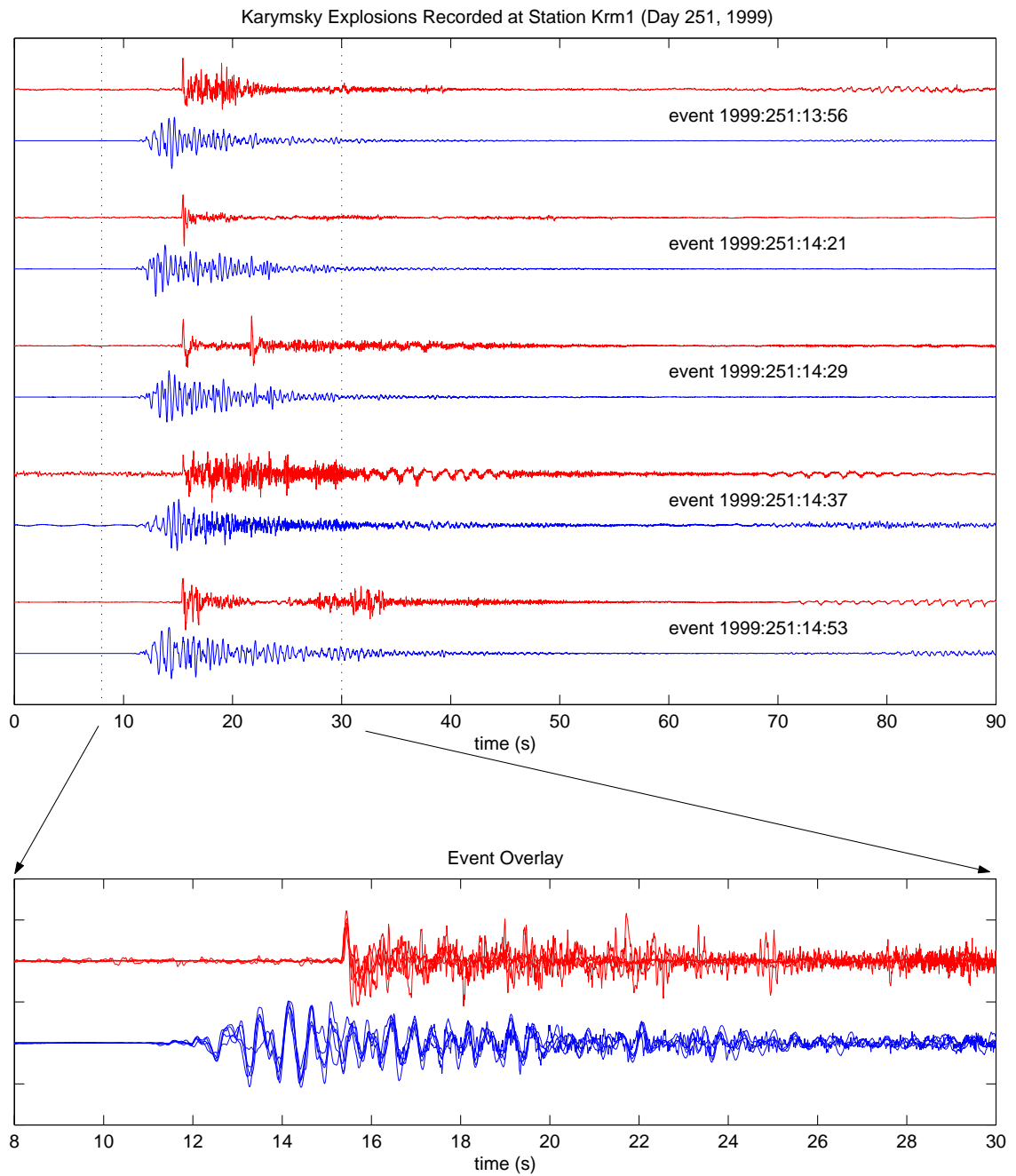
Figure 3.13 (continued) Karymsky Explosion Examples - c) Selected 1999 normalized explosion waveforms from figure 3.9c (top) and overlay of the waveforms (bottom).

repetitive. It remains to be determined whether the differences in recorded seismic onsets are due to variable source locations or due to variable source motions. Vertical differences in source locations on the order of tens of meters may be sufficient to account for the lack of seismic self-similarity in 1998 and 1999. Unfortunately, unless microphones are placed closer to the vent, variable source locations within the conduit are beyond the resolution afforded by the current acoustic arrays (about 20 meters for the 1999 microphone arrays). Experiments with closely-spaced seismic stations, such as the 1998 linear array, demonstrate that recorded seismic signals have extremely poor semblance at neighboring stations (station spacing of 85 meters). By reciprocity, it could take far less than 85 meters of source location variability to account for the variability in the observed seismic onsets in 1998 and 1999.

3.4.3 Utility of Acoustic Monitoring

The most immediate benefit of acoustic monitoring at Karymsky is the observation that complicated seismic signals, such as harmonic tremor 'chugging' events are reflected in the acoustic channels. Prior to acoustic monitoring at volcanoes such as Karymsky, seismic waveforms appeared too afflicted by complicated ground propagation filters to satisfactorily recover source locations or mechanisms. Infrasonic monitoring at Karymksy has demonstrated that these seismic signals are associated with emission of gas at the vent. The dramatic and rapid expansion of compressed gas at the free surface is the most likely mechanism for the common seismo-acoustic source, including extended-duration seismo-acoustic codas. The bulk of the seismic energy is a heavily filtered response to gas expansion thrust forces at the vent. Low-amplitude precursory seismicity may reflect processes that are not associated with gas release.

Another important result from the experiments at Karymsky is the observation that different types of explosion events tend to cluster in time. Karymsky explosions are an assortment of simple impulse, high-frequency, and harmonic tremor events. There is good evidence that successive explosions tend to consist of the same event type (see
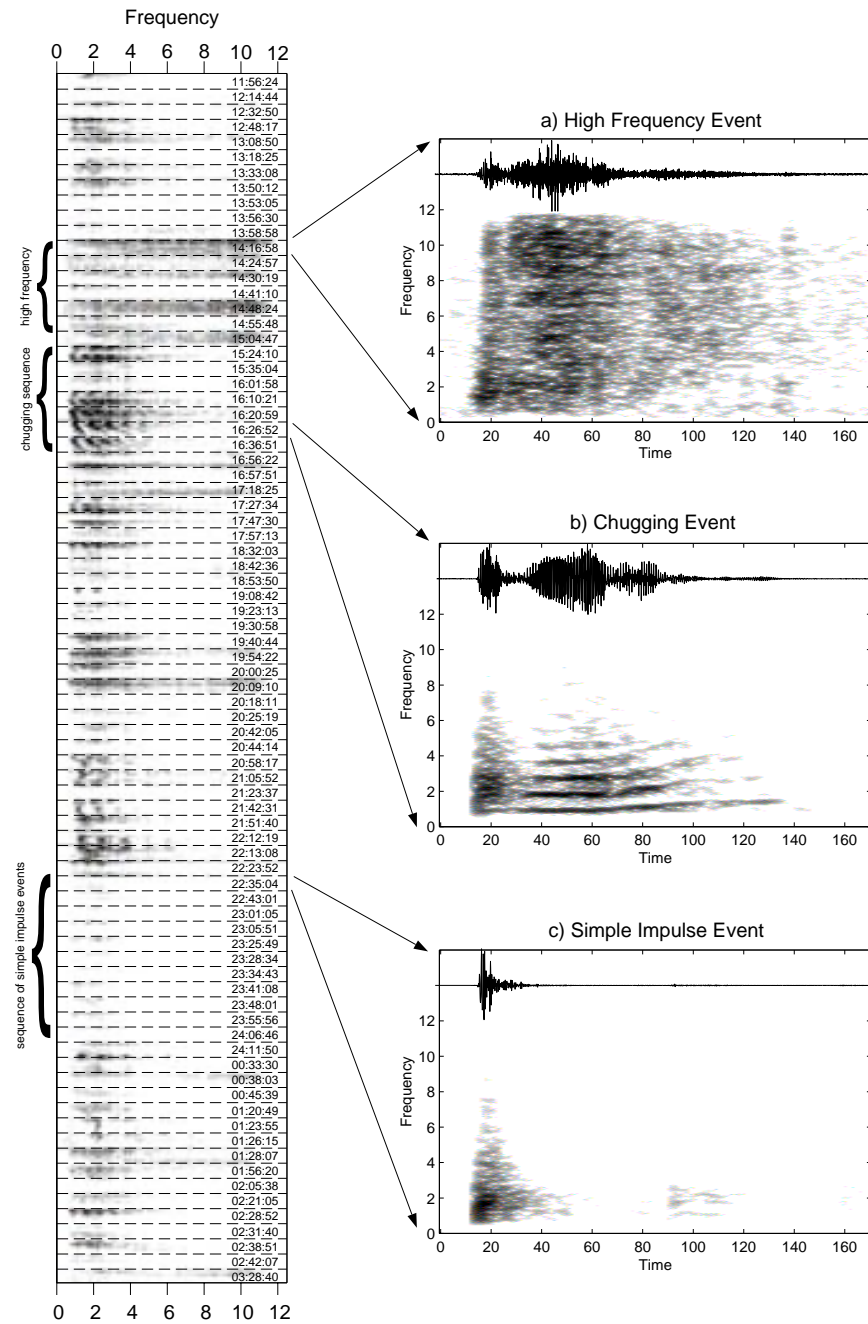
Figure 3.14 Evolution of Karymsky Event Types - Seismic traces and associated spectrograms for three characteristic event types at Karymksy in 1997: a) high-frequency event, b) chugging (harmonic tremor) event, c) simple impulse event. The spectral evolution plot demonstrates how specific event types tend to cluster in time for the Karymsky 1997 record. Spectrograms are calculated for 80 consecutive events using time windows 30 to 90 seconds after the explosion onset. Figure from Johnson & Lees (2000).

figure 3.14). Variable conduit dimensions, fragmentation depth, and/or plug characteristics may contribute to the varied signals produced at Karymsky [Johnson & Lees, 2000]. These parameters may remain consistent over the course of several explosions because the material choking the upper portion of the Karymsky conduit is degassed andesite with a considerable higher viscosity than the Erebus magma [Sparks, 1997]. Unlike Erebus Volcano, where all explosions consist of identical simple impulse explosions corresponding to bubble rupture directly at the free surface, Karymsky events types are variable and cluster temporally suggesting that conditions in the conduit evolve over the course of many explosions.

3.5 Sangay:

3.5.1 Background

Sangay Volcano (see figure 3.15) is located in Ecuador's eastern cordillera and is at the southern terminus of the active volcanoes of the Northern Andes. It has been continuously active at least since 1628, when it was first observed by Europeans [Hall, 1977]. Typical Sangay eruptive activity ranges from vigorous explosions with mass ejecta, dome growth, and pyroclastic flows, to less violent explosions with a predominance of gas release. However, due to its isolated position in the cloud-shrouded eastern cordillera of Ecuador, fluctuations in activity can go largely unnoticed. The 5300 meter stratovolcano has an edifice height of more than 1800 meters and a complex summit with four craters aligned along a 700 meter ridge [Monzier et al., 1999]. During the April, 1998 field season, eruptive activity was at a relative ebb, with discrete Strombolian-type explosions emanating from a single vent approximately 2 times each hour. Some ejecta and the observation of incandescence hinted at a slight, though continuing flux of solid material through the vent. Though the chemical composition of Sangay's volcanic products is somewhat variable, the bulk of recent lavas lie between 55 and 57 weight percent silica, classifying current erupted products primarily as andesite [Monzier et al., 1999]. The viscosity of the degassed erupting magma may be comparable to the magma emerging from Karymsky during 1997 to 1999 [Sparks, 1997].

Figure 3.15 Photo of Sangay - Picture of Sangay taken in 1996 with windblown eruption plume. Photo courtesy of P. Hall.

Sangay explosions were recorded with acoustic and seismic instruments for a 5 day period in April of 1998. A single Venema microphone was co-located with a CMG 40-T seismometer 2200 meters from the active vent at station San1 (see figure 3.16). Data acquisition was continuous at 125 samples per second using a Reftek datalogger. This experiment was the first to digitally record Sangay volcanic earthquakes with seismic or acoustic sensors.

3.5.2 Data Overview

Acoustic noise was problematic during the study at Sangay because of persistent high winds at the recording site and the relative infrequence of explosions (see figure 3.17). As a result, the Sangay data contains only about 50 events of good acoustic quality corresponding to about 40 percent of all the explosions (identified through the seismic channel). Unlike Karymsky seismicity, it is possible that some of the seismic events are not associated with surface degassing (see tremor signals selected by boxes in figure 3.17 for possible candidates). However it is impossible to determine definitively if these sources are truly internal owing to relatively high background acoustic noise.
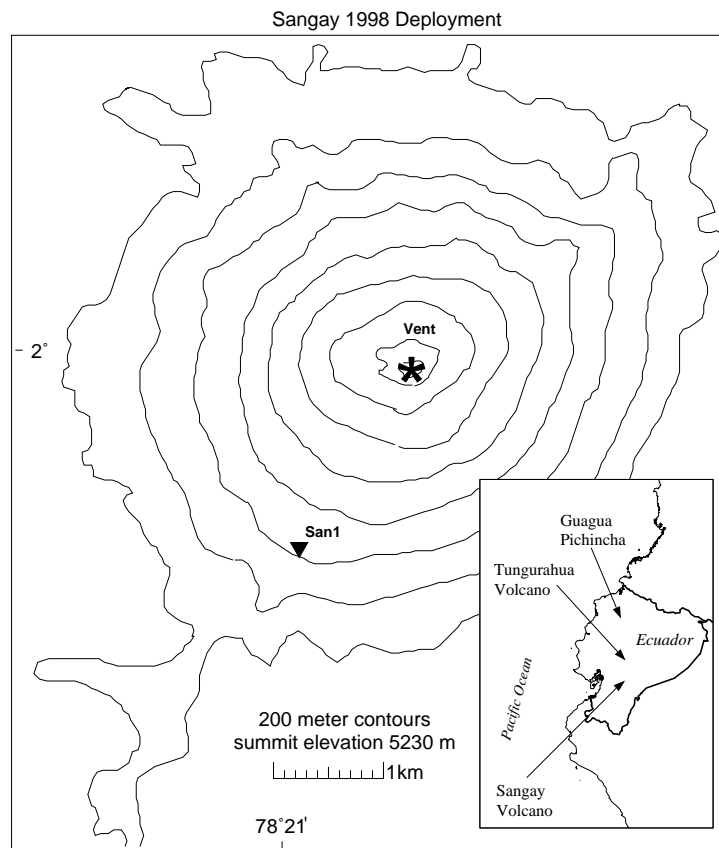
Figure 3.16 Sangay Station Map

Figure 3.16 Sangay Station Map - Sangay 1998 deployment map. Station San1, located 2200 meters from the active vent, contained both a seismometer and microphone.

Sangay explosion events, like Karymsky explosion events, are characterized by a fixed travel time difference between seismic and acoustic phases. For reasonable sound speed velocities (330 m/s), a concurrent seismo-acoustic source implies seismic P-wave arrivals of 1600 m/s +/- 200 m/s. This range of velocities is approximate because of the emergent nature of the seismic signals and the assumption that seismic and acoustic signals have the same origin time. Despite their emergent nature, the onsets of the seismic waveforms are generally self-similar (see overlays in figure 3.18) indicating repeatable source locations and motions for the very beginning of explosive degassing. Acoustic signals from Sangay, like the acoustic signals from Karymsky, are impulsive, making it very easy to identify arrival times.
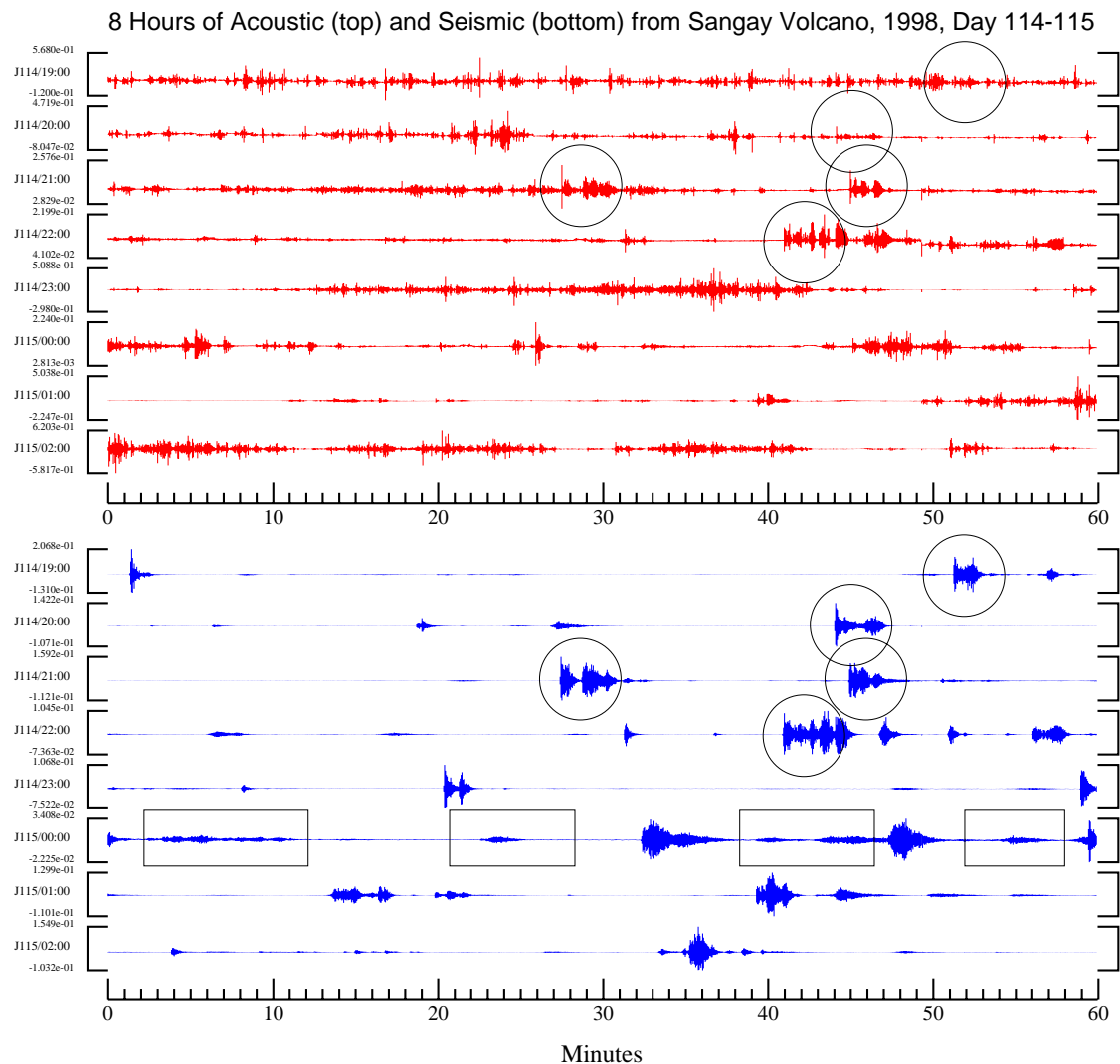
Figure 3.17 Sangay 8-hour Acoustogram and Seismogram - Eight hours of activity recorded at station San1, day 114-115, 1998. Acoustic signals are recorded with a Venema microphone (top) and seismic signals are recorded with a CMG-40T broadband seismometers (bottom). Circled events are displayed in figure 3.18. Boxed events are seismic tremor signals without obvious acoustic counterparts.

The primary difference between Sangay and Karymsky explosion signals is that virtually all explosions recorded at Sangay possess an extended coda. In many explosions, spectacular harmonic tremor 'chugging' events last as long as 5 minutes with 'gliding' of the fundamental frequency between 0.4 and 1.5 Hz (see figure 3.19). These seismo-acoustic 'chugging' events are remarkably similar in appearance to the 'chugging' events
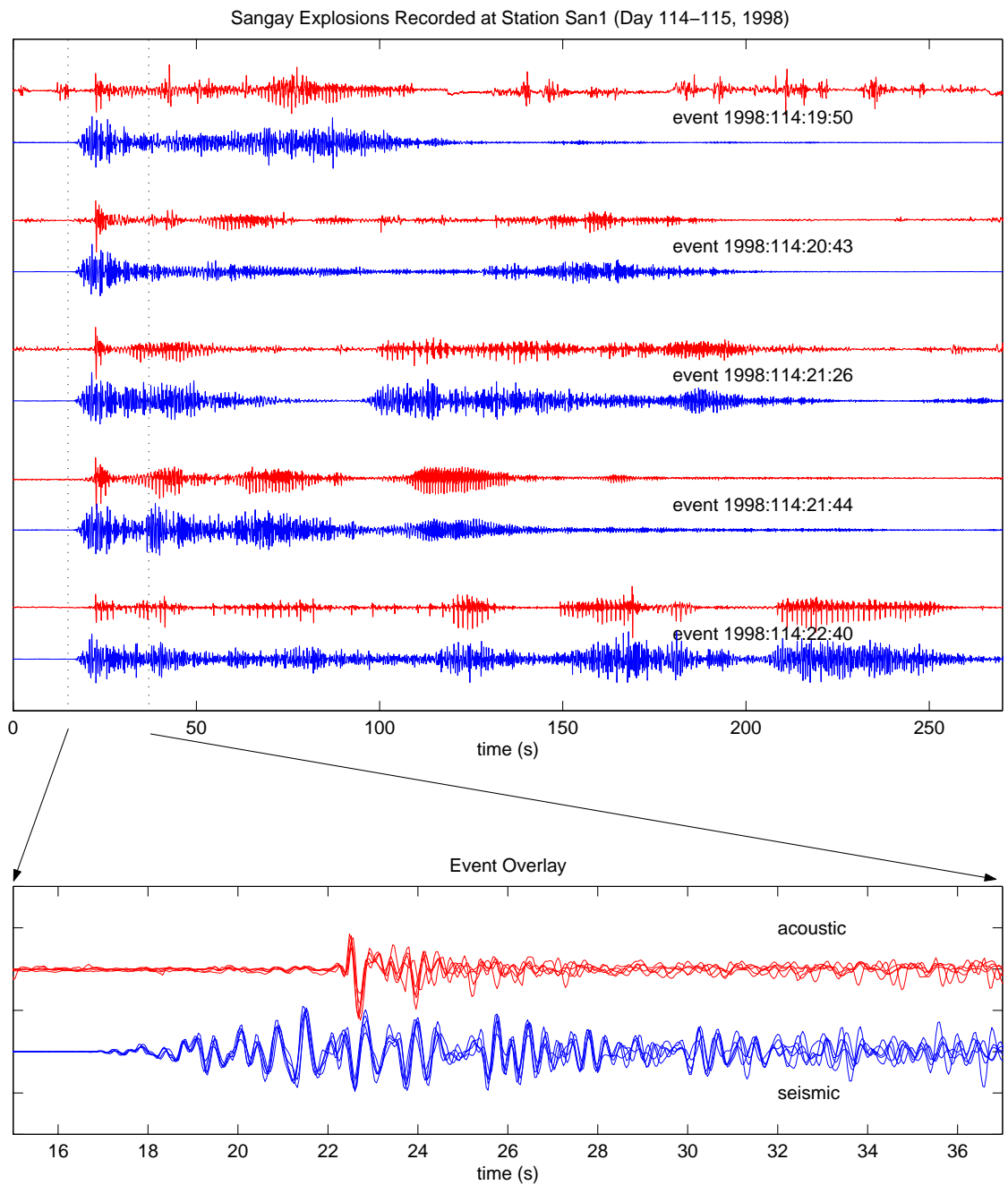
Figure 3.18 Sangay Explosion Examples - Selected normalized explosion waveforms from figure 3.17 (indicated by circles). An overlay of the five events is shown at bottom.

at Karymsky recorded in 1997 and it is likely that the degassing mechanism is very similar. During the 1998 Sangay field season a relatively low magma flux and infrequent explosions suggest that a high-viscosity plug of rubble had time to form in the throat of the volcano. This plug lent itself to the near omnipresence of 'chugging' events [Johnson & Lees, 2000].
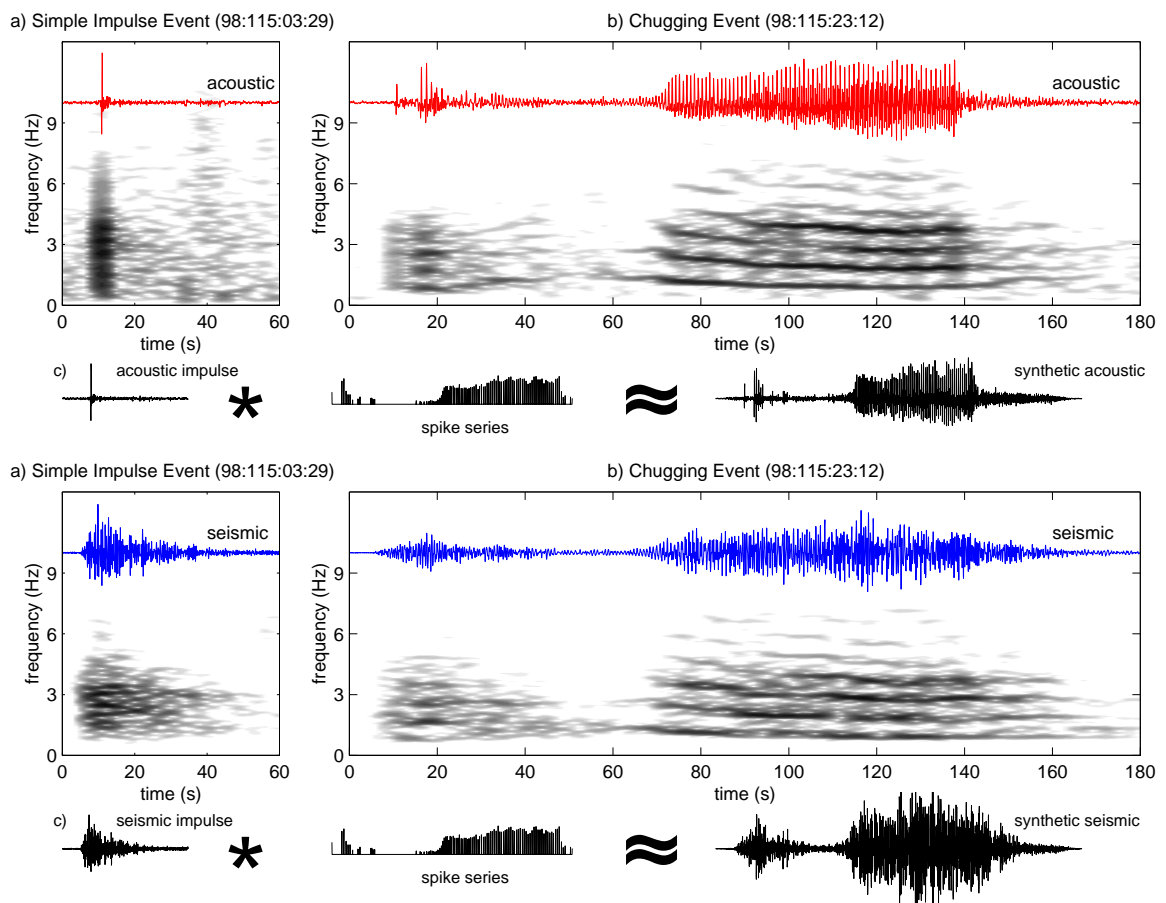

Figure 3.19 Sangay Simple Impulse and Chugging Event - Example traces and spectrograms of: a) rare Sangay simple impulse event and b) common Sangay 'chugging' event. Both traces are bandpassed between 4 seconds and 12.5 Hz and associated spectrograms are calculated with a 10 second window at 2 second increments. The fundamental frequency in the spectrograms correspond to the time interval between individual acoustic chugs. c) Sangay chugging events can be thought of as a series of gas releases or a convolution of a simple impulse event with a spike series corresponding to a sequence of 'chugs'.

116

3.53 Utility of Acoustic Monitoring

The physical conditions which are responsible for the 'chugging' phenomena at Sangay and Karymsky may be replicated at a host of other volcanoes where chugging has been observed: Arenal, Costa Rica [Benoit & McNutt, 1997], Semeru, Indonesia [Schlindwein et al., 1995], Langila, Papua New Guinea [Mori et al., 1989], and Ambrym, Vanuatu [Phil Kyle, personal communication, 1999]. Because chugging is evident in both acoustic and seismic channels and is associated with visible degassing, it provides an opportunity to understand source mechanisms for this distinct type of volcanic harmonic tremor. The periodicity of the pulses, which range from 0.5 Hz at Sangay to 1.5 Hz at Karymsky, is regular enough to produce integer overtones in the frequency spectra (see figure 3.19). Explanations for the regularity of the explosion signals include: resonating fluid bodies [Benoit & McNutt, 1996; Schlindwein et al., 1995; Garces & McNutt, 1997], Von-Karmon vortice shedding [Hellweg, 2000], and choked flow through a pipe [Julian, 1994; Lees & Bolton, 1998]. A choked-flow model appears to be a reasonable explanation for Karymsky and Sangay 'chugging', where gas may be escaping through cracks or narrow conduits in a viscous, blocky lava, in order to vent at the surface.

3.6 Tungurahua:
3.61 Background

Tungurahua Volcano is a large stratovolcano with 3000 meters of local vertical relief. It is located in Ecuador's eastern cordillera about 60 km north of Sangay. Prior to the current period of activity, Tungurahua was most recently active between 1916 and 1918, producing Strombolian explosions, andesitic lava flows (55-58 weight percent silica), and a few pyroclastic flows towards the end of the eruptions in 1918 [Hall et al., 1999]. Heightened seismicity associated with renewed Tungurahua activity was first observed in mid-September, 1999, about a month prior to the eruption onset. Continuous tremor steadily increased in amplitude until magma first breached the surface, on October 5, 1999 [Mario Ruiz, personal communication, 1999]. Initial activity was characterized by periods of Vulcanian volcanism (see figure 3.20) with convective plumes rising more

than 5 km above the vent, ash fall to the north and northwest of the volcano, and small lahars. Since 1999, eruptive vigor has gradually decreased and as of October, 2000, activity consists of sporadic Strombolian explosions [Mario Ruiz, personal communication, 2000].

Figure 3.20 Photo of Tungurahua - Open shutter nighttime image (~1 minute exposure) of incandescent material emitted from Tungurahua. Photo taken November 2, 1999 by A. Calahorrano.

A McChesney 4-element electret condenser microphone was deployed as a monitoring tool on October 23, 1999 to assess the quantity and relative magnitudes of Tungurahua explosions. The microphone was co-located with a temporary short-period seismometer 9 kilometers from the volcano vent (see figure 3.21). Seismo-acoustic data was recorded continuously at 50 samples per second on a Reftek datalogger. Data displayed in this section comes from a 4-day period when activity was manifested by an almost continuous series of explosions, including emissions of gas and ash columns several kilometers high and the ejection of large incandescent blocks.
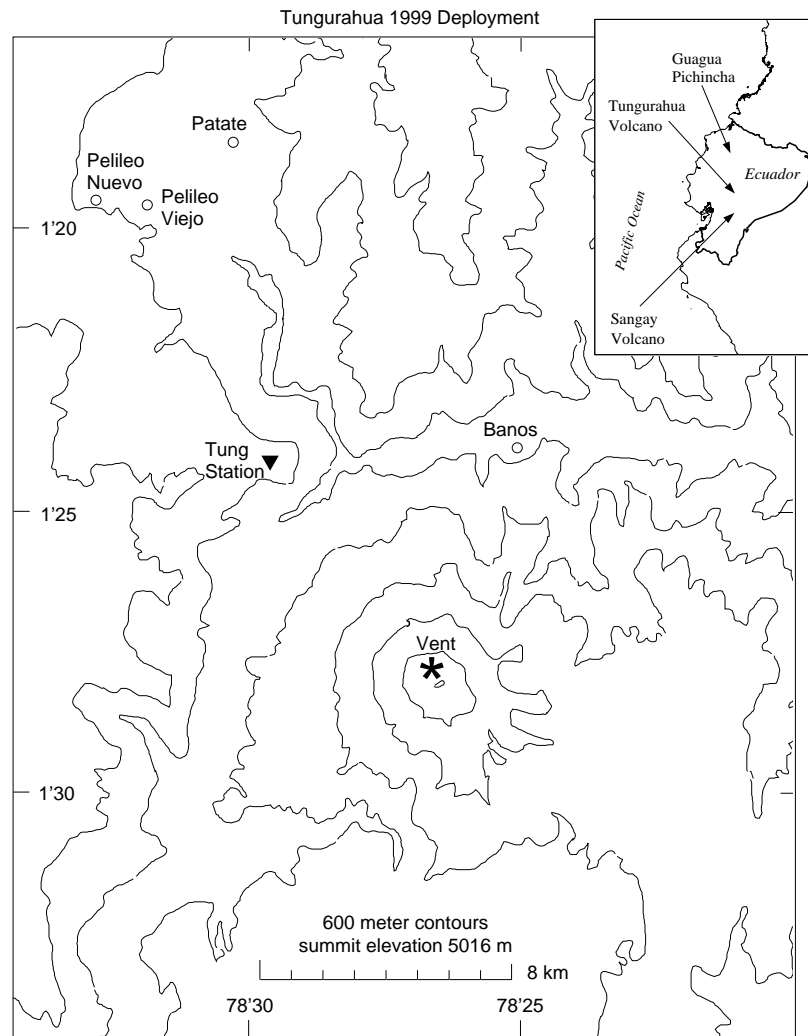
Figure 3.21 Tungurahua Station Map - The temporary station Tung, deployed in October, 1998, contained a short-period seismometer and a 4-element McChesney-type microphone.

3.6.2 Data Overview

The incentive for the deployment of a low-frequency microphone at Tungurahua was to remotely assess the eruptive vigor and frequency of explosions from the volcano. Acoustic monitoring proved particularly beneficial at Tungurahua because seismic channels were plagued by a large amount of volcanic tremor even prior to the commencement of the eruption in 1999. Pre-eruptive seismic tremor was thought to be

related to an active hydrothermal system at Tungurahua because increased seasonal tremor amplitude was positively correlated with periods of heavy rain [Ruiz et al., 1997]. In the weeks preceding and during the eruptions of October, 1999, tremor amplitude increased and was intense enough to saturate short-period stations 5 km from the vent. Up through the end of October, this tremor was energetic enough to effectively obscure seismic signals associated with discrete explosion events (see figure 3.22). Since discrete explosions were identifiable both audibly and visually, a low-frequency acoustic microphone was employed as a supplementary monitoring tool. Despite the distant station location (9 km from the vent), the microphone was successful at identifying a suite of different acoustic signal types during periods of low wind (late afternoon to mid-morning).

During periods of low wind, impulsive acoustic bursts and higher-frequency acoustic tremor (refer to top panel in figure 3.22) are evident almost continuously and correspond to visual observations of gas and ballistic emissions. In this respect, Tungurahua activity differs from the discrete explosions observed at Erebus, Karymsky, and Sangay Volcanoes. Occasionally acoustic impulses are preceded by a couple of minutes of relative quiet (see figure 3.23), but for the most part, acoustic tremor is always present. In general, acoustic signals have only very poor correlation with seismic signals at Tungurahua because of the high-amplitude broad-band seismic background tremor. In only a few instances, when background seismic tremor is relatively low, packets of seismic energy can be associated with acoustic explosion signals (see figure 3.24). If seismic traces were not corrupted by such high noise, their onsets should precede acoustic pulses by approximately 25 seconds for a common seismo-acoustic explosion source at the vent applying reasonable seismic and acoustic propagation velocities.

Because of the relatively lengthy propagation distances between the vent and station Tung, higher acoustic frequencies are attenuated, and the bulk of the recorded acoustic energy lies below 5 Hz (refer to figure 3.24). An additional deficit of acoustic signal
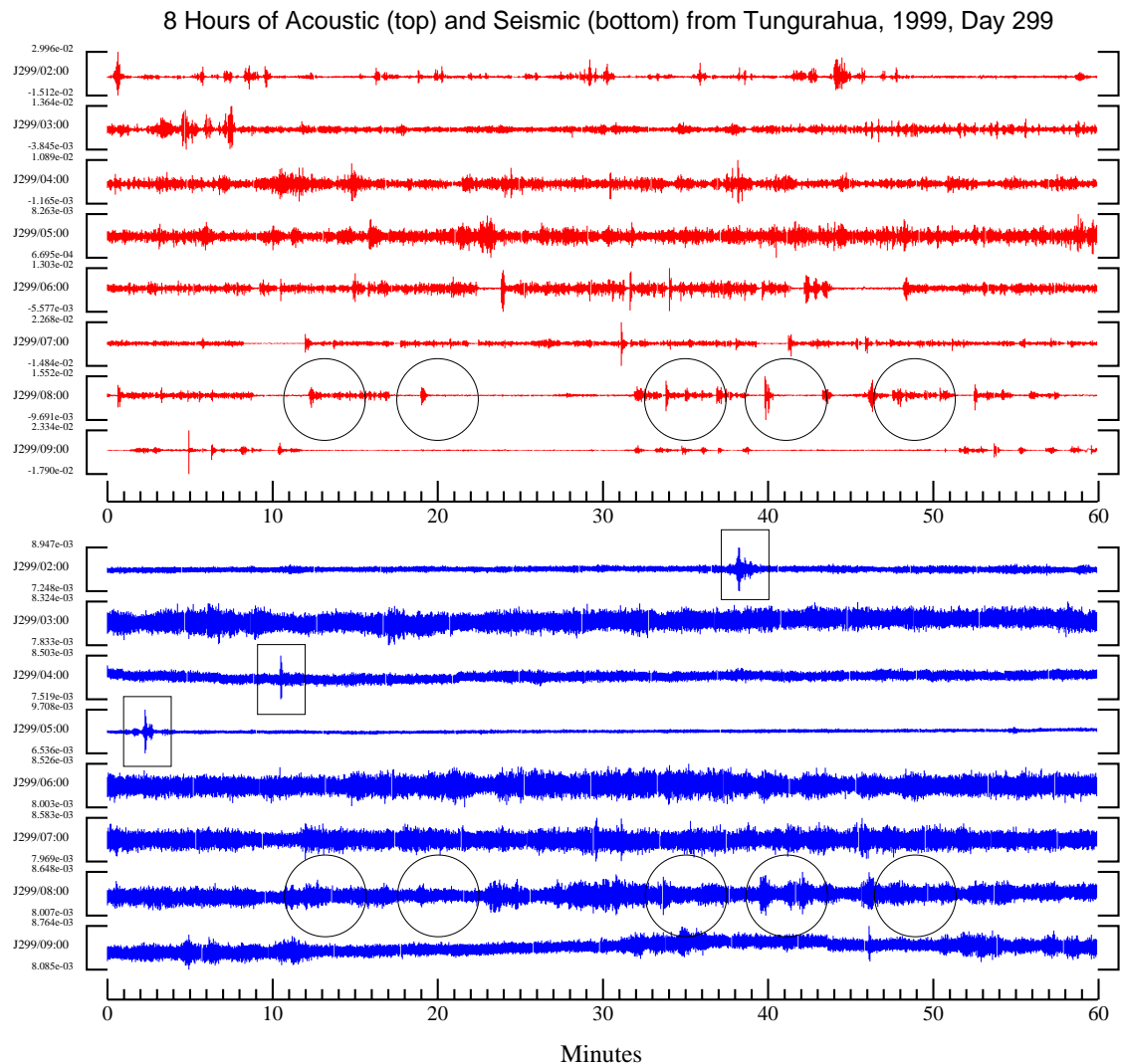
Figure 3.22 Tungurahua 8-hour Acoustogram and Seismogram - Eight hours of activity recorded at station Tung, day 299, 1999. Acoustic signals are recorded with a 4-element McChesney-type microphone (top) and seismic signals are recorded with a Mark Products short-period seismometer (bottom). Acoustic traces reflect degassing sources and have very low wind noise. The high-amplitude seismic tremor is noise that is not associated with degassing. Higher amplitude discrete events (indicated by boxes) are regional earthquakes. Circled events corresponding to discrete eruptions are displayed in greater resolution in figure 3.23.

which occurs at about 3 Hz is not observed in the infrasonic records from other volcanoes and may be unique property of the Tungurahua eruption source. This unique double-peaked acoustic frequency spectra at Tungurahua serves as an effective diagnostic for distinguishing between degassing signal and wind noise. Though wind noise at
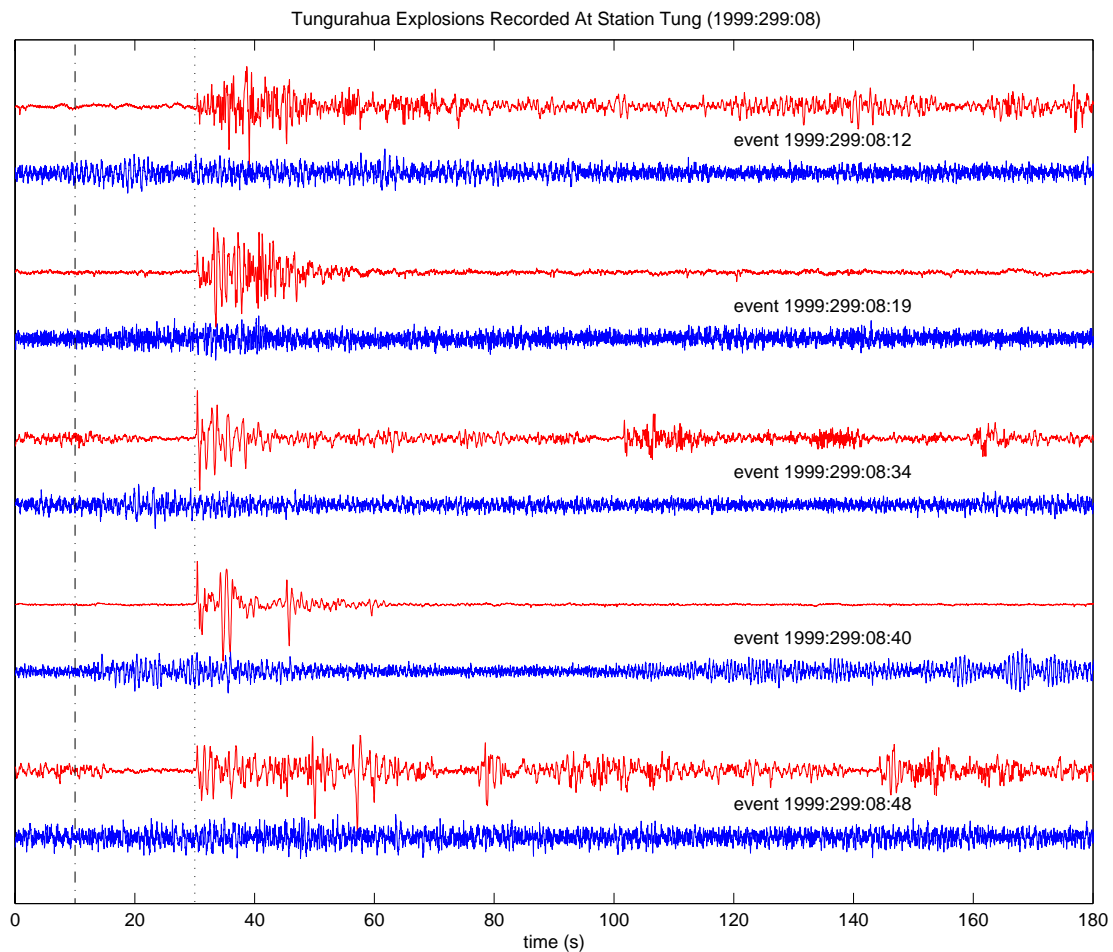
Figure 3.23 Tungurahua Explosion Examples - Selected normalized acoustic (top trace) and seismic (bottom trace) waveforms from figure 3.22 (indicated by circles).

Tungurahua is often severe enough to completely obscure eruption signals, the wind spectra is broad-band and contrasts dramatically with the double-peaked spectra associated with gas emission.

3.6.3 Utility of Acoustic Monitoring

In periods of low wind, the microphone deployed at Tungurahua served as a very effective tool for observing when degassing was occurring. Frequent inclement weather, a large inaccessible zone around the volcano, and noisy seismic data made verification of gas and material flux from the vent difficult to monitor without infrasonic observations.
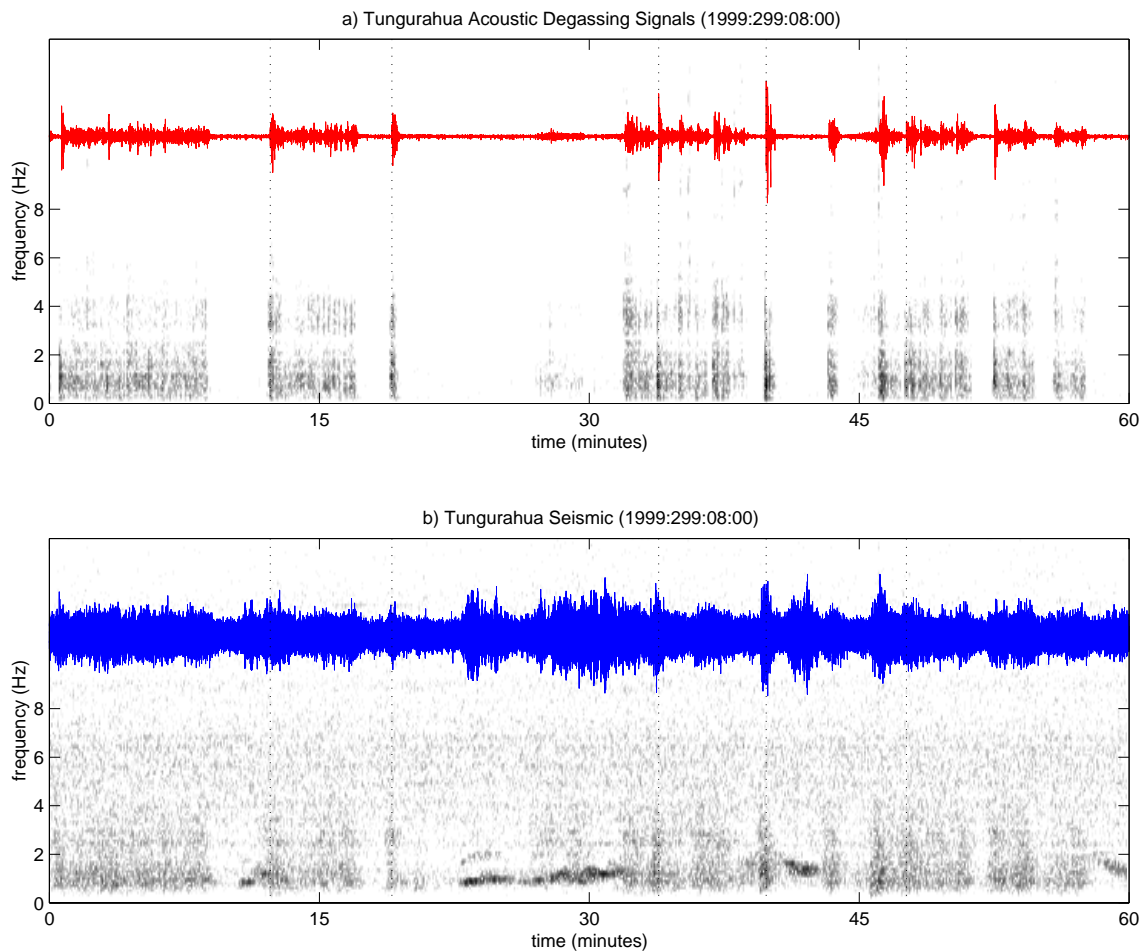
Figure 3.24 Tungurahua Spectrogram - Seismic and acoustic traces with associated spectrograms for one hour of degassing activity at Tungurahua Volcano. a) The acoustic trace shows a combination of impulses and continuous tremor with a characteristic double-peaked frequency spectra. b) The seismic trace envelope has only a slight correlation with the acoustic trace envelope (most evident in the accompanying spectrograms).

The signals recorded at Tungurahua indicate a continuous style of degassing, consisting of both explosive pulses and quasi-continuous 'jetting'. The Tungurahua activity from October, 1999 is somewhat more vigorous than the Strombolian activity recorded at Erebus, Karymsky, or Sangay. Though magma viscosity is similar at Tungurahua, Karymsky, and Sangay, enhanced gas and magma flux at Tungurahua probably accounts for the heightened eruptive vigor.

As a scientific tool, the microphone deployed at Tungurahua had several shortcomings. The distant location of the acoustic pressure sensor made absolute pressure measurements inexact due to the vagaries of acoustic transmission through 9 km of atmosphere. Thus relative acoustic amplitudes are likely to be extremely dependent upon variations in atmospheric temperature and wind structure throughout the day (see chapter 1). Finally, a lack of clean seismic records and visual observations is a hindrance to the analysis of Tungurahua infrasonic signals. In the future, a seismo-acoustic study could benefit from better visual observations, multiple microphones, and closer proximity of the microphones to the vent.

3.7 Guagua Pichincha:

3.7.1 Background

Guagua Pichincha is a stratovolcano with a horseshoe-shaped caldera 1.5 km wide and an active dacite dome. The last significant eruption of Pichincha occurred in 1660 and is associated with the deposit of several centimeters of ash on Quito, 12 kilometers to the east [Hall, 1977]. In recent decades, up until the onset of the volcanic crisis in 1998, activity at Pichincha was manifested by active fumaroles from the dome and infrequent phreatic explosions (several each year). In 1998 a volcanic crisis was declared because of a dramatic increase in phreatic explosions (several each week) and the presence of long-period earthquakes. A transition to phreato-magmatic explosive activity occurred during the summer of 1999 at about the same time that dome growth was noted [Mario Ruiz, personal communication, 1999]. On October 7th, 1999, possible dome collapse initiated a spectacular convective plume rising five kilometers and clearly visible from Quito (see figure 3.25). This event was responsible for the demise of a microphone station located 600 meters from the vent.

Acoustic monitoring at Pichincha initiated in November, 1998 and continued up until October, 1999. The first instrument installed was a single electret condenser Venema microphone that was co-located with a short-period single-component network
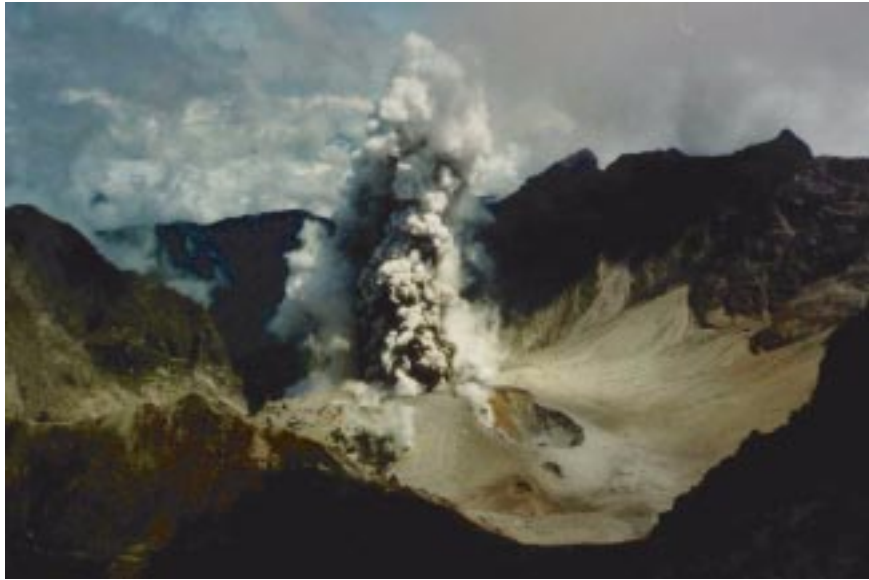
Figure 3.25 Photos of Pichincha - a) August 2, 1999 explosions from dome as seen from near the summit of Pichincha. Photo courtesy of F. Rivadeneira.

Figure 3.25 (continued) Photos of Pichincha - b) View from Quito of October 7th, 1999 convective plume rise associated with a possible partial dome collapse. Photo taken by M. Quito.
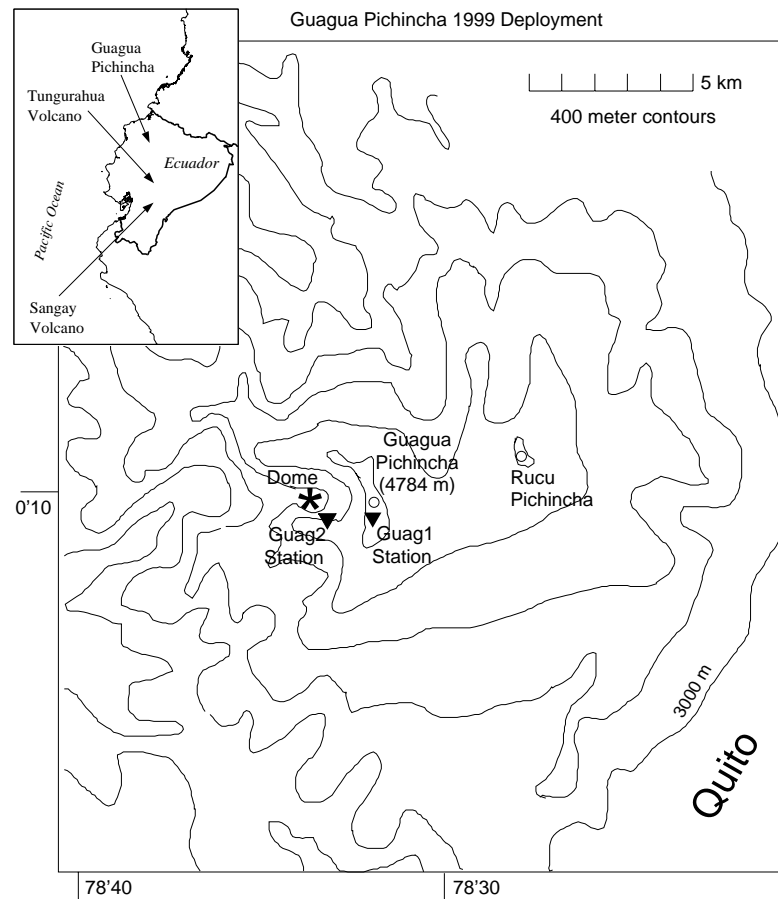
Figure 3.26 Pichincha Station Map - Pichincha 1998-1999 low-frequency microphone station locations. Network seismic station CGG is situated at Guag1. The microphone at Guag1 was a single-element Venema microphone that was operational until June, 1999. Station Guag2 contained a McChesney 16-element microphone array which operated from June 1999 until October 1999.

seismometer 1500 m from the vent at station Guag1 (see figure 3.26). In June, 1999, the single element condenser microphone was replaced by a McChesney 16-element, 4-meter aperture electret condenser microphone array which was co-located with a network seismometer 600 meters from the vent at Guag2. Both instruments were employed primarily to help differentiate between explosion events and shallow sub-surface seismicity. Acoustic signals were telemetered to the Instituto Geofisico of the Escuela Politecnica in Quito for evaluation.

3.7.2 Data Overview

The single-element microphone at Guag1 was replaced by a 16-element microphone array at Guag2 because it appeared as though most of the acoustic signals at Guag1 were being obscured by high levels of wind noise. Indeed, wind was consistently strong at station Guag1, which was located near the summit of Pichincha. Out of approximately 100 possible phreatic explosions (identified through seismic channels), only about a dozen events have associated clear infrasonic pulses similar to those exhibited at the other volcanoes (see figure 3.27 for examples). Interpretation of the acoustic signals recorded at Guag1 is further hampered by a lack of independent observations of the explosions. Audible and visual reports of the explosions are lacking for the period of operation of Guag1 and it is still not entirely clear which seismograms correspond to explosive gas release.

One of the most interesting observation from the Guag1 data, is that acoustic pulses do not follow the onset of seismic signals by a fixed, predictable time interval. At an epicentral distance of 1500 meters, this travel time difference should be approximately 4 seconds for a concurrent seismo-acoustic source at the vent. However, the explosions recorded at Guag1 generally show acoustic arrivals lagging behind seismic arrivals by more than one minute. This indicates that either sub-surface seismicity precedes gas release from the vent or that the initial venting of gas is too insignificant to register on the acoustic channel.

The 16-element microphone was designed and deployed at Guag2 to increase acoustic signal-to-noise (see appendix B). Closer proximity to the vent, deployment in the lee of a ridge, and the spatial filtering of 16 individual sensors resulted in generally low wind noise. However, despite wind noise reduction, clear impulsive acoustic signals were not forthcoming. Obvious acoustic signals are associated with only a minority of the possible explosion events identified from seismic records. When the infrasonic explosion signals are present, they tend to be broad-band (1-15 Hz), tremor-like, relatively emergent, and
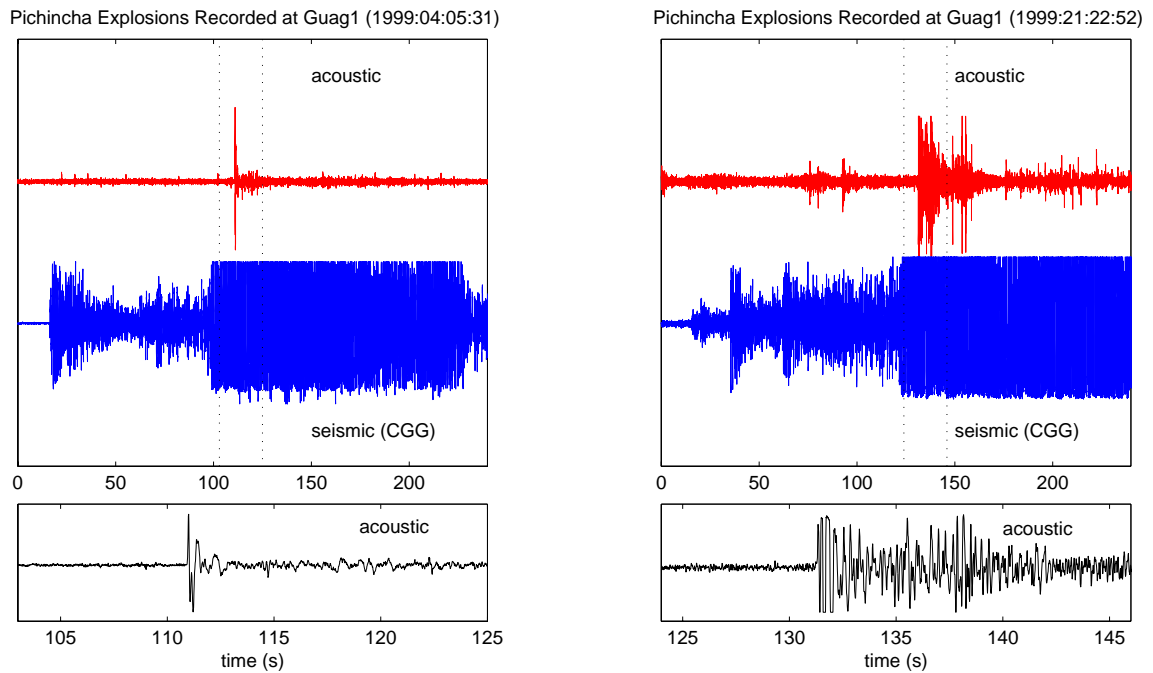
Figure 3.27 Pichincha Explosion Examples from Guag1 - Two normalized explosion waveforms recorded acoustically at station Guag1 (top trace) and seismically at station CGG (bottom trace). Signals are clipped due to dynamic range limitations of the telemetry. Enlargements of a portion of the acoustic traces are included in separate panels below each event.

follow the seismic onsets by as much as 90 seconds (see figure 3.28). Instrument response and propagation filters notwithstanding, the explosion sources at Pichincha during the summer of 1999 are dramatically different from those at Strombolian-type volcanoes. Only a few firsthand reports are available from witnesses but they appear to confirm an entirely different degassing mechanism. These reports describe continuous 'jetting' noises and longer-duration degassing [Mario Ruiz, personal communication, 1999] instead of the 'booming' or 'banging' associated with impulsive explosions at Karymsky, Sangay, and Tungurahua.

3.7.3 Utility of Acoustic Monitoring

The intriguing acoustic signals recorded at Pichincha indicate an activity that is distinct from the Strombolian-type volcanoes where infrasonic recordings are typically made. Not only is the frequency content of the infrasonic signals substantially different at

Pichincha Explosions Recorded at Guag2 (September, 1999)

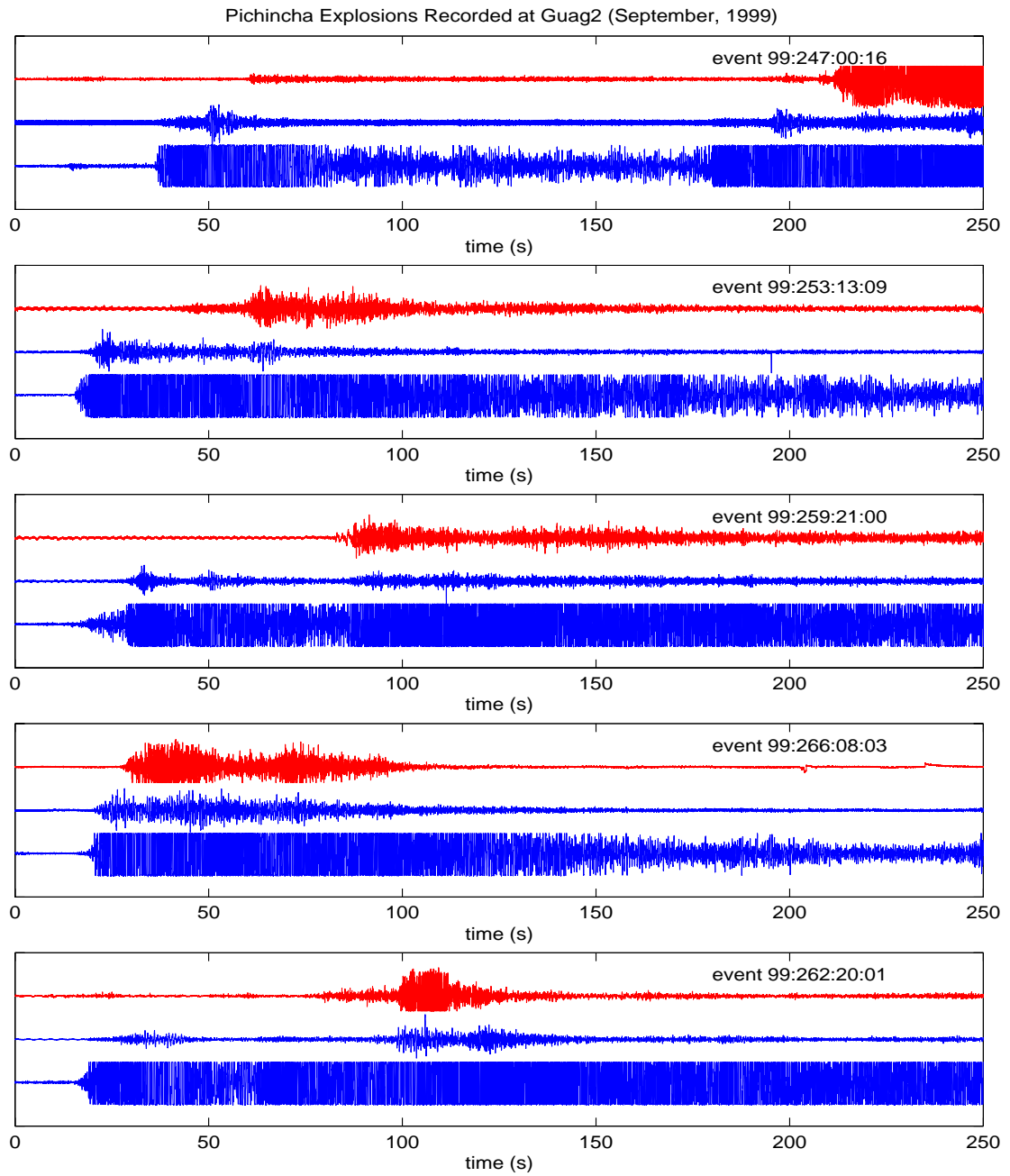**Figure 3.28 Pichincha Explosion Examples from Guag2 - Five normalized explosions recorded with the McChesney 16-element microphone at station Guag2 (top trace) and with short-period network seismometers at station CGG (bottom two traces). Both the low-gain seismic trace from CGG (middle) and high-gain seismic trace from CGG (bottom) are provided. Signals are clipped due to dynamic range limitations of the telemetry.**

Pichincha, but the travel-time difference between acoustic and seismic phases indicate a substantial amount of pre-eruptive seismicity. Hypocenter locations determined by the local network indicate that many of the explosion sources may initiate as deep as three kilometers below the vent [personal communication, Mario Ruiz, 1999]. Travel time differences between acoustic and seismic phases exceeding several tens of seconds could reflect the time necessary for gas to breach the surface from an initial rupture source. The general lack of impulsive acoustic signals and the presence of extended-duration broad-band signals (many minutes long in some cases) indicates a more continuous, less impulsive style of degassing and/or a very weak eruption onset. In chapter 2, infrasonic signals at Karymsky were found to be weak relative to Erebus and were explained by explosion sources occurring at some depth within a conduit. If Pichincha explosion sources are characterized by relatively deep fragmentation depths, gas release from Pichincha could be less impulsive resulting in infrasonic pressure traces with relatively low amplitudes. In the future, it will be critical to decrease speculation about the degassing sources at Pichincha by having more visual observations of explosions. In addition, seismo-acoustic stations with portable dataloggers of sufficient dynamic range need to be deployed at an array of several stations so that broad-band infrasonic explosion signals may be discriminated from wind noise.

3.8 Discussion

Acoustic airwaves generated by volcanic explosions provide an excellent tool for the study of degassing source processes because atmospheric propagation filters are relatively benign. Seismic energy propagating through a much more complex, heterogeneous, volcanic medium, suffers much more significant filtering. Because earth propagation filters can be so severe, seismic waveforms from two different explosion sources may appear relatively similar. The subtle differences in the character of explosive degassing is thus best expressed in infrasonic pressure waveforms (see figure 3.29).
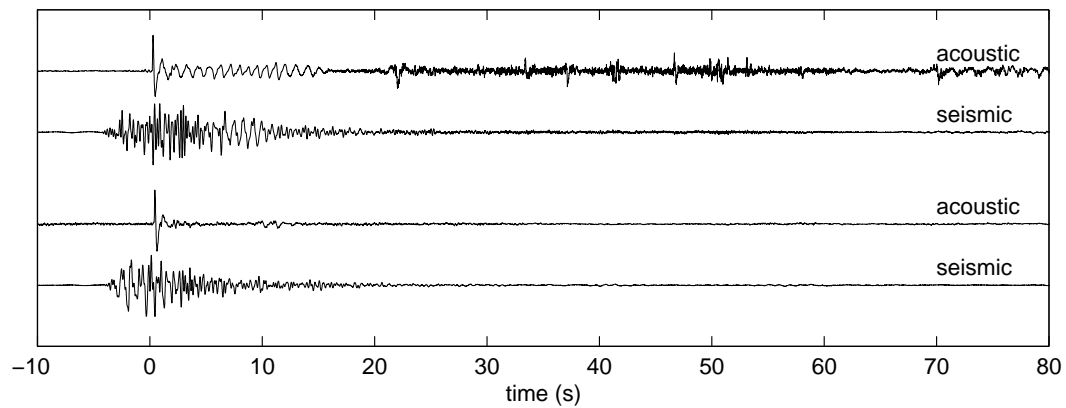
Figure 3.29 Differences in Degassing Expressed by Infrasound - Two different explosions (1999:251:07:37 and 1999:251:10:15) recorded at Karymsky Volcano. Despite similar seismic envelopes and seismic coda lengths, the associated acoustic signals are quite different.

Researchers at several other erupting volcanoes (Klyuchevskoi [Firstov & Kravchenko, 1996], Stromboli [Vergniolle et al., 1996], Unzen [Yamasato, 1998], Sakurajima [Garces et al., 1999], Arenal [Hagerty et al., 2000]) have already recognized the value of infrasound for understanding volcanic degassing phenomena. Infrasonic signals provide a unique opportunity for the comparison of elastic energy generated by different volcanic centers because recorded infrasonic pressure traces are mostly independent of site-specific propagation effects. A critical comparison of seismic signals from explosions at two different volcanoes must take into account variable site responses, instrument responses, background seismic noise, and most importantly volcanic structure and propagation paths. However, corresponding infrasonic signals from two different volcanoes are only minimally filtered by atmospheric propagation (for experiments where microphones are deployed within several kilometers of the vent). Figure 3.30 displays examples of infrasonic pressure traces recorded at Klyuchevskoi, Stromboli, Unzen, Arenal, Sakurajima, so that comparisons may be made with the infrasonic signals introduced earlier in this chapter.

Of all the pressure traces displayed in figure 3.30, Klyuchevskoi and Stromboli infrasonic signals are the most similar in appearance to the explosion signals recorded at Erebus
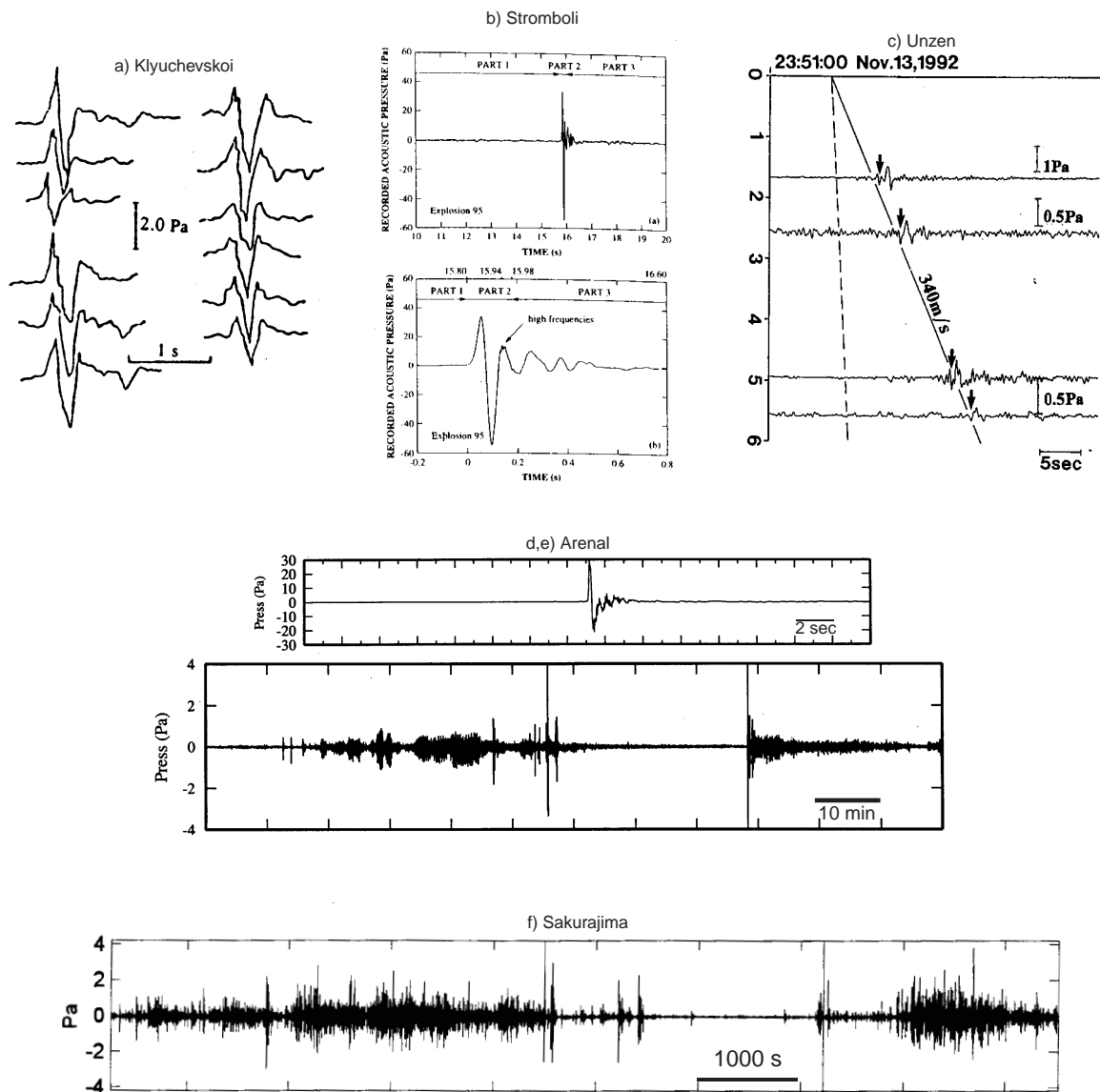
Figure 3.30 Infrasonic Records From Degassing Volcanoes - Acoustic records of degassing activity from several volcanoes. Examples are from: a) Klyuchevskoi [Firstov & Kravchenko, 1996], b) Stromboli [Vergniolle et al., 1996], c) Unzen [Yamasato, 1998], d-e) Arenal [Hagerty et al., 2000], f) Sakurajima [Garces et al., 1999].

Volcano (see figures 3.6 and 3.30a,b). The infrasonic examples from each of these volcanoes consist of single, short-duration sinusoidal pulses. Incidentally, the viscosity of the fluid magmas is comparable at these three volcanoes (Klyuchevskoi - basalt [Firstov & Kravchenko, 1996], Stromboli - basalt [Vergniolle et al., 1996], and Erebus -

phonolite [Dibble, 1994]). At both Stromboli and Erebus, bubbles have been observed rising to the surface and bursting and it is probable that the same mechanism occurs at Klyuchevskoi [Firstov & Kravchenko, 1996]. Degassing signals which are characterized primarily by a single short-duration infrasonic pulse appear to represent a gas volume rupture from near the surface of an open, low-viscosity fluid body (either a conduit or lava lake). Gas release in this type of environment may occur without an equivalent ejection of degassed magma.

Arenal infrasound can be best considered an analog for infrasonic signals recorded at both Karymsky and Sangay (see figures 3.13, 3.18, and 3.30d,e). Explosive activity at these three volcanoes is described as Strombolian because activity consists primarily of discrete explosion events.   However, the character of the explosions differs fundamentally from low-viscosity Strombolian centers (Stromboli and Erebus) as many of the events have extended degassing infrasonic codas (figure 3.30e).   Extended degassing events at the three sites may be attributed to a combination of higher magma viscosity, impediments in the vent, and/or variable depths of fragmentation [Johnson & Lees, 2000].   It should not be surprising that the magma composition at all three volcanoes is andesite, a more viscous fluid than basalt or phonolite. Though the vents of andesitic Strombolian centers are still considered 'open' [Sparks, 1997], low yield-strength caps of rubble often appear to 'plug' the vent. Flux of solid material from the vents of Karymsky, Sangay, and Arenal is generally greater than the solid flux at the lower viscosity Strombolian-type volcanoes as evidenced by dirtier eruption plumes, emission of large bombs, and concurrent lava flows [Johnson & Lees, 2000; Hagerty et al., 2000]. It may be that degassing at these more viscous, andesitic, Strombolian-type centers can not occur without a corresponding flux of exsolved magma.

Sakurajima acoustic signals and eruptive behavior most closely resemble the acoustic signals and eruptive behavior from Tungurahua. At both Sakurajima and Tungurahua (see figures 3.22, 3.23, and 3.30f), infrasonic signals are relatively high-amplitude and

quasi-continuous for time intervals exceeding several hours. During the periods of infrasonic monitoring at both Tungurahua and Sakurajima, activity is considered Vulcanian, characterized by vigorous and nearly continuous emissions of ballistics, ash, and gas [Garces et al., 1999]. Average plume heights at both Sakurajima and Tungurahua extend several kilometers above the vent, substantially higher than the average plumes associated with the Strombolian explosions at Arenal, Karymsky, Sangay, Erebus, or Stromboli. A critical comparison between infrasound intensities at the Strombolian and Vulcanian sites is an important future study that is not possible with the current datasets.

Unzen and Pichincha degassing signals are both somewhat enigmatic due to the infrequence of visual observations of eruptive activity. Both volcanoes possess active dacite domes which experience occasional sloughing or collapse, but the exact source responsible for the infrasound shown in figures 3.27, 3.28, and 3.30c is unclear. Yamasato (1998) believes that Unzen infrasound is produced by gas escaping through cracks in the dome. Pichincha infrasound signals could be attributed to this mechanism or to the occasional collapse of a small section of the dome [Chris Newhall, personal communication, 1999]. The primary similarities between Unzen and Pichincha infrasound are the relative infrequence of explosions, and a general lack of high-amplitude impulsive event onsets. Often, it is difficult to differentiate low-amplitude degassing signals from background noise at these two volcanoes. Though similarities between Unzen and Pichincha infrasound should not be stressed at this juncture, it can be noted that their infrasonic signals both differ significantly from the infrasound produced by lower-viscosity volcanoes.

3.9 Summary and Conclusion

The acoustic and seismic signals presented in this chapter come from five volcanoes which exhibit frequent, but relatively low-vigor degassing explosions. With the exception of Pichincha Volcano (dacitic composition), the volcanoes each have relatively

low viscosity magmas (phonolite - Erebus, andesite - Karymsky, Sangay, and Tungurahua). At the time of study, Karymsky, Sangay, and Erebus each produced distinct degassing explosions characteristic of Strombolian-type activity. Tungurahua had a more vigorous and continuous Vulcanian style of degassing. And Pichincha displayed irregular phreato-magmatic or dome-collapse activity. With the exception of Pichincha, the vents at each volcano can be broadly classified as 'open'.

In each field site electret condenser element microphones with responses in the near-infrasonic bandwidth were co-deployed with seismometers less than 10 km from the degassing sources. At these distances, verification of explosive degassing was trivial during periods of light wind contamination. However, the deployment of multiple microphones (such as the arrays at Karymsky and Erebus) greatly improved signal analysis. These arrays allow for the recovery of accurate explosion source overpressures, as well as source origin locations and times. Furthermore, the arrays enable an understanding of the filtering and magnification effects caused by changeable atmospheric structure (refer to chapters 1 and 2). In the future, Sangay, Tungurahua, and Pichincha would each benefit from studies which include deployment of multiple microphones. It will be equally important to document the degassing signals visually at these sites. Pichincha and other active volcanoes with high-silica, viscous magmas must receive more infrasonic attention in the future because their activity is less well-understood than the activity at Strombolian-type volcanoes, which have been the traditional focus of seismo-acoustic experiments. Visual observations are much more difficult to achieve at silicic systems because their explosions tend to be infrequent and more hazardous.

Infrasonic monitoring of volcanic activity provides a valuable tool for both scientific analysis and hazard assessment. From a research standpoint, infrasound offers the means to reconstruct source motions at the vent. Unlike volcano seismology, infrasound is a direct measure of the acceleration of gases out of a volcano and is thus a more

appropriate tool for constraining degassing source dynamics. In many instances (such as at Tungurahua and Pichincha), infrasound offers the only reliable means to differentiate between sub-surface seismicity and the seismicity associated with explosive degassing. Seismic source motions internal to a volcano provide much useful information about volcanic unrest, but it is ultimately the surficial processes (the presence of an eruption) which create volcanic hazards. Although this dissertation focuses primarily on volcanoes with low objective hazard (such as Erebus and Karymsky), the experiments at these 'laboratory' volcanoes provide a framework for understanding infrasound generation at more explosive systems. Future studies of eruption dynamics and future responses to volcanic crises could be well-served by the incorporation of low-frequency acoustic monitoring.

List of References

Aki, K. and Koyanagi, R. (1981). Deep volcanic tremor and magma ascent mechanism under Kilauea, Hawaii. *Journal of Geophysical Research*, 86(B8), 7095-7110.

Andres, R.J. and Kasgnoc, A.D. (1998) A time-averaged inventory of subaerial volcanic sulfur emissions. *Journal of Geophysical Research*, 103(D19), 25251-25261.

Bass, H.E. and Bauer, H.J. (1972). Atmospheric absorption of Sound: Analytical expressions. *Journal of the Acoustical Society of America*, 52(3), 821-825.

Bedard, A.J. and Georges, T.M. (2000). Atmospheric infrasound, *Physics Today,* 53(3), 32-37.

Beer, T. (1974). *Atmospheric Waves*. Wiley, New York, 300 pp.

Benoit, J.P. and McNutt, S.R. (1997). New constraints on source processes of volcanic tremor at Arenal Volcano, Costa Rica using broadband seismic data. *Geophysical Research Letters*, 24(4), 449-452.

Boatwright, J. (1980). A spectral theory for circular seismic sources: simple estimates of source dimension, dynamic stress drop, and radiated seismic energy. *Bulletin of the Seismological Society of America*, 70(1), 1-27.

Brodsky, E.E., Kanamori, H., and Sturtevant, B. (1999). A seismically constrained mass discharge rate for the initiation of the May 18, 1980 Mount St. Helens eruption. *Journal of Geophysical Research*, 104(B12), 29387-29400.

Chouet, B.A., Dawson, P.B., De Luca, G., Martini, M., Milana, G., Saccorotti, G., and Scarpa, R. (1998). Array analyses of seismic sources at Stromboli. *Acta Vulcanologica*, 10(2), 367-382.

Clift, R., Grace, J.R., and Weber, M.E. (1978). *Bubbles, Drops and Particles*. Academic Press, New York, 380 pp.

Dibble, R.R. (1994). Velocity modeling in the erupting magma column of Mount Erebus, Antarctica. *Volcanological and Environmental Studies of Mount Erebus, Antarctica, Antarctic Research Series*, 66, 17-33.

Dibble, R.R., Kienle, J., Kyle, P.R., and Shibuya, K. (1984). Geophysical Studies of Erebus Volcano, Antarctica, from 1974 December to 1982 January. *New Zealand Journal of Geology and Geophysics*, 27(4), 425-455.

Dibble, R.R., O'Brien, B., and Rowe, C.A. (1994). The velocity structure of Mount Erebus, Antarctica, and its lava lake. *Volcanological and Environmental Studies of Mount Erebus, Antarctica, Antarctic Research Series*, 66, 1-16.

Dobrovol'skiy, I.P. (1994). Seismic efficiency of the tectonic earthquake. *Physics of the Solid Earth*, 30(5), 462-465.

Duvall, W.I. and Stephenson, D.E. (1965). Seismic energy available from rockbursts and underground explosions. *Transactions of the Society of Mining Engineers*, 232(3), 235-240.

Fagents, S.A. and Wilson, L. (1993). Explosive volcanic eruptions-VII. The ranges of pyroclasts ejected in transient volcanic explosions. *Geophysical Journal International*, 113(2), 359-370.

Fay, J.A. (1994). *Introduction to Fluid Mechanics*. MIT Press, Cambridge, 605 pp.

Fehler, M. (1983). Observations of volcanic tremor at Mount St. Helens Volcano. *Journal of Geophysical Research*, 88(B4), 3476-3484.

Fairfield, C. (1980). OMSI sound project; the acoustic effects of the Mount St. Helens eruption on May 18, 1980. *Oregon Geology*, 42(12), 200-202.

Firstov, P.P. and Kravchenko, N.M. (1996). Estimation of the amount of explosive gas released in volcanic eruptions using air waves. *Volcanology and Seismology*, 17, 547-560.

Ford, R.D. (1970). *Introduction to Acoustics*. Elsevier, New York, 154 pp.

Garces, M.A., Hagerty, M.T., and Schwartz, S.Y. (1998a). Magma acoustics and time-varying melt properties at Arenal Volcano, Costa Rica. *Geophysical Research Letters*, 25(13), 2293-2296.

Garces, M.A., Hansen, R.A., and Lindquist, K. (1998b). Traveltimes for infrasonic waves propagating in a stratified atmosphere. *Geophysical Journal International*, 135(1), 255-263.

Garces, M.A., Iguchi, M., Ishihara, K., Morrissey, M. Sudo, Y., and Tsutsui, T. (1999) Infrasonic precursors to a vulcanian eruption at Sakurajima Volcano, Japan. *Geophysical Research Letters*, 26(16), 2537-2540.

Garces, M.A. and McNutt, S.R. (1997). Theory of the airborne sound field generated in a resonant magma conduit. *Journal of Volcanology and Geothermal Research*, 78(3-4), 155-178.

Gordeev, E.I., Kasahara, M., Levina, V.I., Miyamachi, H., and Chebrov, V.N. (1997). Magma activity at Karymsky Volcano and Academy Nauk Caldera (Kamchatka, Russia) triggers large tectonic (M7.0) event. *Eos Transactions, American Geophysical Union*, 78(46), Fall Meeting Supp., F442.

Hagerty, M., Schwartz, S.Y., Garces, M., and Protti, M. (2000). Analysis of seismic and acoustic observations at Arenal Volcano, Costa Rica, 1995-1997. *Journal of Volcanology and Geothermal Research*, 101(1-2), 27-65.

Hall, M.L. (1977). *El Volcanismo en el Ecuador*. IPGH, Quito, 120 pp.

Hall, M.L., Robin, C., Beate, B., Mothes, P., and Monzier, M. (1999). Tungurahua Volcano, Ecuador; structure, eruptive history and hazards. *Journal of Volcanology and Geothermal Research*, 91(1), 1-21, 1999.

Hellweg, M. (2000). Physical models for the source of Lascar's harmonic tremor, *Journal of Volcanology and Geothermal Research*, 101(1-2), 183-198.

Ivanov, B.V., Braitseva, O.A., and Zubin, M.I. (1991). Karymsky Volcano. *Active Volcanoes of Kamchatka 2*. Nauka, Moscow, 180-203.

Jensen, F.B., Kuperman, W.A., Porter, M.B., and Schmidt, H. (1994). *Computational Ocean Acoustics*. AIP Press, New York, 612 pp.

Johnson, J.B. and Lees, J.M. (2000). Plugs and chugs - seismic and acoustic observations of degassing explosions at Karymsky, Russia and Sangay, Ecuador. *Journal of Volcanology and Geothermal Research*, 101(1-2), 67-82.

Johnson, J.B., Lees, J.M., and Gordeev, E.I. (1998). Degassing explosions at Karymsky Volcano, Kamchatka. *Geophysical Research Letters*, 25(21), 3999-4042.

Johnson, J.B. and Malone, S.D. (1997). Acoustic Air-wave Propagation from the 1980 Mount St. Helens Eruption. *Eos Transactions, American Geophysical Union*, 78(46), Fall Meeting Supp., F130.

Johnson, J.B., Ruiz, M.C., and McChesney, P. (1999). Low-frequency acoustic monitoring and wind-filtering at active volcanoes. *Eos Transactions, American Geophysical Union*, 80(46), Fall Meeting Supp., F1148.

Julian, B.R. (1994). Volcanic tremor: Nonlinear excitation by fluid flow. *Journal of Geophysical Research*, 99(B6), 11859-11877.

Kanamori, H. and Given, J.W. (1982). Analysis of long-period seismic waves excited by the May 18, 1980, eruption of Mount St. Helens; a terrestrial monopole? *Journal of Geophysical Research*, 87(B7), 5422-5432.

Kinney, G.F. and Graham, K.J. (1985). *Explosive Shocks in Air*. Springer-Verlag, New York, 269 pp.

Law, R. (2000). *Magmatic degassing and eruptive behavior of Karymsky Volcano, Kamchatka, Russia; evaluated using correlation spectrometer (COSPEC) measurements of SO2 emissions*. Master's thesis, New Mexico Technical University, Socorro, NM.

Law, R. and Kyle, P. (1999). Correlation spectrometer (COSPEC) measurements of SO2 emissions during strombolian eruptions at Karymsky Volcano, Kamchatka, Russia. Eos Transactions, American Geophysical Union, 80(46), Fall Meeting Supp., F927.

Lay, T. and Wallace, T. (1995). *Modern Global Seismology*. Academic Press, San Diego, 521 pp.

Lees, J.M. and Bolton, E.W. (1998). Pressure cookers as volcano analogues. *Eos Transactions, American Geophysical Union*, 79(45), Fall Meeting Supp., F620.

Lighthill, M.J. (1978). *Waves in Fluids*. Cambridge University Press, New York, 504 pp.

Maekawa, Z. (1968). Noise reduction by screens. *Applied Acoustics*, 1(3), 157-173.

McGetchin, T.R. and Chouet, B.A. (1979). Energy budget of the Volcano Stromboli. *Geophysical Research Letters*, 6(4), 317-320.

McNutt, S.R. (1994). Volcanic tremor amplitude correlated with the volcanic explosivity index and its potential use in determining ash hazards to aviation. *Acta Vulcanologica*, 5, 193-196.

Miksis, M. and Ting, L. (1986). Wave propagation in a bubbly liquid with finite-amplitude asymmetric bubble oscillations. *Physics of Fluids*, 29, 603-618.

Mikumo, T. and Bolt, B.A. (1985). Excitation mechanism of atmospheric pressure waves from the 1980 Mount St. Helens eruption. *Geophysical Journal of the Royal Astronomical Society*, 81(2), 445-461.

Monzier, M., Robin, C., Samaniego, P., Hall, M.L., Cotten, J., Mothes, P., and Arnaud, N. (1999). Sangay Volcano, Ecuador; structural development, present activity and petrology. *Journal of Volcanology and Geothermal Research*, 90(1-2), 49-79.

Mori, J., Patia, H., McKee, C., Itikarai, I. Lowenstein, P., De Saint Ours, P., and Talai, B. (1989). Seismicity associated with eruptive activity at Langila Volcano, Papua New Guinea. *Journal of Volcanology and Geothermal Research*, 38(3-4), 243-255.

Neuberg, J., Luckett, R. Baptie, B., and Olsen, K. (2000). Models of tremor and low-frequency earthquake swarms on Montserrat. *Journal of Volcanology and Geothermal Research*, 101(1-2), 83-104.

Newhall, C.G. and Self, S. (1982). The volcanic explosivity index (VEI): An estimate of explosive magnitude for historical volcanism. *Journal of Geophysical Research*, 87(C2), 1231-1238.

Nicholls, H.R. (1962). Coupling explosive energy to rock. *Geophysics*, 27(3), 305-316.

Power, J. (1993). Sounds during the August 18, 1992, Spurr Eruption. *Alaska Volcano Observatory Newsletter*, 5(5), 14-15.

Reed, J.W. (1987). Air pressure waves from Mount St. Helens eruptions. *Journal of Geophysical Research*, 92(D10), 11979-11982.

Reed, J.W. (1972). Attenuation of blast waves by the atmosphere. *Journal of Geophysical Research*, 77(9), 1616-1622.

Richards, A.F. (1963) Volcanic sounds: investigation and analysis. *Journal of Geophysical Research*, 68(3), 919-928.

Ripepe, M. and Gordeev, E.I. (1999). Gas bubble dynamics model for shallow volcanic tremor at Stromboli. *Journal of Geophysical Research*, 104(B5), 10639-10654.

Ripepe, M., Rossi, M., and Saccorotti, G. (1993). Image processing of explosive activity at Stromboli. *Journal of Volcanology and Geothermal Research*, 54(3-4), 335-351.

Rowe, C.A., Aster, R.C., Kyle, P.R., Dibble, R.R., and Schlue, J.W. (2000). Seismic and acoustic observations at Mount Erebus Volcano, Ross Island, Antarctica, 1994-1998. *Journal of Volcanology and Geothermal Research*, 101(1-2), 105-128.

Ruiz, M., Hall. M., Samaniego, P., and Metaxian, J.P. (1997). Tremor Activity in Tungurahua Volcano, Ecuador, *Abstracts of Volcanic Activity and the Environment, IAVCEI General Assembly*, 126.

Schlindwein, V., Wassermann, J., and Scherbaum, F. (1995). Spectral analysis of harmonic tremor signals at Mt. Semeru Volcano, Indonesia. *Geophysical Research Letters*, 22(13), 1685-1688.

Sparks, R.S.J. (1978). The dynamics of bubble formation and growth in magmas; a review and analysis. *Journal of Volcanology and Geothermal Research*, 3(1-2), 1-37.

Sparks, R.S.J. (1997). *Volcanic Plumes*. Wiley, New York, 574 pp.

Sparks, R.S.J. (1998). *The Physics of Explosive Volcanic Eruptions*, Geological Society, London, 186 pp.

Tahira, M., Nomura, M., Sawada, Y., and Kamo, K. (1996). Infrasonic and acoustic-gravity waves generated by the Mount Pinatubo eruption of June 15, 1991. *Fire and Mud*. University of Washington Press, Seattle, 601-614.

Taran, Y.A., Rozhkov, A.M., Serafimova, E.K., Esikov, A.D., and Yesikov, A.D. (1991). Chemical and isotopic composition of magmatic gases from the 1988 eruption of Klyuchevskoy Volcano, Kamchatka. *Journal of Volcanology and Geothermal Research*, 46(3-4), 255-263.

Thompson, G., McNutt, S.R., and Tytgat, G. (in press). Three distinct regimes of volcanic tremor associated with eruptions of Shishaldin Volcano, Alaska, April 1999. *Bulletin of Volcanology*.

Tomaru, A. (1995). Numerical study of nucleation and growth of bubbles in viscous magmas. *Journal of Geophysical Research*, 100(B2), 1913-1931.

Truax, B. (1978). *The World Soundscape Project's Handbook for Acoustic Ecology*. A.R.C. Publications, Vancouver, 171 pp.

Vergniolle, S., Brandeis, G., and Mareschal, J.-C. (1996). Strombolian explosions 2, Eruption dynamics determined from acoustic measurements. *Journal of Geophysical Research*, 101(B9), 20449-20466.

Wada, Y. (1994). On the relationship between dike width and magma viscosity. *Journal of Geophysical Research*, 99(B9), 17743-17755.

Walker, D. and Mullins, O. (1981). Surface tension of natural silicate melts from 1200-1500 degrees C and implication for melt structure. *Contributions to Mineralogy and Petrology*, 76(4), 455-462.

Wilson, L. (1980). Relationship between pressure, volatile content, and ejecta velocity in three types of volcanic explosion. *Journal of Volcanology and Geothermal Research*, 8(2-4), 297-313.

Wilson, L., Sparks, R.S.J., Huang, T.C., and Watkins, N.D. (1978). The control of volcanic column heights by eruption energetics and dynamics. *Journal of Geophysical Research*, 83(B4), 1829-1836.

Yamasato, H. (1997). Quantitative analysis of pyroclastic flows using infrasonic and seismic data at Unzen Volcano, Japan. *Journal of Physics of the Earth*, 45(6), 397-416.

Yamasato, H. (1998). Nature of infrasonic pulse accompanying low frequency earthquake at Unzen Volcano, Japan. *Bulletin of the Volcanological Society of Japan*, 43, 1-13.

Appendix A - Formula Derivations

Equation 1.2

The total energy contained in an acoustic wavefield is a combination of the kinetic energy associated with particle motion and the potential energy associated with elasticity. Ford (1970) gives a formula for energy density of an acoustic airwave:

$$D(x, t) = \frac{\Delta P^2}{\rho_a c^2}$$

The total acoustic energy contained in a hemispherically radiating infrasonic wave is then calculated by integrating over a volumetric halfspace:

$$E_{acoustic} = \int D(x, t) dV = 2\pi \int_0^\infty D(R, t) R^2 dR = 2\pi \int_0^\infty \left(\frac{\Delta P(R, t)^2}{\rho_a c^2} \right) R^2 dR$$

Since $\Delta P(R, t)R = \Delta P\left(r, t - \frac{(R-r)}{c} \right)r$ for a radially expanding acoustic wave [Ford, 1970], the acoustic energy can be rewritten as:

$$E_{acoustic} = \frac{2\pi r^2}{\rho_a c^2} \int_0^\infty \Delta P\left(r, t - \frac{(R-r)}{c} \right)^2 dR$$

The radial increment dR at a fixed distance is equal to cdt, yielding:

$$E_{acoustic} = \frac{2\pi r^2}{\rho_a c} \int \Delta P(t)^2 dt \tag{1.2}$$

Equation 1.15

The ideal gas law ($PV = nRT$) can be rewritten in the form:

$$(PV^\gamma)P^{\gamma - 1} = (nRT)^\gamma$$

Which leads to the relationship:

$$\frac{(PV^{\gamma})P^{\gamma-1}}{(P_oV_o{}^{\gamma})P_o{}^{\gamma-1}} = \frac{(nRT)^{\gamma}}{(nRT_o)^{\gamma}}$$

Rewriting in terms of sound speed ($(c/c_o)^2 = T/T_o$ from equation 1.5) and assuming adiabatic expansion of gases ($PV^{\gamma} = P_oV_o{}^{\gamma}$ [Kinney & Graham, 1985]) gives:

$$\frac{P^{\gamma-1}}{P_o{}^{\gamma-1}} = \frac{c^{2\gamma}}{c_o{}^{2\gamma}} \Rightarrow \frac{c}{c_o} = \left(\frac{P}{P_o}\right)^{\frac{\gamma-1}{2\gamma}}$$

Defining Δc as the difference between sound speed at excess pressure (ΔP) and ambient sound speed leads to:

$$\Delta c = c_o\left[\left(\frac{P_o + \Delta P}{P_o}\right)^{\frac{\gamma-1}{2\gamma}} - 1\right] \tag{1.15}$$

Equation 2.2 and 2.3

For spherically expanding pressure pertubations [Ford, 1970]:

$$\Delta P(R, t)R = \Delta P\left(r, t - \frac{(R-r)}{c}\right)r$$

Therefore:

$$R\Delta P(R)_{max} = r\Delta P(r)_{max}$$

where R and r correspond to a reference radius and the radius of the measured excess pressure (ΔP). However, by incorporating focusing effects (the magnification factor (MF) introduced in chapter 1), the relationship must be modified:

$$(MF)R\Delta P(R)_{max} = r\Delta P(r)_{max}$$

Reduced pressure is then defined as the effective peak excess pressure at a radius of one meter ($R = 1$):

$$R_P = \frac{r\Delta P_{max}}{(MF)} \tag{2.2}$$

From chapter 1, the energy contained in the acoustic wavefield for a hemispherically radiating acoustic source is:

$$E_{acoustic} = \frac{2\pi r^2}{\rho_o c_o}\int \Delta P(t)^2 dt \tag{1.2}$$

For a simple source with acoustic radiation that is affected by atmospheric structure, excess pressure can be modified by a magnification factor for known focusing effects:

$$E_{acoustic} = \frac{2\pi r^2}{\rho_o c_o}\int \frac{\Delta P}{MF} dt \tag{2.3}$$

Equation 2.9 and 2.10

For a hemispherical plume volume, the radius of the incandescent volume can be related to the area of incandescence.

$$R_l = \left(\frac{2A_l}{\pi}\right)^{1/2}$$

The incandescent hemispherical plume volume is proportional to the radius cubed:

$$V_l = \frac{(4/3)\pi R_l^3}{2} = \frac{(4/3)\pi}{2}\left(\frac{2A_l}{\pi}\right)^{3/2} = \sqrt{\frac{32}{9\pi}}A_l^{3/2} \tag{2.9}$$

And ejection velocity is approximated as the rate of change of the plume radius:

$$U_M = \frac{dR_l}{dt} = \frac{d}{dt}\left(\frac{2A_l}{\pi}\right)^{1/2} = \frac{1}{\sqrt{2\pi A_l}}\left(\frac{dA_l}{dt}\right) \tag{2.10}$$

Equation 2.22

Energy dissipation is equivalent to $\int F \cdot dl$. In the case of constant-velocity fluid flow through a circular pipe of finite length (L), the force acting upon a fluid element as it passes through the circular pipe is:

$$F = \frac{\pi D^2}{4}\frac{dP}{dl}L$$

The work done by this force is proportional to the distance traveled by the fluid elements within the conduit. This distance is equivalent to the product of the average flow velocity and the time duration of the flow ($\bar{V}t$). For a steady-velocity flow from a high-pressure reservoir, energy dissipation in the conduit is:

$$\int F \cdot dl = \frac{dP}{dl} \frac{\pi L D^2}{4} \bar{V} t \tag{2.22}$$

It is important to note that this equation is appropriate for instances where the conduit pressure gradient induced by the pressurized reservoir is greater than the hydrostatic pressure gradient (weight of gases in a vertical conduit).

Equation 2.31

For an arbitrary force-time function (see cartoon below):

$$F = \begin{cases} \frac{1}{2} f_o \left(1 - \cos\left(\pi \frac{t}{\tau} \right) \right) & \text{for } (0 < t < 2\tau) \\ 0 & \text{for } (t > 2\tau) \end{cases} \tag{2.29}$$

The final momentum of material accelerated from rest is:

$$MV = \int_0^{2\tau} F \, dt = \int_0^{2\tau} \frac{1}{2} f_o \left(1 - \cos\left(\pi \frac{t}{\tau} \right) \right) dt = f_o \tau$$

And the corresponding maximum thrust force (f_o) is MV/τ (equation 2.30). According to Kanamori & Given (1982), seismic energy generated from a monopole thrust source is:

$$E_{seismic} = \frac{1}{6\pi\rho} \left[\frac{1}{2V_P^3} + \frac{1}{V_S^3} \right] \int_{-\infty}^{\infty} [\dot{F}(t)]^2 dt \tag{2.28}$$

For the arbitrary bell-shaped thrust force:

$$\int_{-\infty}^{\infty} [\dot{F}(t)]^2 dt = (f_o)^2 \int_0^{2\tau} \left[\frac{\pi}{\tau} \sin\left(\pi \frac{t}{\tau} \right) \right]^2 dt = \left(f_o \frac{\pi}{2\tau} \right)^2 \int_0^{2\tau} \left[\frac{1}{2} - \frac{\cos(2\pi t/\tau)}{2} \right] dt = \left(f_o \frac{\pi}{2\tau} \right)^2 \tau$$

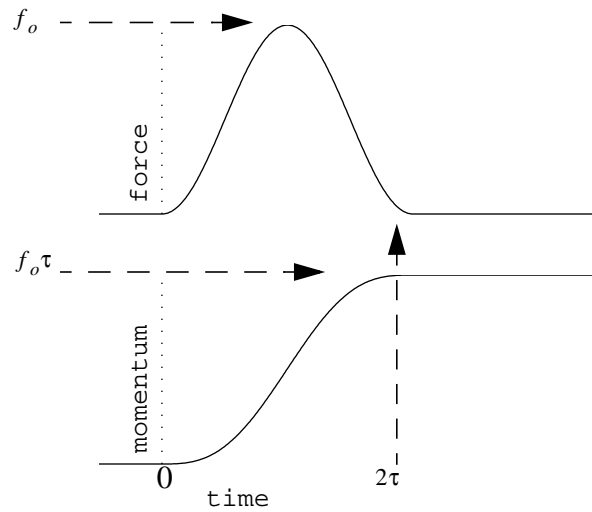Using the relationship $f_o = MV/\tau$, the radiated seismic energy becomes:

Figure A-1 Arbitrary Thrust Function - A bell-shaped force-time function with a maximum force of f_o and a period of 2τ produces a curve with maximum momentum equal to $f_o\tau$.

$$E_{seismic} \approx \frac{\pi}{24} \frac{(MV)^2}{\rho\tau^3} \left[\frac{1}{2V_P^3} + \frac{1}{V_S^3} \right] \qquad (2.31)$$

Equation 2.34

$$E_{Walls} = \frac{1}{25}\rho\bar{V}^3 LDt \qquad (2.33)$$

For a constant density flow through a circular conduit, density can be related to mass by:

$$M = \rho AL = \rho\frac{\pi D^2}{4}L = \rho\frac{\pi D^2}{4}\bar{V}t$$

Substituting for density in equation 2.33 yields:

$$E_{Walls} \approx \frac{4}{25\pi}M\bar{V}^2\frac{L}{D} \qquad (2.34)$$

Appendix B - Microphone Specifications and Wind Noise

Both infrasonic and seismic waveform analysis confront some of the same signal process-
ing issues. In each case instrument response must be removed and environmental noise
must be minimized. This appendix summarizes the responses of the microphones used in
the studies at Erebus, Karymsky, Sangay, Tungurahua, and Pichincha and describes how
transfer functions can be applied for the recovery of the true acoustic pressure time his-
tory. This appendix also details background noise levels and wind noise minimization
schemes used in some of the experiments.

Microphone Response

The pressure sensing elements commonly used in infrasonic studies at volcanoes are
either pressure transducers or electret condenser elements. Both of these devices come
with their own set of benefits and drawbacks. Pressure transducers (used in the Dibble and
Ramey microphones) are economical and have a flat frequency response down to DC fre-
quencies, but suffer from electronic noise. Electret condenser microphones are somewhat
less noisy, but possess a relatively poor response at lower frequencies. The mass-produced
condenser elements (used in the McChesney, Ripepe, and Venema microphones) have cor-
ner frequencies ranging from 1 to 5 Hz which is in the bandwidth of interest for volcanic
infrasound. For this reason they are inferior to more expensive, engineering-quality con-
denser element microphones (such as the Larson-Davis instrument) which has a corner
frequency at 4 seconds.

The active element in both electret condenser elements and pressure transducers operate in
a similar manner. Atmospheric pressure waves deflect a diaphragm (a metal alloy filament
in electret condenser elements and an etched silicon chip in pressure transducers) which
varies the dimension of a capacitive gap. Changes in voltage across the gap are analog fil-
tered and amplified by adjoining circuitry, and then digitized to a datalogger or teleme-
tered as a frequency modulated tone. Because the capacitive gap in an electret condenser

element is 'leaky,' there is a response roll-off at lower frequencies. Pressure transducers on the other hand suffer no leakage if operated in an absolute mode, where one side of the diaphragm is permanently sealed. In this instance barometric pressure fluctuations (which have much higher amplitude ($\sim 10^4$) than recorded infrasound) are usually high-pass filtered before they are conveyed to the recording device. The main deficiency of absolute pressure transducers is their relatively high electronic noise level compared to electret condenser elements. However, the newest generation of pressure transducers (released during the last couple years) have low enough noise levels to make them competitive with electret condenser elements.

Most of the experiments at the five volcanoes used electret condenser elements because of their heightened sensitivity with respect to a noise floor. Since manufacturers do not generally provide frequency response information for electret condenser elements in the infrasonic bandwidth, calibration tests were performed under the direction of Pat McChesney, an engineer for the Pacific Northwest Seismographic Network (PNSN). Pat McChesney designed and constructed a sealed control box with an inward-facing woofer that could be oscillated sinusoidally at infrasonic frequencies. Test microphones were placed in the control box along with a SenSym SCXL004DN absolute pressure transducer of known sensitivity and frequency response. In this manner, the amplitude and phase response of the electret condenser microphones could be assessed for low frequencies. A summary of instrument responses determined in the lab (indicated by a star*) is provided in table B.

Table B Microphone Response Summary - Instrument sensitivity and high-pass 3 dB point reflect the combined response of pressure sensing element, amplifier, and associated filters determined either in the McChesney laboratory control box (*) or in the field by co-location with the Larson-Davis precision microphone (**). Microphones which are not calibrated by either method have responses listed as unknown. For more information about the different experiments where these microphones were deployed, refer to volcano background sections in chapter 3.

station	microphone type	sensitivity	3 dB	station	microphone type	sensitivity	3 dB
EHUT*	Larson-Davis[1]	42 mV/Pa	0.27 Hz**	V3,L3,R3**	Ripepe-B[7]	80 counts/Pa	?
EHUT*	McChesney4[2]	200 mV/Pa	3.0 Hz	V4,L4,R4**	Ripepe-new[7]	210 counts/Pa	?

Table B (continued) Microphone Response Summary

station	microphone type	sensitivity	3 dB	station	microphone type	sensitivity	3 dB
EHEL*	McChesney4[2]	170 mV/Pa	4.9 Hz	Krm3*	Larson-Davis[1]	42 mv/Pa	0.27 Hz
ENKB*	McChesney4[2]	130 mV/Pa	1.4 Hz	Krm3**	McChesney1[2]	50 mv/Pa	~2.5 Hz
ECON*	McChesney4[2]	130 mV/Pa	4.5 Hz	Krm3**	McChesney4[2]	200 mv/Pa	~2.5 Hz
EE1S*	McChesney4[2]	140 mV/Pa	1.7 Hz	Krm9**	McChesney4[2]	100 mv/Pa	~2.5 Hz
EE1S	Dibble[3]	70 mV/Pa	flat	Krm9**	Venema-high[6]	500 mv/Pa	?
Kar1*	Ramey[4]	7.8 mV/Pa	flat	Krm1**	McChesney4[2]	100 mv/Pa	~2.5 Hz
Kar1	Ripepe-I[5]	unknown	?	Krm2**	McChesney4[2]	200 mV/Pa	~2.5 Hz
Kry1*	Larson-Davis[1]	42 mV/Pa?	0.27 Hz	Krm0**	McChesney4[2]	100 mV/Pa	~2.5 Hz
Kry2*	Venema-low[6]	30 mV/Pa	~5 Hz	San1*	Venema-low[6]	~30 mV/Pa	~5 Hz
Kry3*	Venema-high[6]	160 mV/Pa	~4 Hz	Tung	McChesney4[2]	unknown	~2.5 Hz
V1,L1,R1**	Ripepe-new[7]	320 counts/Pa	?	Guag1	Venema-low[6]	unknown	?
V2,L2,R2**	Ripepe-new[7]	310 counts/Pa	?	Guag2	McChesney16[2]	unknown?	?

[1]The Larson-Davis free-field precision microphone used at the experiments at Karymsky and Erebus is a commercially available electret condenser microphone suitable for engineering purposes. The microphone deployed at Karymsky and Erebus consisted of a one-inch electret condenser element #2570, preamp PRM900C, and a power supply 2200C. Specifications are provided by Larson-Davis and verified in the McChesney laboratory calibration box. Laboratory calibration tests reveal a behavior which closely resembles a single-pole high pass filter with corner frequency at 0.27 Hz. In many experiments, the Larson-Davis microphone was temporarily co-deployed with other electret condenser microphones to assess the relative response of the other instruments.

[2]McChesney1, 4, and 16 microphones consist of a variable gain amplifier, low-pass RC filters (~20 Hz), and 1 to 16 individual WM-52BM Panasonic omnidirectional condenser elements. Each Panasonic condenser element has a slightly different sensitivity and corner frequency (~1 to ~5 Hz) which limit their application for infrasonic waveform modeling. However, the spatial wind filtering abilities of the McChesney 4 and 16 boxes allow identification of acoustic pulses in windy conditions (see section on noise in this appendix). Of all the McChesney units used in this study, only the microphones deployed at Erebus have undergone careful laboratory calibration tests to determine sensitivity and corner frequency so that instrument responses may be removed. McChesney microphones deployed at Karymksy were calibrated only by temporary co-location with the Larson-Davis microphone. Frequency response of the McChesney microphones resembles a single-pole high-pass filter to first order. Design and construction of the McChesney microphones is by both the author and Pat McChesney (University of Washington).

[3]The Dibble microphone is a pressure transducer microphone that has been continuously operating at Erebus since 1991. The microphone active element is a SenSym LX02002D transducer. Associated electronics have a passband of 0.3 to 13 Hz. Output from the microphone is telemetered to a data acquisition center in McMurdo. Design and construction is by Raymond Dibble (Victoria University, Wellington, NZ).

[4]The Ramey microphone is a replica of the Dibble microphone that was deployed temporarily at Karymksy in 1997. Pressure sensing element is a SenSym LX06002D transducer. Microphone sensitivity was obtained in laboratory calibration tests in 2000. Frequency response is flat except for a low-pass filter (~20 Hz) used to remove high-frequency acoustic signals. Construction of microphone is by Jim Ramey (University of Washington).

[5]The Ripepe-A microphone contains an electret condenser element, amplifier of unknown gain, and a band-pass filter. It was deployed at Karymsky in 1997. Sensitivity and corner frequencies are not constrained. Design and construction is by Pasquale Poggi (Isstituto di Ottica, Florence, Italy).

[6]Venema microphones (low and high gain) use Radio Shack omnidirectional electret condenser elements (catalog number 270-092B). The attached variable-gain amplifier and low-pass filters (~20 Hz) were designed and built by Brian Venema and the UW Physics electronics shop. This microphone type was used at Karymsky, Sangay, and Pichincha. Unfortunately, laboratory calibration tests conducted in 2000 may reflect deterioration of the sensing elements during their long life span. Absolute sensitivity at Pichincha is entirely unknown because signals were conveyed by telemetry at unknown gain.

[7]Ripepe-B microphones consist of single electret condenser element (unknown manufacturer), amplifier, and low-pass filter. Sensitivity (listed in counts/Pa for the Datamark acquisition system) was determined by temporary co-location of microphones with a Larson-Davis microphone. Microphone circuitry designed and built by Maurizio Ripepe and Evgenii Gordeev (Isstituto di Ottica, Florence, Italy and OMSP, Kamchatka, Russia).

Transfer Function

Deconvolution of the microphone response is a necessary step for infrasonic waveform modeling. In particular, estimates of gas flux from the vent (equations 1.9 and 2.11) depend upon unfiltered pressure time histories. Fortunately, laboratory calibration tests provide sufficient frequency and phase information to generate suitable transfer functions for the Larson-Davis and McChesney microphones. The transfer function for these microphones closely resembles a single-pole high-pass filter. Figure B-1 shows an example of the frequency and phase response for a single Panasonic electret condenser element used in the McChesney 1, 4, and 16 element microphone boxes.
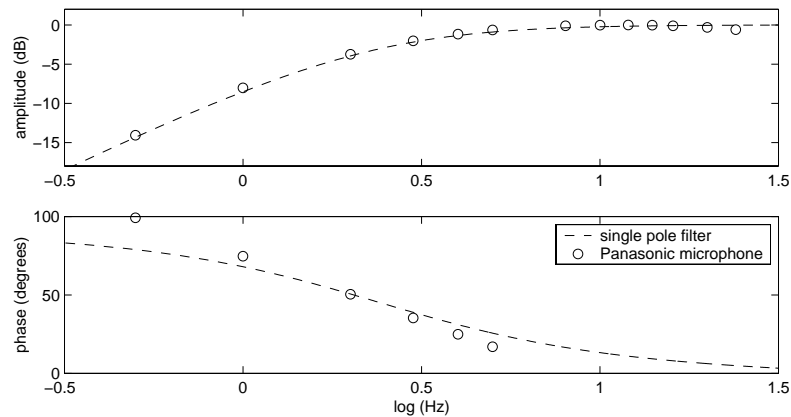
Figure B-1 Frequency Response of Electret Condenser Element - Panasonic electret condenser elements used in the McChesney microphones have frequency responses closely resembling a single-pole high-pass filter. The example shows a microphone element with a corner frequency of 2.5 Hz. Corner frequencies for all Panasonic microphones (WM-52BM) lie between 1 and 5 Hz.

Known instrument response transfer functions may be easily removed in the frequency domain using the MATLAB signal processing toolbox. For infrasonic waveforms analyzed in chapter 2, the microphone response is approximated as a single-pole Butterworth filter of variable corner frequency. Figure B-2 illustrates instrument deconvolution for both the Larson-Davis and a McChesney4 microphone. Both instruments were co-located at Erebus at station EHUT and the similarity of the infrasonic waveforms is greatly improved after the removal of the instrument response (compare B-2a and B-2e).

Reduced pressure (maximum acoustic amplitude) is increased by about 20 percent for the infrasonic trace recorded by the McChesney microphone.
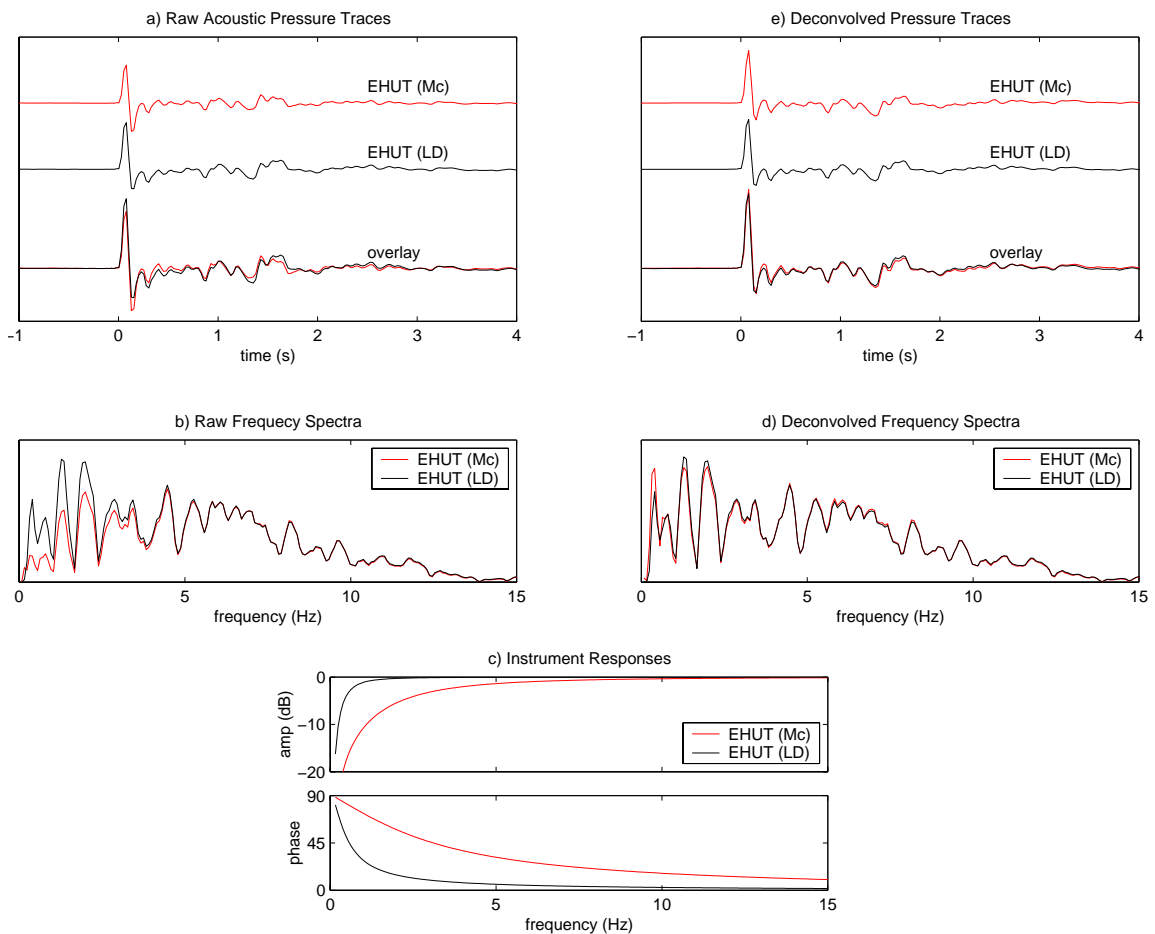

Figure B-2 Deconvolution of Microphone Response - a) Unfiltered acoustic pressure traces and b) associated frequency response. c) Transfer functions for single-pole filters with different 3 dB points. d) Frequency spectra after removal of instrument response and e) deconvolved waveforms.

Noise

Both electronic and environmental noise can be problematic during the analysis of infrasonic signals. Electronic noise level is independent of microphone sensitivity and environmental noise and depends upon the pressure sensing element, associated electronics, and data acquisition system. Though a pre-op-amp may be used to increase effective instrument sensitivity, the inherent electronic noise will also be amplified. In general,

electret condenser elements have lower inherent electronic noise than pressure transducers for identical amplification and data acquisition systems. However, this electronic noise only becomes problematic for pressure transducers deployed in recording situations where environmental and datalogger noise is very low. There was, for instance, no real advantage to using electret condenser elements at Pichincha, because the noise associated with telemetry was far greater than the noise produced by the pressure sensing components.

In most situations, environmental noise (specifically wind) is by far the most significant source of signal corruption of infrasonic pressure records. During periods of heavy winds, the acoustic signals related to degassing may be completely obscured by high amplitude wind 'tremor.' Figure B-3 illustrates acoustic traces associated with both degassing signal and wind noise at Tungurahua Volcano. It should be apparent that wind noise is much higher in amplitude than degassing signals and that it is broad-band (nearly white). Thus it is extremely difficult to remove wind noise during the post-processing of infrasonic data.

Wind noise and wind speed are well-correlated as indicated by figure B-4. For a single pressure sensing element, the root-mean-square pressure seems to be exponentially related to wind speed [Johnson et al., 1999]. During field experiments, the single best tactic for wind noise minimization appears to be the deployment of microphone sensors away from windy locales. As a result, microphones deployed at the five volcanoes from chapter 3 were positioned below ridge tops when possible and within a few centimeters of the ground. Some experimentation was done with the placement of sensors in the lee of a wind barrier, but the exact noise reduction benefits are unknown because turbulent eddies can be generated by these obstacles. Acoustic sensors buried in snow at Erebus Volcano seem to produce the best signal-to-noise of all microphone stations. Unfortunately, the infrasound attenuating properties of this and other types of windscreens is uncertain.

An attempt to filter problematic wind noise resulted in the development of the McChesney 4 and 16-element microphones. These microphones have multiple sensors which are
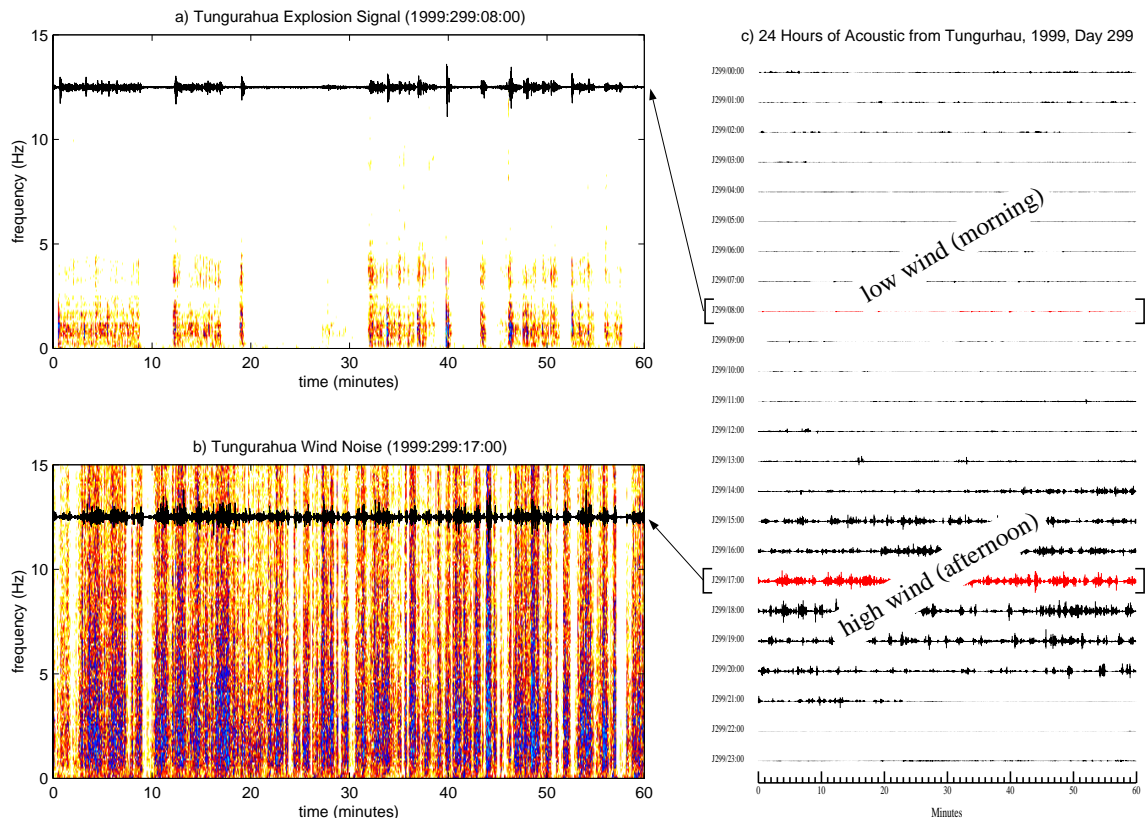
Figure B-3 Tungurahua Wind Noise - a) Low-amplitude infrasonic signals associated with degassing have a predominance of low frequencies b) In contrast, wind noise is high amplitude and broad-band. c) 24-hour acoustogram at Tungurahua shows the relative amplitudes of wind and signal indicating a tendency for wind noise to cluster in time (generally during the afternoon at Tungurahua).

physically separated from one another to spatially filter out incoherent wind noise (see figure B-5). For sensor-spacing less than a few meters, all infrasound is coherently stacked (quarter wavelengths at 20 Hz are about 4 meters), but wind noise across the small array should be incoherent and combine destructively. Signal-to noise improvement should theoretically be proportional to the square root of the number of sensors used [Johnson et al., 1999].

For the 4-element McChesney microphone, a 6 dB improvement in signal-to-noise could be expected under optimal conditions. Though a factor of two signal-to-noise gain may be ineffective for recovering degassing signals during periods of extreme wind (such as the
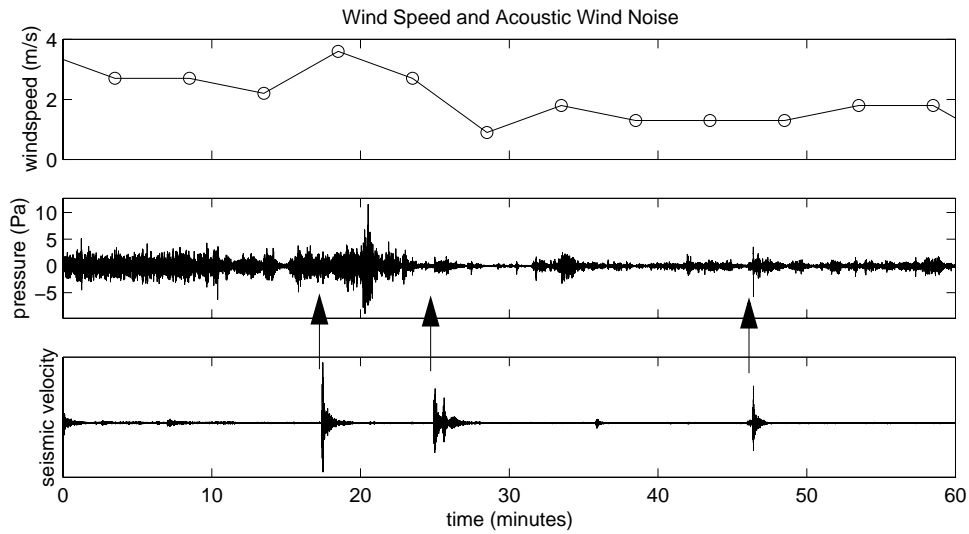
Figure B-4 - Wind Noise vs. Wind Speed - The relationship between wind speed and acoustic noise at a microphone deployed at Karymsky (station Krm3). Seismic events (and arrows) correspond to explosions with corresponding acoustic signals that are mostly obscured by wind noise (except for the third explosion). Anemometer wind speeds (top plot) are sampled 5 meters from the microphone and averaged over a 5 minute interval.
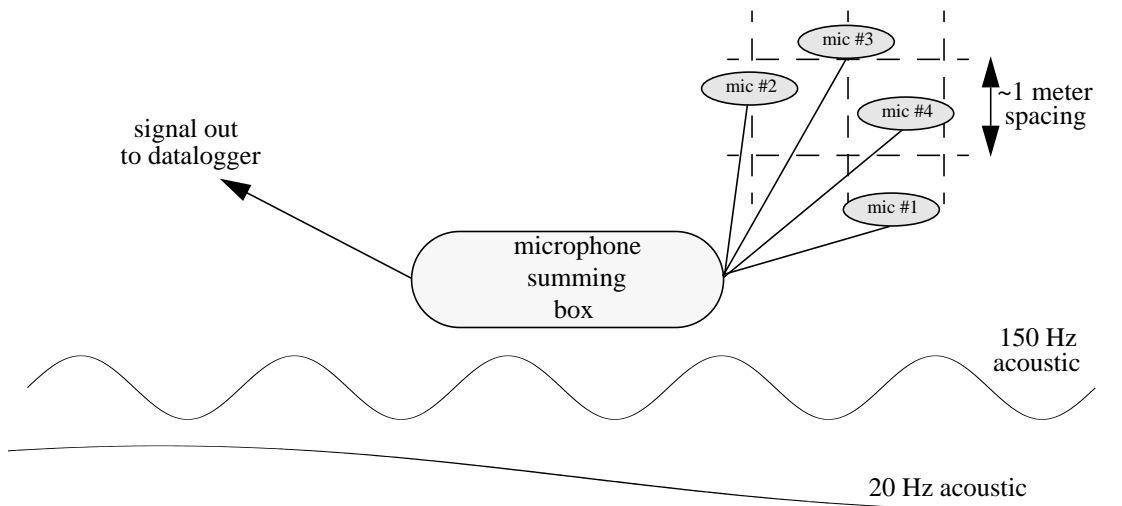

Figure B-5 Multi-element Microphone - Schematic showing design of the McChesney4 microphone summing box. Approximate meter spacing between individual sensors is sufficient for incoherent wind noise to combine destructively at the different sensors. However, a 20 Hz acoustic signal (~17 meter wavelength) is oblivious to the microphone separation. The summing box contains amplifier and low-pass filter.

noisy trace in figure B-3b), it can be a benefit when wind conditions are moderate. Figure B-6 shows infrasonic explosion signals from Karymsky in 1999 recorded at co-located McChesney1 and McChesney4 microphones. The multi-element microphone appears to record the explosion much more clearly, proving its utility as a wind filter. In certain instances, this reduction in noise may be sufficient to allow for the discrimination of degassing signal above background wind noise.
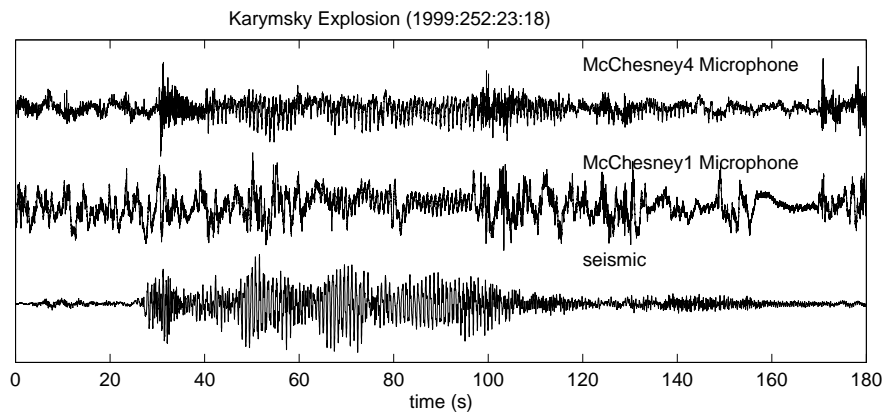
Karymsky Explosion (1999:252:23:18)

Figure B-6 Wind Noise Cancellation - Wind noise is a persistent problem on both acoustic channels, but the McChesney4 microphone shows significant improvement for the displayed Karymksy explosion. The 1-element microphone was co-located with the 4-element microphone which had ~1.5 meter sensor spacing. Both microphones were deployed at station Krm3, 1450 meters from the vent.

Appendix C - Karymsky Seismic Station Calibration

Seismic site responses are typically calibrated with tectonic earthquakes of known magnitude. Unfortunately, the seismic record from three field season at Karymsky provides only one local tectonic earthquake. This 4.3 M_b event occurred at 1999:252:03:52:42 at 54.0352 N and 159.4511 E (approximately 80 km from the volcano) using data from the Global Seismographic Network. The seismogram recorded at station Kry2 is shown in figure C-1.
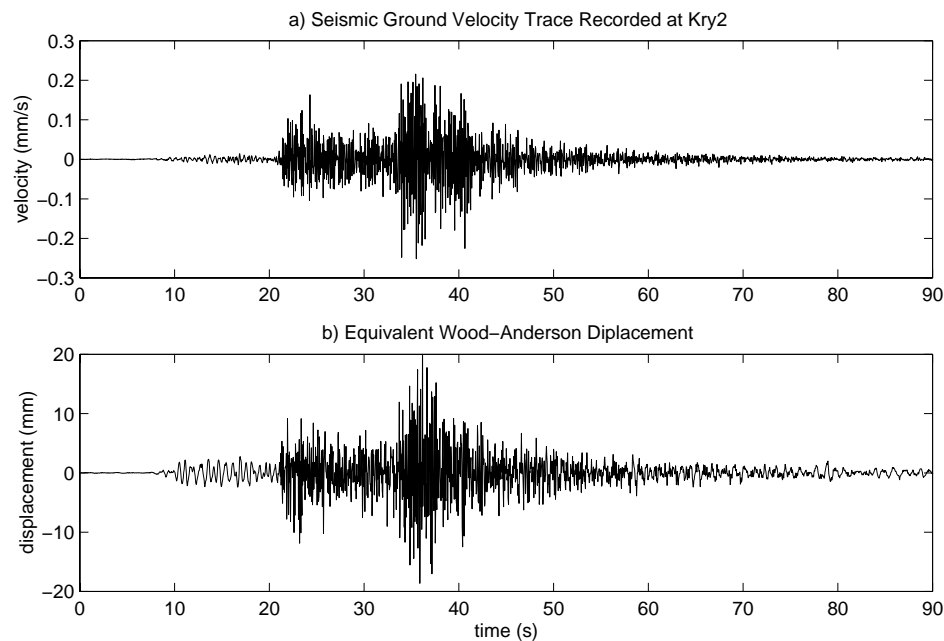

Figure C-1 - Tectonic Earthquake Seismogram at Karymsky - a) Horizontal ground velocity seismogram for M_b 4.3 earthquake recorded at station Kry2. b) Equivalent Wood-Anderson displacement trace (using magnification of 2800). Seismic trace onset corresponds to event origin time at 98:252:03:52:42.

To determine the local site responses at the Karymsky seismic stations, true horizontal ground velocity seismograms (figure C-1a) were converted to Wood-Anderson equivalent seismograms (figure C-1b) by integrating to displacement, applying a gain of 2800, and high-pass filtering above 0.8 Hz. The displacement records could then be converted to local magnitude (M_l) by using a version of Richter's formula [Lay & Wallace, 1995]:

$$M_L = \log(A) - 2.48 + 2.76\log(\Delta) \ \text{(equation C-1)}$$

A = maximum waveform amplitude mplitude (mm)

Δ = epicentral distance (km)

For the seismic trace recorded at station Kry2, maximum Wood Anderson displacement is 20 mm for an epicentral distance of 96 km (corresponding to a travel time difference of 12 seconds between P and S waves). According to equation C-1, the local magnitude using station Kry2 is estimated as ~4.35. The local magnitude estimate from Kry1 is somewhat lower (~4.2) because the equivalent Wood Anderson displacement at Kry1 is only 15 mm. Without applying any site response scaling factor, these local magnitude estimates agree very well with the 4.3 M_b estimate determined by the Global Seismic Network. Hence a site response of one is used for Karymsky reduced displacement and radiated seismic energy calculations in chapter 2.

Vita

Jeffrey B. Johnson

B.S. Geological & Environmental Sciences, Stanford University, 6/1995

M.S. Geophysics, Stanford University, 6/1996

Ph.D. Geophysics Program, University of Washington, 12/2000